Stony Brook University

Correlation between structure and thermoelectric properties: Searching for better thermoelectric materials

A Dissertation Presented

by

Qing Jie

to

The Graduate School

in Partial fulfillment of the

Requirements

for the Degree of

Doctor of Philosophy

in

Materials Science and Engineering

Stony Brook University

December 2010

Stony Brook University

The Graduate School

Qing Jie

We, the dissertation committee for the above candidate for the Doctor of Philosophy degree, hereby recommend acceptance of the dissertation.

Dr. Qiang Li- Dissertation Advisor
Scientist, Brookhaven National Laboratory
Adjunct Professor, Materials Science and Engineering, Stony Brook University

Dr. Dilip Gersappe – Chairperson of Defense
Associate Professor, Materials Science and Engineering, Stony Brook University

Dr. Genda Gu
Scientist, Brookhaven National Laboratory
Adjunct Professor, Materials Science and Engineering, Stony Brook University

Dr. Vyacheslav Solovyov
Scientist, Brookhaven National Laboratory

This dissertation is accepted by the Graduate School.

Lawrence Martin
Dean of the Graduate School

Abstract of the Dissertation

Correlation between structure and thermoelectric properties: Searching for better thermoelectric materials

by

Qing Jie

Doctor of Philosophy

in

Materials Science and Engineering

Stony Brook University

2010

The wide-spread application of thermoelectric devices is important for effective utilization of energy and environment. The market share of thermoelectric devices could potentially reach billions of dollars per year and urgently needs new materials with high energy conversion efficiency, which depends primarily on the thermoelectric figure of merit (ZT). $ZT = S^2T/(\rho\kappa)$, where S, ρ, κ, T are Seebeck coefficient, electrical resistivity, thermal conductivity and absolute temperature, respectively, and S^2/ρ is the power factor (P.F.). ZT could be enhanced by either decreasing the thermal conductivity or increasing the power factor of the material under study. In this work, the relationship between structure and the thermoelectric properties in a number of promising thermoelectric materials has been investigated. The goals are twofold: 1) developing novel synthesis/processing techniques to significantly increase the properties of known thermoelectric materials; 2) exploring new research

directions, particularly searching for new unconventional materials having exceptional high thermoelectric performance than the existing materials.

In the first part of this work, a non-equilibrium synthesis method, which employs melt spinning with a subsequent spark plasma sintering (SPS) technique, has been used to reduce the thermal conductivity of two different p-type filled skutterudite materials. The results show that the non-equilibrium synthesis method is capable of producing nano-size grains in both $Ce_{0.9}Fe_3CoSb_{12}$ and $Ce_{1.05}Fe_4Sb_{12.04}$ filled skutterudite materials. It is found that the rapid conversion process employed in the non-equilibrium method produces higher performance materials by simultaneously increasing the power factor and reducing their thermal conductivities. The *ZT* values were enhanced over the temperature range from 300K to 800K by up to 50%, compared with samples prepared by a traditional long term annealing method. Detailed high-resolution TEM investigation and electron transport measurements on $Ce_{1.05}Fe_4Sb_{12.04}$ filled skutterudite samples suggest that this non-equilibrium method created cleaner grain boundaries, and hence helped electron transport.

In the second part of this work, the enhancement of power factor in two other materials has been investigated. A new class of thermoelectric materials, $FeSb_2$, with metal-insulator transition was first investigated. By slightly changing the growth procedure, metal-insulator transition has been introduced into a $FeSb_2$ single crystal. Compared to the $FeSb_2$ single crystal without metal-insulator transition, this crystal has much lower electrical resistivity along the c-axis, and hence results in a record high thermoelectric power factor, which is nearly three

orders of magnitude higher than that belonging to the control sample without metal-insulator transition. In the last chapter of this work, the thermoelectric power and resistivity of misfit layered cobalt oxide $Ca_3Co_4O_9$ single crystal and polycrystalline samples have been measured up to 1000K using a home-made measurement system. Two transitions which lead to fast increase of the power factors in both materials have been found at 400K and around 800K respectively. i*n-situ* high temperature X-ray powder diffraction has been used to investigate the nature of those transitions. The results indicate that both of them are related to structural transitions in the material.

The results of the work in this thesis provide very useful information on the impact of structural changes on thermoelectric properties (both thermal conductivity and power factor). The mechanism we found here could help in the design and tailoring of better materials for thermoelectric power generation and cooling devices.

to Helen, Ru and My Parents

Table of Contents

List of Figures x

Acknowledgement xv

Publications xvii

Part I 1

1 Introduction 2

1.1 Background 5

1.1.1 Thermoelectric effects and their applications 5

1.1.2 Thermoelectric Efficiency and Figure of Merit 9

1.1.3 Current Commercial Thermoelectric Materials and Their Applications 11

1.1.4 Searching for Better Thermoelectric Materials 13

1.1.5 Filled Skutterudites 21

1.2 Non-equilibrium Processing Method 26

1.2.1 Melt spinning 26

1.2.2 Spark Plasma Sintering (SPS) 27

2 Experiments 30

2.1 Sample Synthesis 30

2.1.1 Ingot Preparation 30

2.1.2 Melt Spinning 32

2.1.3 SPS sintering 33

2.2 Phase and structure analysis 34

2.2.1 X-ray powder diffraction 34
2.2.2 Scanning Electron Microscope (SEM) 35
2.2.3 Transmission Electron Microscope (TEM) 35
2.3 Thermoelectric Properties Characterization 36
2.3.1 Low temperature thermoelectric properties measurement 36
2.3.2 High temperature thermoelectric properties measurement 41
3 Enhanced Thermoelectric Properties in Non-equilibrium Synthesized $Ce_{0.9}Fe_3CoSb_{12}$ Filled Skutterudites 46
3.1 X-ray Powder Diffraction 46
3.2 Micro-structural Observation by SEM 48
3.3 Thermoelectric Properties 50
3.4 Summary 53
4 Strong Impact of Grain Boundaries on the Thermoelectric Properties of Non-equilibrium Synthesized p-type $Ce_{1.05}Fe_4Sb_{12.04}$ Filled Skutterudites with Nanostructure 54
4.1 X-ray Powder Diffraction 55
4.2 Thermoelectric Properties 56
4.3 Micro-structural Observation by SEM and TEM 60
4.4 Impact of Grain Boundaries on Carrier Transport 62
4.5 Summary 65
5 Fure Perspectives 66
5.1 Double Filled p-type Antimonide Skutterudites 66
5.2 Half-Heusler Compounds 67

Part II 70

6 Giant Thermoelectric Power Factor Induced by Metal-Insulator Transition in $FeSb_2$ Single Crystal 71

6.1 Introduction 71

6.2 Single Crystal Growth 75

6.3 Thermoelectric Properties Measurement 75

6.4 Results and Discussion 78

6.5 Some Unsolved and Important Issues 83

7 Thermoelectric Misfit Layered Cobaltite $Ca_3Co_4O_9$: High Temperature Properties and *in-situ* X-ray Investigation 84

7.1 Introduction 84

7.2 Experiments 86

7.2.1 Sample Preparation 86

7.2.2 Home-made High-T TE Properties Measurement System 87

7.2.3 High temperature *in-situ* X-ray powder diffraction experiment 89

7.3 Results and Discussion 90

7.3.1 Single crystal quality investigation by X-ray diffraction 90

7.3.2 Thermoelectric Properties 91

7.3.3 Structural Transition Identified by i*n-situ* X-ray Powder Diffraction 94

7.4 Suggestions for theoretical modeling 97

REFERENCES 98

List of Figures

Figure 1.1 Illustration of a Seebeck effect circuit made of two different materials. T_h is the hot end temperature, and T_c is the cold end temperature. 6

Figure 1.2 Illustration of the Peltier effect. 6

Figure 1.3 Illustration of the Thomson effect 7

Figure 1.4 Diagram of a Seebeck and a Peltier thermoelectric couple made of an n-type and a p-type thermoelectric material. *I* is current. 8

Figure 1.5 Figure of merit of some commercial and promising thermoelectric materials [32] 12

Figure 1.6 Transport properties calculated for an idealized semiconductor at room temperature, plotted as a function of carrier concentration.[39] 15

Figure 1.7 Illustration of the filled skutterudite structure. For $Ce_{0.9}Fe_3CoSb_{12}$, the two large spheres represent the Ce atoms, the small dark gray spheres represent the Fe or Co atoms, and the light gray spheres represent Sb atoms. Note the four-membered Sb rings and the large ‘‘cage’’ in which the La resides. This illustration corresponds to the conventional unit cell shifted by the fractional coordinates 1/4, 1/4, 1/4 22

Figure 1.8 The of thermal conductivity of p-type (a, $CeFe_4Sb_{12}$)[6] and n-type (b, Yb_xCoSb_{12})[8] filled skutterudites. 23

Figure 1.9 The melt spin machine used in this work, the cartoon at the down-left corner shows how it works. 27

Figure 1.10 The working diagram of a SPS device 28

Figure 1.11 The mechanism of neck formation during SPS sintering 29

Figure 2.1 Filled skutterudite sealed in carbon coated quartz tube 31

Figure 2.2 An example of quenched filled skutterudite ingot 31

Figure 2.3 Typical melt spun ribbon of filled skutterudite 32

Figure 2.4 The pressure dependence of melt spun ribbon thickness. 33

Figure 2.5 SPS sintered filled skutterudite pellet 34

Figure 2.6 Physical Properties Measurement System (PPMS, Quantum Design) 36

Figure 2.7 Thermal Transport sample puck and radiation shield 37

Figure 2.8 Four-wire Hall effect measurement 40

Figure 2.9 A ULVAC ZEM-3 Seebeck Coefficient / Electric Resistance Measuring System and the schematic diagram for the measurement 41

Figure 2.10 Schematic of the flash method 43

Figure 2.11 Temperature increase for various experimental conditions 44

Figure 2.12 Anter Flashline^{TM} 4020 Thermal Properties Analyzer 45

Figure 3.1 X-ray powder diffraction pattern of filled skutterudite $Ce_{0.9}Fe_3CoSb_{12}$ prepared by (a) non-equilibrium (MS) and (b) equilibrium (AN) synthesis. The Miller indices for several of the peaks are marked by X. The arrows denote the $Fe(Co)Sb_2$ impurity peaks observed in the samples. 47

Figure 3.2 SEM images of fracture surfaces of the (a) MS and (b) AN samples 48

Figure 3.3 Temperature dependences of (a) ρ, (b) S and (c) power factor for the AN (solid square) and MS samples (open circle) 50

Figure 3.4 Temperature dependence of (a) κ, (b) κ_L and (c) ZT for AN (solid square) and MS samples (open circle) 52

Figure 4.1 A comparison of X-ray diffraction spectrum of melt spin ribbon (a), non-equilibrium synthesized pellet (b) and equilibrium synthesized pellet (c). 55

Figure 4.2 The temperature dependence of the electrical resistivity (a), thermopower (b) and power factor ($PF=S^2/\rho$) (c) in samples prepared by non-equilibrium (red circle) and equilibrium (black square) method. 57

Figure 4.3 Temperature dependence of thermal conductivity κ (a), lattice thermal conductivity κ_L (b) and ZT (c) in samples prepared by non-equilibrium (red circle) and equilibrium (black square) method. 59

Figure 4.4 SEM images of the fracture surface of (a) non-equilibrium MS and (b) equilibrium AN samples. The inset to (a) is the HRTEM image showing the nanostructure of the melt-spun ribbon prior to SPS. HRTEM images showing typical grain boundaries in the MS samples (c) and the AN samples (d). 61

Figure 4.5 The temperature dependence of hole mobility and hole concentration (the inset) in p-type $Ce_{1.05}Fe_4Sb_{12.04}$ filled skutterudites prepared by non-equilibrium (red circle) and equilibrium (black square) method. The hole mobilities of two samples were calculated using equation $\sigma = pe\mu$, where e is the electric charge of the carrier. The lines are corresponding fitting curves (see text). 63

Figure 5.1 Figure of merit ZT versus T for $Hf_{0.75}Zr_{0.25}NiSn_{0.975}Sb_{0.025}$ obtained from measured (∇) and extrapolated ($\bullet$) thermal conductivities. The upper left inset shows the unit cell of TiNiSn half-Heusler phase. The lower right inset shows thermal conductivities obtained from laser-flash thermal

diffusivity and specific heat, with data points starting at 300 K:$Hf_{0.75}Zr_{0.25}NiSn_{0.975}Sb_{0.025}$(▼), $Hf_{0.6}Zr_{0.25}Ti_{0.15}NiSn_{0.975}Sb_{0.025}$ (■), and $Hf_{0.75}Zr_{0.25}Ni_{0.9}Pd_{0.1}Sn_{0.975}Sb_{0.025}$(□)[74]. 68

Figure 6.1 Crystal structure of $FeSb_2$ [92] showing Fe (open, brown crosses) surrounded by Sb (full blue) octahedral. 74

Figure 6.2 The traditional Flux method for $FeSb_2$ single crystal preparation and the single crystal grown by this method. 76

Figure 6.3 The modified Flux method for $FeSb_2$ single crystal preparation and the single crystal grown by this method 77

Figure 6.4 The temperature dependence of the resistivity of $FeSb_2$ single crystals along the highly conductive *c*-axis 79

Figure 6.5 The temperature dependence of the Seebeck coefficient of $FeSb_2$ single crystals along *c*-axis 80

Figure 6.6 The temperature dependence of thermoelectric power factor of $FeSb_2$ single crystals along *c*-axis 81

Figure 7.1 Schematic illustration of the crystal structure of $Ca_3Co_4O_9$ 85

Figure 7.2 Photograph of the as grown $Ca_3Co_4O_9$ single crystal prepared by the flux method 86

Figure 7.3 The home-made high temperature thermoelectric properties measurement system: (a) the whole system, (b) the probe for resistivity measurement, (c) the schematic diagram of the thermopower measurement 89

Figure 7.4 The XRD pattern of a $Ca_3Co_4O_9$ single crystal (the thickness ~ 0.1mm) shows the crystalline c-axis perpendicular to the surface (a-b plane) of the crystal. 90

Figure 7.5 Temperature dependence of thermopower and resistivity of $Ca_3Co_4O_9$ (a) polycrystalline sample, and (b) single crystal (a-b plane) above 300K 91

Figure 7.6 The temperature dependence of power factors for CCO polycrystal (a) and single crystal a-b plane (b). 93

Figure 7.7 The X-ray powder diffraction spectrum of $Ca_3Co_4O_9$ recorded from 375 to 407K 95

Figure 7.8 The 004 Peak shifting (a) and d-spacing change (b) of $Ca_3Co_4O_9$ around 800K 96

Acknowledgement

First of all, I am deeply grateful to my thesis advisor, Dr. Qiang Li, who led me into this field and gave me continuous encouragement and support. The training I got from him is invaluable.

I owe a special thank to my family who gave their support to me without any condition. I want to thank my wife, Ru Jiang, for accompanying me here in U.S. and always trusting my choices. I thank my parents for allowing me to leave them and across half of the world to pursue my dream. I can not accomplish it without their love.

I want to thank my department, the Department of Materials Science and Engineering in Stony Brook University, for giving me this opportunity to study and pursue doctor degree in the United States. Professor Richard Gambino, Professor Dilip Gersappe, Mrs. Debby Michienzi, and Mrs. Lynn Allopenna have been giving very helpful advices on every step I have taken.

I am also indebted to colleagues and friends at Brookhaven National Laboratory. I would like to thank Dr. Yufeng Hu for teaching me all the basic research skills, and Dr. Genda Gu for all those helpful discussions. Dr. Vyacheslav Solovyov set a very good example for me as an active and independent scientist in our collaboration. Dr. Jack Lin, Dr. Ivo K. Dimitrov, Dr. Arnold Moodenbaugh and Dr. Harold (Bud) Wiesmann have helped me a lot on melt spinner and materials synthesis. Dr. Juan zhou performed TEM characterization on our samples. Dr. Rongwei Hu and Dr. Cedomir Petrovic provided the $FeSb_2$ single crystals for the measurement. I want to thank Dr.

Haiyan Chen for her work on *in-situ* high-T X-ray powder diffraction at NSLS. I appreciate Dr. Zhijun Xu's help on the single crystal orientation.

I appreciate the help offered by Dr. Xun Shi and Dr. Jihui Yang from GM R&D center on SPS sintering.

I want to thank Dr. Hsin Wang, Dr. Wallace Porter (Oak Ridge National Laboratory), Dr. Changpeng Li and Professor Ctirid Uher (University of Michigan) for their help on high-T thermoelectric properties measurement.

The research work presented in this dissertation was supported by the U.S. Department of Energy, Office of Basic Energy Science, under Contract No. DE-AC02-98CH10886, and also partly supported by the U. S. Department of Energy, Office of Energy Efficiency and Renewable Energy, Vehicle Technologies Program.

Publications

1. **Jie Q**, Zhou J, et al., Impact of grain boundaries on the thermoelectric properties of non-equilibrium synthesized p-type $Ce_{1.05}Fe_4Sb_{12.04}$ filled skutterudites with nanostructure, (in preparation).
2. Wen J, **Jie Q**, et al., Magnetic-field-induced decoupling of superconducting layers in a copper-oxide compound, NATURE, submitted.
3. Dimitrov IK, Manley ME, Shapiro SM, Yang J, Zhang W, Chen LD, **Jie Q**, et al., Einstein Modes in the Phonon Density of States of the Single-Filled Skutterudite $Yb_{0.2}Co_4Sb_{12}$, PHYSICAL REVIEW B, accepted.
4. **Jie Q**, Zhou, J et al., Thermoelectric Properties of Non-equilibrium Synthesized $Ce_{0.9}Fe_3CoSb_{12}$ Filled Skutterudites, MRS PROCEEDING, 2010, accepted.
5. Si WD, **Jie Q**, et al., Superconductivity in $Fe_{1:08}Te:O_x$ Epitaxial Thin Films, PHYSICAL REVIEW B, Vol 81, 092506 (2010)
6. Solovyov V.F., Develos-Bagarinao K, Li Q, **Jie Q** and Zhou J, Nature of $Y_1Ba_2Cu_3O_7$ nucleation centers on ceria buffers, SUPERCOND. SCI. TECHNOL. 23, 014008 (2010)
7. Si WD, Lin ZW, **Jie Q**, et al., Enhanced superconducting transition temperature in $FeSe_{0.5}Te_{0.5}$ thin films, APPLIED PHYSICS LETTERS, Volume:95, Issue:5, 052504 (2009)
8. Lu, Z. Q. J., Lowhorn, N. D., Wong-Ng, W., **Jie Q**. et al, Statistical Analysis of a Round-Robin Measurement Survey of Two Candidate Materials for a Seebeck Coefficient Standard Reference Material, J. RESEARCH OF NIST, Vol 114, 1, 37-55 (2009)

9.Tyson TA, Chen Z, **Jie Q**, et al., Local structure of thermoelectric $Ca_3Co_4O_9$, PHYSICAL REVIEW B, Vol 79, 024109 (2009)

10. Lowhorn ND, Wong-Ng W, Zhang W, **Jie Q**, et al., Round-robin measurements of two candidate materials for a Seebeck coefficient Standard Reference Material (TM), APPLIED PHYSICS A-MATERIALS SCIENCE & PROCESSING, Volume: 94, Issue: 2, 231-234 (2009)

11. Tranquada JM, Gu GD, Hucker M, **Jie Q**, et al., Evidence for unusual superconducting correlations coexisting with stripe order in $La_{1.875}Ba_{0.125}CuO_4$, PHYSICAL REVIEW B, Volume: 78, Issue: 17, 174529 (2008)

Part I

Non-equilibrium Synthesis of Filled Skutterudites

Thermoelectric Materials

1 Introduction

The promising perspective of widespread application of thermoelectricity relies on the availability of superior materials that would exceed the performance of current state-of-the-art thermoelectric (TE) materials, such as Bi_2Te_3-Sb_2Te_3, PbTe, and Si-Ge solid solutions. The efficiency of a TE material is related to the dimensionless figure of merit *ZT*, expressed as $ZT = S^2T/(\rho\kappa)$, where *S*, ρ, κ, *T* are the Seebeck coefficient, electrical resistivity, thermal conductivity and absolute temperature, respectively. The thermal conductivity, κ could be expressed as the sum of the electronic thermal conductivity (κ_e) and lattice thermal conductivity (κ_L). Since κ_L is the only parameter that could be tuned separately in this equation, reducing the lattice thermal conductivity has become a very important method in order to increase *ZT*.

Filled skutterudites are among the most promising material systems for intermediate temperature power generation owing to both good thermoelectric and mechanical properties.[1-4] Earlier transport studies found that the p-type binary skutterudite $CoSb_3$ exhibits very high hole mobility and power factor, albeit low *ZT* owing to its high lattice thermal conductivity.[5] During the past 15 years, extensive work has been performed on synthesizing skutterudite materials

with the primary goal of lowering their thermal conductivities by introducing "rattling" atoms into the cages in their crystal lattice. In 1995, Morelli and Meisner reported a near tenfold reduction in the thermal conductivity by filling the voids in skutterudite lattice with Ce atoms.[6] On the n-type side, Nolas *et al.* reported reductions in the thermal conductivity of Yb filled skutterudites, by as much as 50%,[7-8] and hence the *ZT* value of $Yb_{0.2}Co_4Sb_{12}$ was raised above 1 at temperatures higher than 600K. Recently, the thermal conductivity of antimonide skutterudites has been further reduced by filling the voids with two or three different elements.[9-10] However, despite the successful reduction of κ, the carrier mobility has also been degraded rather strongly as a consequence of filling[6-8, 11-12]. This adversely affects the power factors of those materials. Furthermore, the synthesis process involves a long term annealing (varying from two days to one week) in order to form the desirable filled skutterudite phase, which on the other hand also causes the segregation of minority second phases into grain boundaries and raises the cost of large scale production. Different technology is needed to implement the further reduction of κ without deteriorating carrier mobility.

An early calculation shows that internal interfaces in nanostructured materials could reduce the thermal conductivities more than their electrical conductivities, based on differences in their respective scattering lengths[13]. During the past decade, enhancement of *ZT* has been reported in superlattices such as Bi_2Te_3/Sb_2Te_3 [14] and $PbSe_{0.98}Te_{0.02}/PbTe$ [15], due to reductions in their lattice thermal conductivities. Poudel *et al.* successfully reduced the thermal

conductivity in p-type BiSbTe alloy by producing nano-sized grains *via* a special ball milling technique, and raised the peak value of *ZT* from 1 to 1.4 [16]. Recently, a non-equilibrium synthesis technique, which employs melt-spinning with subsequent spark plasma sintering (SPS), has been introduced in thermoelectric research due to its high efficiency and ability to create very small grain size in materials. Significant reduction in the thermal conductivity has been observed in n-type filled skutterudites prepared by this method [17-18]. However, lower carrier mobility and decreased power factor is also observed in these melt-spun samples[19]. In this work, we set to prepare p-type filled skutterudite materials, by both non-equilibrium (melt-spinning followed by SPS) and equilibrium process (long term annealing). We will investigate the effects of non-equilibrium synthesis method on p-type filled skutterudites by comparing the thermoelectric properties and microstructures of these samples.

1.1 Background

1.1.1 Thermoelectric effects and their applications

There are three related reversible thermoelectric (TE) effects: Seebeck, Peltier and Thomson effects.[20] In 1821, Thomas Johann Seebeck (1770-1831), a German scientist, discovered that a small electric current would flow in a closed circuit composed of two dissimilar metallic conductors when their junctions are kept at different temperatures. A thermocouple consists of two such dissimilar metals connected in series. The electromotive force, or emf (V), that appears in an open circuit is the emf developed by the thermocouple which blocks the flow of electric current.

If the circuit is opened, the emf created, E_{ab}, is called the relative Seebeck emf (RSE), or Seebeck voltage. The emf E_{ab} created is directly proportional to the differential temperature ΔT (K) between the two junctions

$$E_{ab} = S_{ab} \times \Delta T \tag{1.1}$$

where S_{ab} (V/K) is called the Seebeck coefficient of the circuit.

This effect is illustrated in Figure 1.1. The pair a-b of thermoelements, creates the thermoelectric circuit, which is the basis of thermoelectric power generation. The thermoelement *a* is the positive conductor with respect to *b* if the current flows from *a* to *b* in the cold junction. If *a* and *b* are a pair of semiconductors, then a is usually p-type material, and b is usually n-type material.

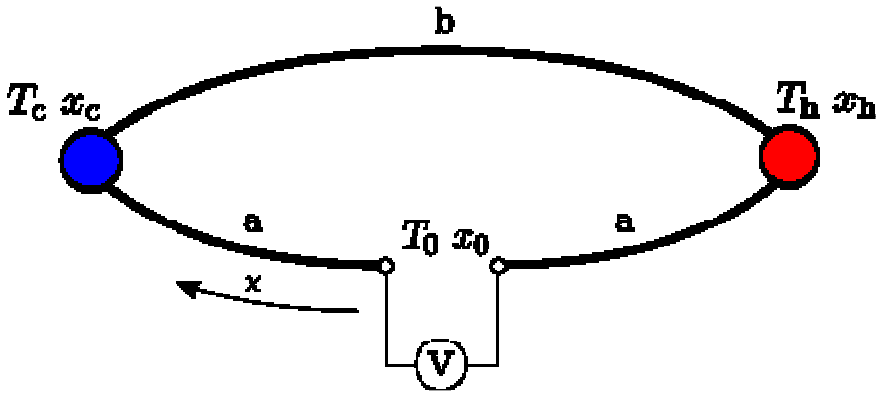

Figure 1.1 Illustration of a Seebeck effect circuit made of two different materials. T_h is the hot end temperature, and T_c is the cold end temperature.

In 1834, Jean Charles Athanase Peltier (1785-1845), discovered that when an electric current flows across a junction of two dissimilar metals, heat is liberated or absorbed depending on the direction of this electric current. The rate of heat liberated or absorbed P is proportional to the electric current I flowing in the conductor, that is

$$P = P_{ab} \times I \tag{1.2}$$

where P_{ab} is called the relative Peltier coefficient. This effect is the basis of thermoelectric refrigeration or heating. The Peltier effect is illustrated in Figure 1.2.

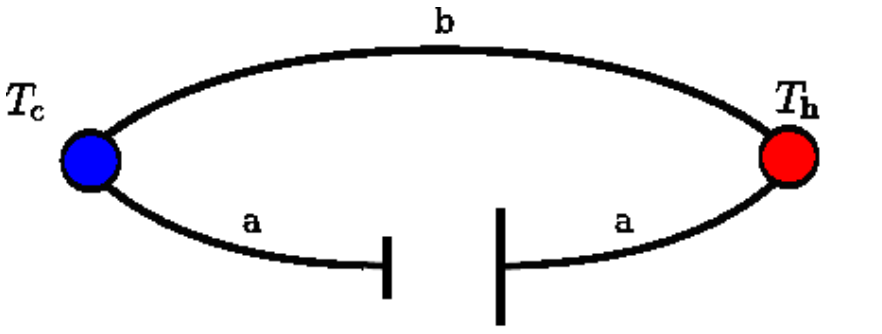

Figure 1.2 Illustration of the Peltier effect.

In 1852, Thomson discovered that if an electric current flows along a single conductor while a temperature gradient exists in the conductor, an energy interaction takes place in which power is either absorbed or rejected, depending on the relative direction of the current and gradient. More specifically heat is liberated if an electric current flows in the same direction as the heat flows; otherwise it is absorbed. Figure 1.3 illustrates the Thomson effect.

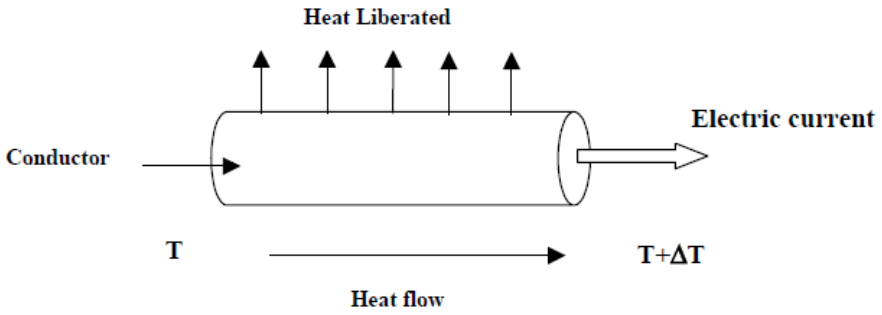

Figure 1.3 Illustration of the Thomson effect

The power P' absorbed or rejected per unit length (W/m) is proportional to the product of the electric current I (A) and the temperature gradient dT/dx (K/m), that is,

$$P' = \sigma(T)\, I\, dT/dx \tag{1.3}$$

where $\sigma(T)$ (V/K) is the Thomson coefficient.

The widest application for Seebeck effect is the thermopiles or thermocouples for temperature measurement. Another application is power-generation devices that are designed to convert heat into electrical energy (Fig1.4 (a)). The deep space applications of NASA's Voyager and Cassini missions using radioisotope thermoelectric generators (RTGs) are well established[21].

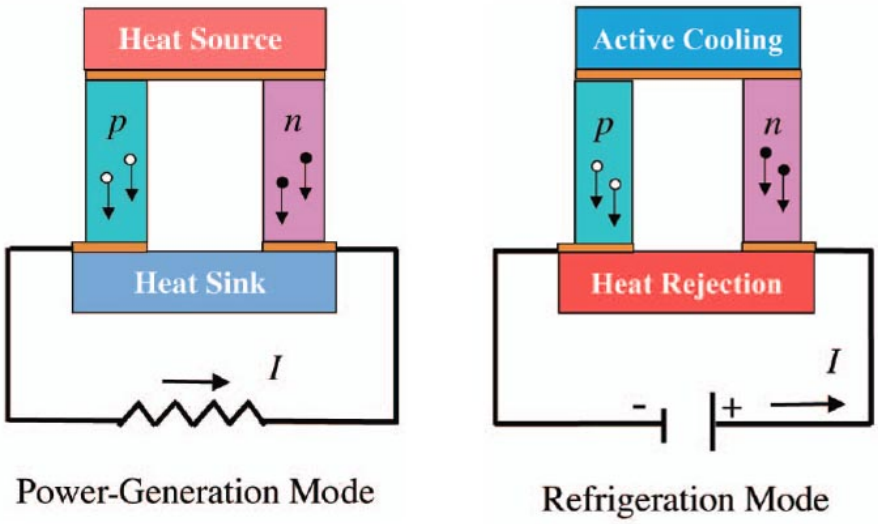

(a) (b)

Figure 1.4 Diagram of a Seebeck and a Peltier thermoelectric couple made of an n-type and a p-type thermoelectric material. *I* is current.

The most important application of the Peltier Effect is for solid-state refrigeration devices (Fig.1.4 (b)). Such TE devices use electricity to pump heat from cold to hot, without any moving parts or bulk fluids [liquids or gases like chloroflurocarbons(CFCs) or hydrochloroflurocarbons (HCFCs)]. TE refrigerators are lightweight, small, and inexpensive, and they completely eliminate the need for CFCs and HCFCs and heavy compressors in small-scale refrigeration. Thermoelectric refrigeration could also be an environmentally "green" method of small scale, localized cooling in computers, infrared detectors, electronics, and opto-electronics as well as many other applications, such as seat coolers for comfort. If significant economical cooling can be achieved, the resulting "cold computing" could produce speed gains of 30-200% in some computer processors based on complementary metal oxide semiconductor (CMOS) technology.[22] Recent utilization of Peltier coolers for the refrigeration of biological specimens

and samples is an emerging thermoelectric application. Currently, the world market for TE cooling devices is still small (about $80 million to $160 million per year).[23]

Over the past decade, there has been heightened interest in the field of thermoelectrics. This is primarily driven by the demand for alternative energy to reduce our dependence on fossil fuels. There is growing economic, social, and environmental pressure to reduce fuel consumption. Thus, the development of higher-performance thermoelectric materials is becoming ever more important. Power-generation applications are currently being investigated by the automotive industry as a means of developing electrical power from waste engine heat from the radiator and exhaust systems for use in next-generation vehicle. A conservative estimate is that the world market for efficient TE materials alone (at current TE materials prices) is billions of dollars per year.[23] If one includes the value added to home refrigerators or computers and power generation, the economic impact could be huge.

1.1.2 Thermoelectric Efficiency and Figure of Merit

Presently, the use of TE devices is limited by their low efficiencies. The efficiency of a refrigerator is expressed by the coefficient of performance (COP). The laws of thermodynamics tell us that a maximum efficiency, called the Carnot efficiency, cannot be exceeded. The COP at Carnot efficiency is just $T_{cold}/(T_{hot}-T_{cold})$ for refrigeration, where T_{hot} and T_{cold} are the temperature of the ambient environment and of the coldest part of the refrigerator, respectively. The real

efficiency of any device is often given as a percentage of the Carnot efficiency. Present TE devices operate at about 10% of Carnot efficiency, whereas the efficiency of a compressor-based refrigerator increases with size: a kitchen refrigerator operates at about 30% of Carnot efficiency and the largest air conditioners for big buildings operate near 90%.

In case of power generation, thermoelectric (TE) device performance relies directly on the temperature gradient (ΔT) and an intrinsic material parameter, the thermoelectric figure of merit (*ZT*). The thermoelectric efficiency is defined by combining the Carnot efficiency ($\Delta T / T_{hot}$) and the figure of merit *ZT* as shown in equation 1.4[24]

$$\eta = \frac{\Delta T}{T_{hot}} \frac{\sqrt{1+ZT_{avg}}-1}{\sqrt{1+ZT_{avg}}+\frac{T_{cold}}{T_{hot}}} \qquad \textbf{(1.4)}$$

Where T_{hot} and T_{cold} are the temperature of the hot and cold ends in a thermoelectric module and ΔT is their difference. The term $\sqrt{1+ZT_{avg}}$ varies with the average temperature T_{avg}. This equation indicates that increasing efficiency requires both high *ZT* values and a large temperature gradient across the thermoelectric materials.

The best materials available today for commercial devices that operate near room temperature have *ZT* of about 1, a value that has increased by only a few tens of percent since the late 1950s. These materials are alloys of antimony and bismuth tellurides with traces of other elements to dope the semiconductors. Thermoelectric devices with *ZT* of 1 operate at only 10% of Carnot efficiency. By

increasing *ZT* by a factor of 4, and depending on ΔT, the predicted efficiency would be increased to 30%, a highly attractive prospect.

1.1.3 Current Commercial Thermoelectric Materials and Their Applications

Before we evaluate the method to enhance the *ZT* value for thermoelectric materials, we will start with a brief review of the development of commercial thermoelectric materials and their properties.

The most widely used thermoelectric materials are alloys of Bi_2Te_3 and Sb_2Te_3. For near-room-temperature applications, such as refrigeration and waste heat recovery up to 200 °C, Bi_2Te_3 alloys have been proven to possess the highest *ZT* value for both n- and p-type thermoelectric systems. Bi_2Te_3 was first investigated as a material of great thermoelectric promise in the 1950s.[25-28] It was quickly realized that alloying with Sb_2Te_3 and Bi_2Se_3 allowed for the fine tuning of carrier concentrations along with reductions in lattice thermal conductivities. The most commonly studied p-type compositions are near $(Sb_{0.8}Bi_{0.2})_2Te_3$ whereas n-type compositions are close to $Bi_2(Te_{0.8}Se_{0.2})_3$. The electronic transport properties and detailed defect chemistry (which controls the dopant concentration) of these alloys are now well understood thanks to extensive studies of single crystal and polycrystalline materials.[29-30] Peak *ZT* values for these materials are typically in the range of 0.8 to 1.1. *p*-type materials achieved the highest values among them (Fig. 1.5b). By adjusting the carrier concentration, *ZT* can be optimized to peak at different temperatures, enabling the tuning of materials for specific applications such as cooling or power generation.[31]

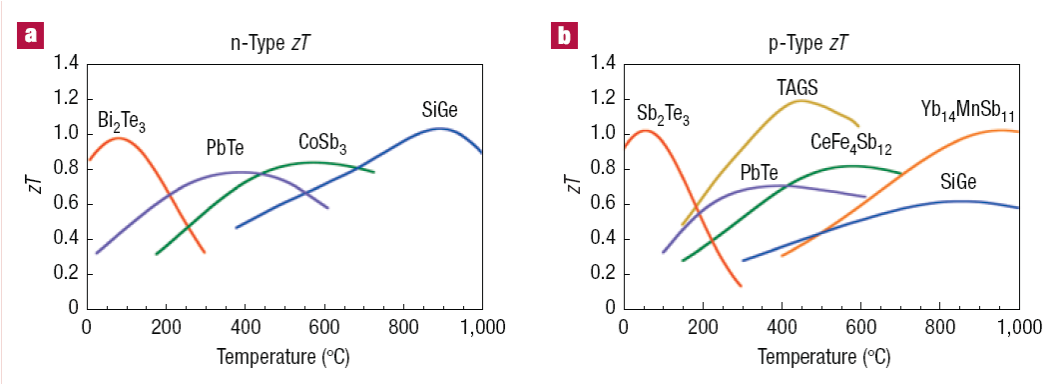

Figure 1.5 Figure of merit of some commercial and promising thermoelectric materials [32]

For mid-temperature power generation (500–900 K), materials based on group-IV tellurides are typically used, such as PbTe, GeTe or SnTe.[26, 28, 33] The peak *ZT* in optimized n-type material is about 0.8. Again, a tuning of the carrier concentration will alter the temperature where *ZT* peaks. Alloys, particularly with $AgSbTe_2$, have led to several reports of $ZT > 1$ for both n-type and p-type materials.[34] Only the p-type alloy $(GeTe)_{0.85}(AgSbTe_2)_{0.15}$, commonly referred to as TAGS, with a maximum *ZT* greater than 1.2 , has been successfully used in long-life thermoelectric generators.[35] With the advent of modern microstructural and chemical analysis techniques, such materials are being reinvestigated with great promise.

Successful, high-temperature (>900 K) thermoelectric generators have typically used silicon–germanium alloys for both n- and p-type legs. The *ZT* of these materials is fairly low, particularly for the p-type materials (Fig. 1.5b) because of the relatively high lattice thermal conductivity of the diamond structure.

For cooling below room temperature, alloys of BiSb have been used in the n-type legs, coupled with p-type legs of $(Bi,Sb)_2(Te,Se)_3$.[36-37] The poor mechanical properties of BiSb leave much room for the research for other low-temperature materials.

1.1.4 Searching for Better Thermoelectric Materials

TE efficiencies have experienced slow advance since the late 1950s. However, it is a good time to look for better TE materials now. Progress in synthetic methods and especially in structure determination by X-ray diffraction has been rapid and allows much more complicated materials to be studied than those used in present TE devices. In some cases, atom by atom control of the growth of artificially structured or compositionally graded materials can be obtained. Modern computers make it possible to rapidly calculate a realistic electronic description of the carriers (band structure). The combination of all these advances has increased the chances of developing improved TE materials.

The challenge to create high *ZT* thermoelectric materials lies in achieving simultaneously low electronic resistivity (ρ), high thermoelectric power (S) and low thermal conductivity (κ) in the same solid. These properties define the dimensionless thermoelectric figure of merit as

$$ZT = \frac{S^2}{\rho\kappa}T = \frac{S^2}{\rho(\kappa_e + \kappa_L)}T \tag{1.5}$$

where κ_e is the carrier thermal conductivity, κ_L is the lattice thermal conductivity. By treating the carriers as Fermi gas, we have

$$\kappa_e = \frac{\pi^2 n k_B^2 \tau}{3m} T \quad \textbf{(1.6)}$$

where n is the carrier concentration, τ is the collision time, k_B is the Boltzmann's constant, m is the effective mass of carrier, and T is the absolute temperature.

Wiedemann and Franz observed that, in many metals at not too low temperatures, the ratio of the thermal conductivity to the electrical conductivity is directly proportional to the temperature, with the value of the constant of proportionality independent of the particular metal.[38] In the frame of electron Fermi gas, we have

$$\frac{\kappa_e}{\sigma} = \frac{\pi^2}{3}(\frac{k_B}{e})^2 T \quad \textbf{(1.7)}$$

where σ is electrical conductivity, and e is the charge of a single carrier. This is known as the Wiedemann-Franz law. The Lorenz number L is defined as

$$L = \frac{\kappa_e}{\sigma T} \quad (1.8)$$

and equals 2.45×10^{-8} $W\Omega K^{-1}$. When the temperature is much lower than the Debye temperature, the Lorenz number tends to decrease.

The challenge in optimizing ZT lies in the fact that the three parameters in ZT (S, σ, and κ_e) are not independent. There is no simple way of enhancing the ZT values by changing one parameter while keeping the other parameters at the same level. However, some guidelines do exist in the search for new material systems for thermoelectric applications.

Higher Power Factor

There are four guidelines for finding materials with favorable electronic properties. The first one is that *heavily doped semiconductors make the best thermoelectrics*.[39] Figure 1.6 shows the calculation of the carrier concentration dependence of the thermoelectric properties in a simplified model. Within the framework of this simple model, metals are poor thermoelectric materials because of their low Seebeck coefficients and large electronic contributions to the thermal conductivity. Insulators have large Seebeck coefficients and small electronic contributions to their thermal conductivity, but have too few carriers, which results in large electrical resistivities.

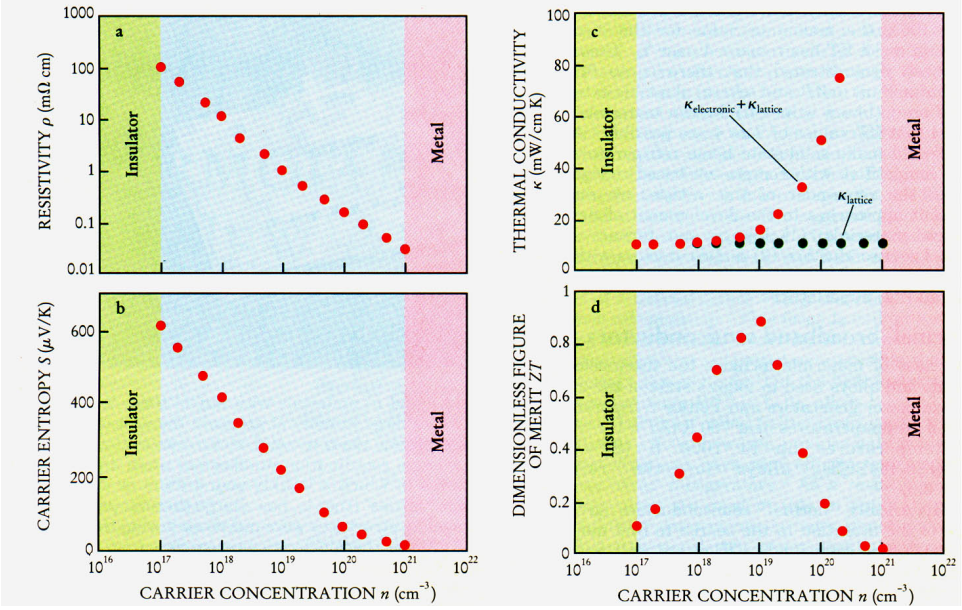

Figure 1.6 Transport properties calculated for an idealized semiconductor at room temperature, plotted as a function of carrier concentration.[39]

For this example, the largest value for *ZT* is obtained midway between these two extremes (metal or insulator) at a carrier concentration of about $10^{19}/cm^3$.

The second guideline is the "$10k_BT_{max}$ rule" and concerns the size of the semiconducting energy gap. *For optimum thermoelectric performance, the energy gap of the semiconductor must be at least 10 times* k_BT_{max}, where T_{max} is the maximum operating temperature. Small gaps are generally good for thermoelectric performance because they lead to higher carrier mobilities. However, if the gap is too small then the thermal excitation of minority carriers will adversely affect the figure of merit, since electrons and holes carry heat in opposite directions. An in-depth examination of this situation has been given by Mahan *et al*.[40] They found that the $10k_BT_{max}$ rule holds for direct and indirect gaps, and for both phonon and impurity scattering. The rule is also in reasonable accord with experimental data on good thermoelectrics.

It has been shown theoretically that $Z \propto \mu \cdot m^{*\frac{3}{2}}$,[41] where μ is carrier mobility, and m^* is the density of states effective mass. Therefore it is desirable to maximize both m^* and μ. Two important guidelines for materials result from the above proportionality. The first follows from the observation that m^* can be increased without affecting μ much if the semiconductors has several equivalent bands; therefore, *good thermoelectrics are likely to be multivalley semiconductors, and crystal structures with high symmetry are required to produce several equivalent bands*.[42] The second concerns the electronegativity difference between the elements making up the thermoelectric materials. The electronegativity difference is a measure of the covalency of the bonding in a material. Large electronegativity differences indicate ionic bonding, large charge transfer, and strong scattering of electrons by optical phonons. This strong

scattering leads to low carrier mobilities, and is one reason why oxides generally make poor thermoelectric materials. High electron mobilities, on the other hand, are found in materials composed of elements with very similar values of electronegativity.[43] *Good thermoelectrics, then, are composed of elements having small differences in electronegativity.*

Lower Lattice Thermal Conductivity

Above guidelines are used to make sure that potential thermoelectric materials have good electronic properties. However a material with good electronic properties is not necessary a good thermoelectric material, because κ_L in many semiconductors is much greater than κ_e. Thus, another challenge is to minimize κ_L.

The classical kinetic theory provides a good approximation for the lattice thermal conductivity.

$$\kappa_L = \frac{1}{3} C_v l v_s \tag{1.9}$$

where C_v is the specific heat at constant volume, l is mean free path of the heat carrying phonon, and v_s is the average velocity of sound.[38]

At very low temperature (under 40K), the behavior of κ_L is dominated by the Debye T^3 law for C_v. Phonon scattering is insignificant in this temperature range, because of the low number of excited phonons and their very long wavelengths.

However, at high temperatures (above the Debye temperature), C_v approaches the classical value of 3R, making κ_L primarily depend on l which is determined by phonon-phonon scattering. According to Keyes's expression[44] the lattice thermal conductivity is dominated primarily by phonon-phonon scattering:

$$\kappa_L T = \frac{R^{3/2}}{3\gamma^2 \varepsilon^3 N_0^{1/3}} \frac{T_m^{3/2} \rho^{2/3}}{A^{7/6}} \tag{1.10}$$

where T_m is the melting point, A is the mean atomic weight, γ is the Grüneisen constant, ε is the fractional amplitude of interatomic thermal vibration , R is the ideal gas constant, N_0 is Avogadro's number, and ρ is the density. This equation allows some useful insight into thermal conductivity: 1) in the high temperature range κ_L follows a *1/T* law, 2) a low melting point can lead to a low thermal conductivity, 3) κ_L decreases with increasing atomic mass, and 4) the proportionality to $\rho^{2/3}$ makes κ_L low for crystals with large interatomic distances.

Many of the guidelines for finding materials with a low lattice thermal conductivity can be understood from the above expressions.

First, *look for materials in which the average atomic weight is high*. The origin of this rule is simple: heavy atoms lead to small sound velocities and a correspondingly low thermal conductivity.[45]

Second, *mass fluctuation scattering can be used to reduce the lattice thermal conductivity*. The idea behind this rule is that isovalent substitutions will scatter heat carrying phonons strongly because the wavelength of these phonons is about the same as the distance between the scattering centers. Electrons, on the

other hand, have longer wavelengths and will be scattered less. The value of *ZT* will therefore increase.

Third, *crystal structures with many atoms per unit cell tend to have low lattice thermal conductivities*. This rule is not as well grounded theoretically as the first two, but nevertheless seems to be validated by experience. One explanation for this trend is that the number of defects per unit cell tends to grow rapidly as the size of the cell increases. The amount of disorder then tends to be relatively greater for materials with many atoms per unit cell. Another explanation may lie in the breakdown of the concept of a phonon as the number of atoms in the unit cell grows large. Remembering that there are 3n phonon modes, where *n* is the number of atoms in the unit cell, it is reasonable to assume that as *n* grows large these modes will begin to overlap and will no longer be distinguishable. It has been argued by Allen and Feldman[46] that thermal transport in this situation is beginning to resemble thermal transport in a glass.

Fourth, *crystal structures in which the ions are highly coordinated tend to have lower thermal conductivities than crystal structures in which the ions have low coordination*. This is a empirical relationship proposed by Spitzer,[47] based on a compilation of thermal conductivity data on more than 200 semiconductors. We are not aware of any generally accepted explanation for this behavior, although it is interesting that highly coordinated ions are also involved in the reduction in thermal conductivity associated with the “rattling” cations discussed next.

Fifth, *materials in which one or more atoms per unit cell are loosely bound and "rattle" in an oversized cage have low lattice thermal conductivity*. [43] The cage is invariably constructed from many atoms that highly coordinate the rattler. Such rattlers scatter phonons, and can reduce the mean free path of heat carrying phonons to dimensions comparable to the interatomic spacing. The effect on the thermal conductivity is dramatic, as recent work on filled skutterudites[1-2] and germanium clathrates[48] have shown. We will discuss the filled skutterudites in detail in the following session.

Boundary scattering

The five guidelines discussed above are from the chemical composition and lattice structure point of view. They are very useful when people are trying to design new materials or improving the properties of a known material by doping. There are some additional highly successful strategies utilizing boundary scattering as a route for reducing the lattice thermal conductivity of polycrystalline materials to impressively low levels. In 1998, Chen showed that the internal interfaces in nanostructured materials could reduce the thermal conductivities more than their electrical conductivities, based on differences in their respective scattering lengths[13]. The nanostructuring effect has been realized in several different material systems. In 2001, Venkatasubramanian *et al.* [14] produced Bi_2Te_3/Sb_2Te_3 superlattices, and observed maximum *ZT* of ~2.4 for this material using their device. This value is more than twice the *ZT* of the common $(BiSb)_2Te_3$ bulk material. In 2002, Harman *et al.*[15] grew PbSeTe-

based quantum dot superlattice structures by molecular beam epitaxy, which was estimated to have intrinsic *ZT* value of 2.0 at 300K.

In the case of bulk materials, in 2001, Sharp *et al*. estimated the relative magnitudes of the boundary scattering effects on the phonons and charge carriers, and predicted that reducing grain size could greatly enhance the *ZT* value of Si-Ge compounds and half-Heusler alloys[49]. Later experimental research shows that preparing nanosized inclusions or reducing grain size in Si-Ge[16, 50], Bi_2Te_3 based compounds [16, 51-52] and Ti-base half-Heusler alloys[53] is truly effective in reducing the thermal conductivity while keeping the power factors at the similar level.

1.1.5 Filled Skutterudites

Filled skutterudites are a type of very promising thermoelectric materials for intermediate temperature power generation.

The word skutterudite is derived from a town in Norway where minerals with this structure, such as $CoAs_3$, were first discovered. Compounds with the filled skutterudite structure were discovered by Jeitschko and Braun[54] in 1977 and have the general formula of RM_4X_{12} , where *X* was P, As, or Sb; *M* was Fe, Co, Ru, or Os; and *R* was La, Ce, Pr, Nd, or Eu [55-57].

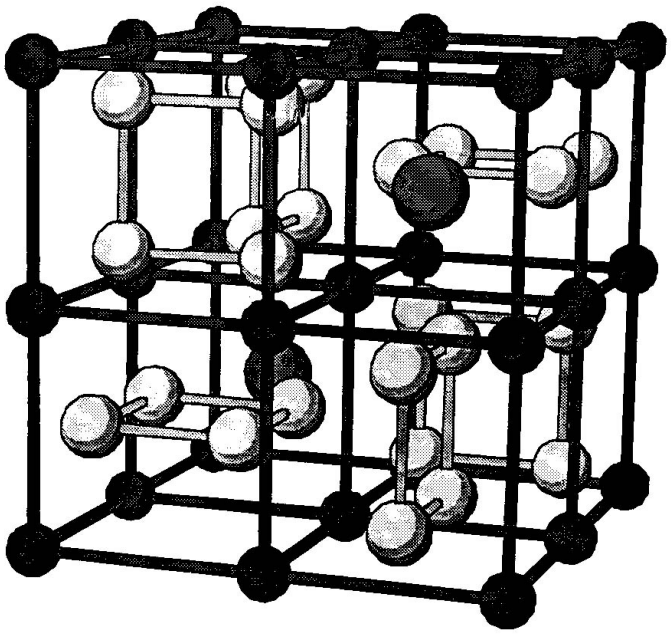

Figure 1.7 Illustration of the filled skutterudite structure. For $Ce_{0.9}Fe_3CoSb_{12}$, the two large spheres represent the Ce atoms, the small dark gray spheres represent the Fe or Co atoms, and the light gray spheres represent Sb atoms. Note the four-membered Sb rings and the large ‘‘cage’’ in which the La resides. This illustration corresponds to the conventional unit cell shifted by the fractional coordinates 1/4, 1/4, 1/4

These compounds are body-centered cubic with 34 atoms in the conventional unit cell and space group *IM3* (Fig. 1.7).[2] This structure can be described as consisting of square planar rings of four pnicogen atoms (X) with the rings oriented along either the (100), (010), or (001) crystallographic directions. The metal (M) atoms form a simple cubic sublattice and the R atoms are positioned in the two remaining ‘‘holes’’ in the unit cell.

Although there are quite a few groups of skutterudites materials, the most popular filled skutterudites are developed based on $CoSb_3$, because these materials show both good mechanical and thermoelectric properties.[4] The base compound, $CoSb_3$, is a p-type narrow gap semiconductor with a highly nonparabolic band structure[58]. The physical properties of $CoSb_3$ single and

polycrystalline materials are sensitive to the preparation procedure, and show very high hole mobility, with the highest value close to 10000 $cm^2V^{-1}s^{-1}$.[5, 59-60] This is very favorable for thermoelectrics. However, the thermal conductivities of these materials are too high for thermoelectric applications.

In 1995, Morelli and Meisner reported a near tenfold reduction in the thermal conductivity by filling the voids in skutterudite lattice with Ce atoms [6]. On the n-type side, Nolas *et al*. reported reductions in the thermal conductivity of Yb filled skutterudites, by as much as 50% [7-8], and hence the *ZT* value of $Yb_{0.2}Co_4Sb_{12}$ was raised above 1 at temperatures higher than 600K. Recently, the thermal conductivity of antimonide skutterudites has been further reduced by filling the voids with two or three different elements.[9-10]

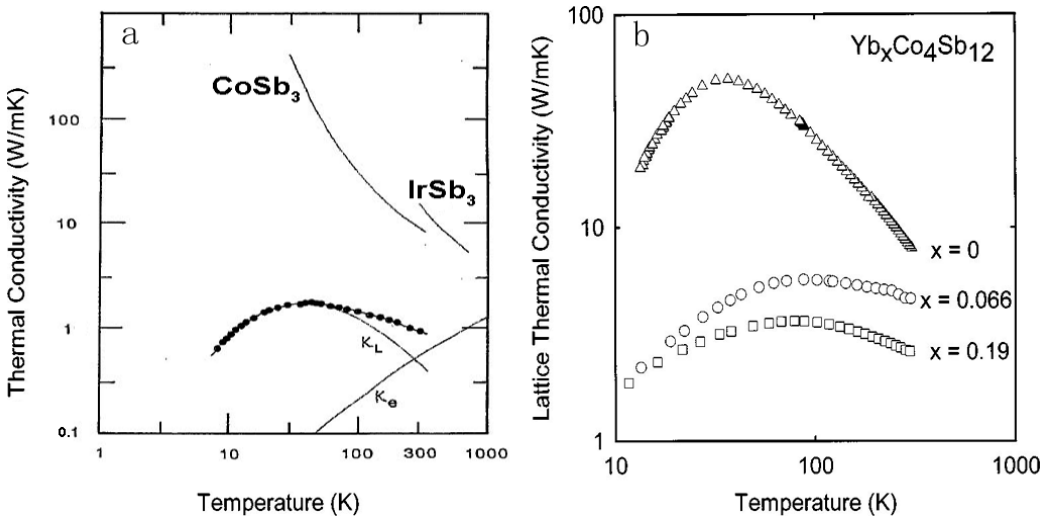

Figure 1.8 The of thermal conductivity of p-type (a, $CeFe_4Sb_{12}$)[6] and n-type (b, Yb_xCoSb_{12})[8] filled skutterudites.

X-ray[54-57] and neutron structure refinements indicate that for many of the compounds the *R* atoms (such as La or Ce) tend to exhibit exceptionally large

thermal parameters corresponding to the rattling of these atoms in an oversized atomic cage. This rattling dramatically reduces the thermal conductivity of these filled skutterudite compounds. This makes the filled skutterudites an excellent approximation of an ideal thermoelectric solid with the good electrical transport properties of a crystal but the poor thermal conduction of a glass, as first proposed by Slack.[43]

The interpretation of this phenomenon is that the filler atoms are weakly bound in a large atomic cage in the filled skutterudites. Such an atom inside the cage ‘‘rattles’’ due to large local anharmonic vibrations, which drastically lowers the lattice thermal conductivity. It is generally believed that the rattling of the rare-earth ion is responsible for reducing the lattice thermal conductivity to a value within two or three times κ_{min}, while preserving the favorable electrical properties. κ_{min} is attained when the mean free path of the heat carrying phonons is comparable to the phonon wavelength and corresponds to the thermal conductivity of an amorphous solid with the same chemical composition. The estimated mean-free path of the heat-carrying phonons at room temperature is ~0.75 nm in filled skutterudites, which agrees well with the nearest-neighbor separation of the rattlers, 0.8 nm.[61] In bulk materials, κ_{min} is the lower limit to the lattice thermal conductivity, although lower values have been seen for interfacial heat transfer.

Although the filler atoms are very effective for reducing the thermal conductivities of antimonide skutterudite materials, the types of filler atoms have to be chosen very carefully, since in some cases the carrier mobility may also be

degraded rather strongly as a consequence of the filling.[6-8, 11-12] For example, the polycrystalline $CoSb_3$ has a hole mobility value of 270 $cm^2V^{-1}s^{-1}$, while the hole mobility drops to about 20 $cm^2V^{-1}s^{-1}$ in $La_{0.05}Co_4Sb_{12}$. Usually, the mobility decreases with higher filling level. The reason for the deterioration of the electronic properties is that the filler atoms introduce extra carriers into the system and hence change the band structure. Lower carrier mobility leads to lower thermopower and/or lower electrical conductivity. In some cases the filling is not capable of improving the *ZT* value, although it does decrease the thermal conductivity quite a lot.[62-63] New techniques have to be introduced to further improve the thermoelectric properties of these materials.

1.2 Non-equilibrium Processing Method

The non-equilibrium processing method used in this work includes a rapid solidification process (melt spinning) and subsequent fast sintering technique (Spark Plasma Sintering).

1.2.1 Melt spinning

Melt spinning is a technique used for the rapid cooling of liquids. A wheel is cooled internally, usually by water or liquid nitrogen, and rotated. A thin stream of liquid is then dripped onto the wheel and cooled, causing rapid solidification (Fig. 1.9). This technique is used to develop materials that require extremely high cooling rates in order to form, such as metallic glasses. The cooling rates achievable by melt-spinning are on the order of 10^4–10^7 Kelvin per second (K/s).

The concept of the melt spinner was developed by Pond and Maddin in 1969, whereby liquid was quenched on the inner surface of a drum[64], then later as a continuous casting technique by Liebermann and Graham[65]. However the melt spinner is only able to produce small thin ribbon shaped specimens, some as thin as 10 micrometers. This limits melt spinning to mainly production of research specimens for alloys with high critical cooling rate, which are difficult to fabricate with other techniques. Furthermore, since the system use radio frequency heating power to melt material, the materials should have relatively low electrical resistivity.

In this work, melt spinning machine (Model 2460, Serial #8, Edmund Bühler GmbH) was used to produce ribbons with nano-sized grains before the final sintering/densification step.

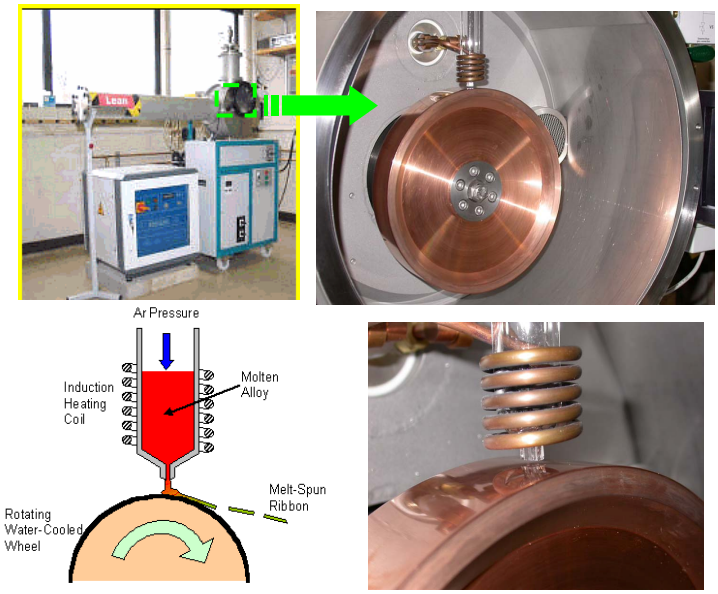

Figure 1.9 The melt spin machine used in this work, the cartoon at the down-left corner shows how it works.

1.2.2 Spark Plasma Sintering (SPS)

The SPS process is based on the electrical spark discharge phenomenon: a high energy, low voltage spark pulse current momentarily generates spark plasma at high localized temperatures (from several to ten thousand ºC) between the particles, and results in optimum thermal and electrolytic diffusion (Figure 1.10). [66] SPS sintering temperatures range from low to over 2000 ºC which are about 200 to 500 ºC lower than that required in the conventional sintering process. Vaporization, melting and sintering are completed in short periods of approximately 5 to 20 minutes, including temperature rise and holding time.

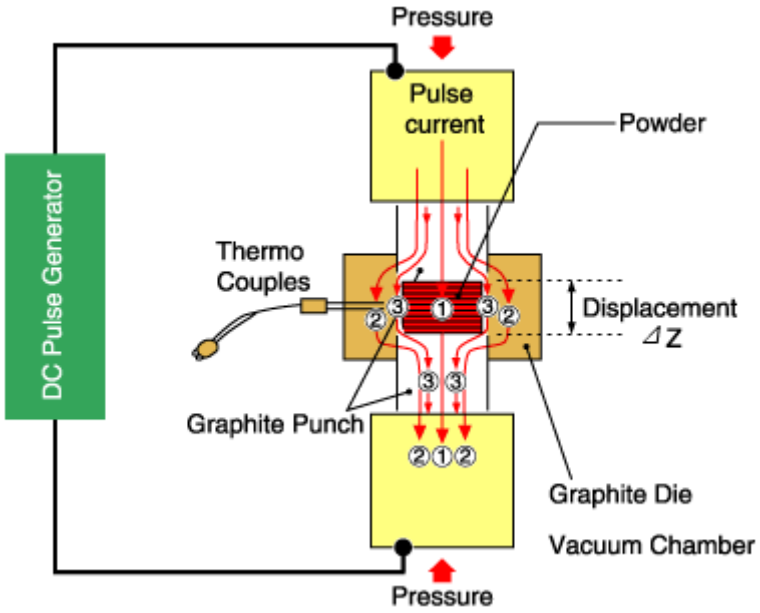

Figure 1.10 The working diagram of a SPS device

The Spark Plasma Sintering (SPS) process is a pressure assisted pulsed current sintering process utilizing ON-OFF DC pulse energizing. By a repeated application of an ON-OFF DC pulse voltage and current between powder materials, the spark discharge point and the Joule heating point (local high temperature-state) are transferred and dispersed to the overall specimen. The homogeneously repeated heating phenomena during the ON stage results in efficient sintering at low power consumption. The Spark Plasma Sintering (SPS) process concentrates high energy pulses at the point of inter-granular bonding and offers significant improvements over conventional hot-press and hot isostatic press sintering.

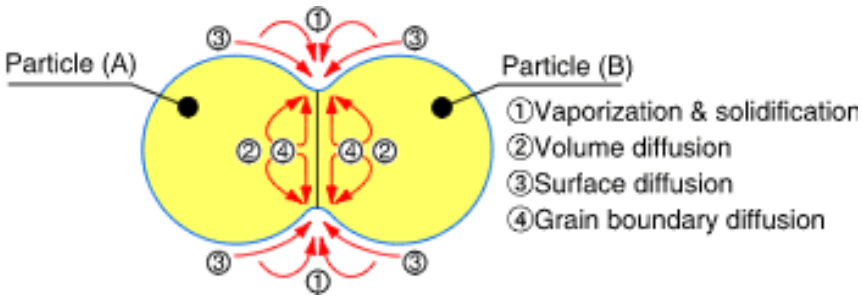

Figure 1.11 The mechanism of neck formation during SPS sintering

The mechanism of neck formation during the Spark Plasma Sintering (SPS) process is shown in Fig. 1.11.[66] When spark discharge appears in the gap between the particles of a material, a local high temperature state of several to ten thousand ºC momentarily occurs. This causes vaporization and the melting of the surfaces of the powder particles during the Spark Plasma Sintering process. Constricted shapes or “necks” are formed around the contact area between the particles. A density of over 99% is achievable in a sintered pellet, thanks to the gradual development of these necks and plastic transformation which progresses during sintering. Since only the surface temperature of the particles rises rapidly by self-heating, grain growth of the starting powder materials is minimized. Therefore, by employing this technique, making bulk material with amorphous structure or nano-crystallization becomes a possible task.

2 Experiments

2.1 Sample Synthesis

2.1.1 Ingot Preparation

The filled skutterudite ingots were prepared by mixing stoichiometric amounts of high purity rare-earth elements, such as Ce (ingot, 99.8% min, Alfa Aesar), Fe (granules, 99.98%, Alfa Aesar), Co (Cobalt Slug 99.95%, Alfa Aesar) and Sb (shots, 99.9999%, Alfa Aesar). The electrical properties of filled skutterudite materials are very sensitive to oxidization. To make high quality ingots, a complete protocol has been developed.

First, the oxide layer on the surface of a Ce chunk was removed with the protection of oil. Then the chunk was cut into small pieces and cleaned with acetone and pure alcohol. The Ce pieces were quickly weighed and put into a glove box. Subsequently all other elements were then weighed and loaded into a carbon coated quartz tube together with Ce pieces in the glove box. A Parafilm was then used to cover opening of the tube and make sure the mixture was protected by Ar gas until the tube was sealed. In the final step, the quartz tube was sealed under 1/3 atm Ar gas. Figure 2.1 shows a sealed tube.

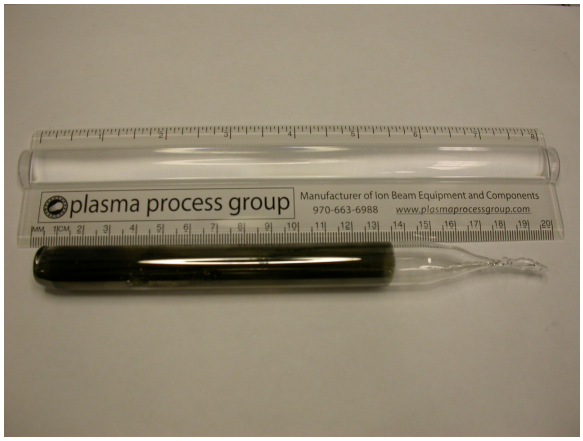

Figure 2.1 Filled skutterudite sealed in carbon coated quartz tube

The quartz ampoule was heated to 600˚C at 2˚C/min, left for about 3 hours, then slowly heated to 1050 ˚C at 0.5˚C/min and left at this temperature for about 24 hours. It is important to slowly heat the tube because of the highly exothermic reaction between the Ce and Sb. The quartz ampoule containing the homogenous molten liquid was removed from the furnace at 1050˚C and quenched into a water bath.

A quenched ingot was removed from the quartz tube and cleaned with a wire brush and ultrasonic cleaner with alcohol to remove small amounts of carbon from its surface. A cleaned ingot is shown in Fig. 2.2.

Figure 2.2 An example of quenched filled skutterudite ingot

To prepare the conventional sample, the quenched ingot was placed in a furnace and annealed at 700˚C for 30h in order to form the correct crystallographic phase. The completely reacted ingot was removed from the quartz tube and cleaned with a wire brush and alcohol to remove small amounts of carbon from the surface.

2.1.2 Melt Spinning

The ingot was cut into several pieces. Then about 10 grams of the pieces were loaded into a quartz crucible for melt spinning. Figure 2.3 shows typical melt-spun ribbon.

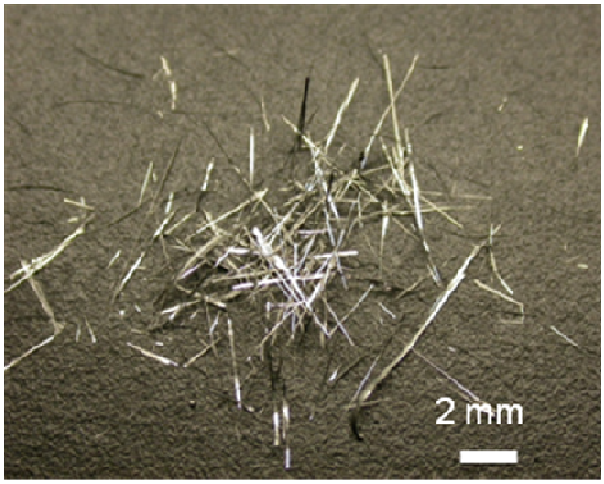

Figure 2.3 Typical melt spun ribbon of filled skutterudite

During the melt spinning, the highest cooling rate happened at the contact surface between the ribbon and the copper roller. So, the thinner the ribbon, the better is the cooling effect. The thickness of the ribbons for specific materials depends on two parameters in our experiment.

1) The surface linear speed of the copper roller.

Higher linear speed results in thinner ribbons. In this work, the surface linear speed of the copper roller was adjusted at 30 m/s.

2) The flow speed of the molten material.

The optimum flow speed was achieved by choosing right nozzle length and adjusting the pressure between the chamber and the external pressure tank.

We investigated the effect of pressure difference on ribbon thickness. A number of pressure differences between the chamber and the external pressure tank have been tried, while all other parameters were held fixed. The results are shown in Fig. 2.4. The ribbon thickness increases with pressure difference. In order to achieve fastest quench rate, a pressure difference of 0.4 atm has been used for the filled skutterudite samples we made.

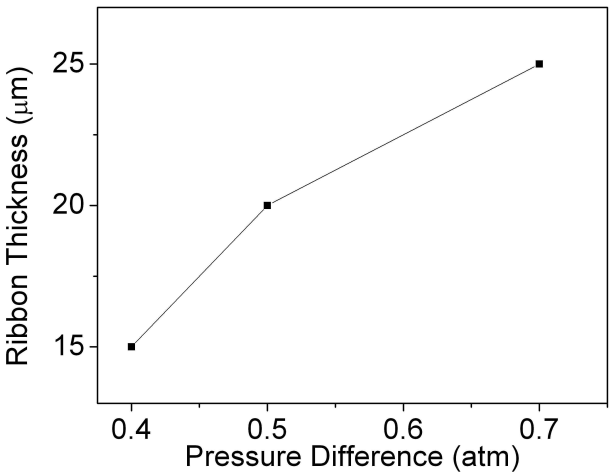

Figure 2.4 The pressure dependence of melt spun ribbon thickness.

2.1.3 SPS sintering

The spun ribbons and annealed ingot were ground into powder, then loaded into graphite dies and sintered into half inch pellets using SPS. The

sintering work was done by Dr. Xun Shi and Dr. Jung Young Cho at the Research Center of General Motor Co..

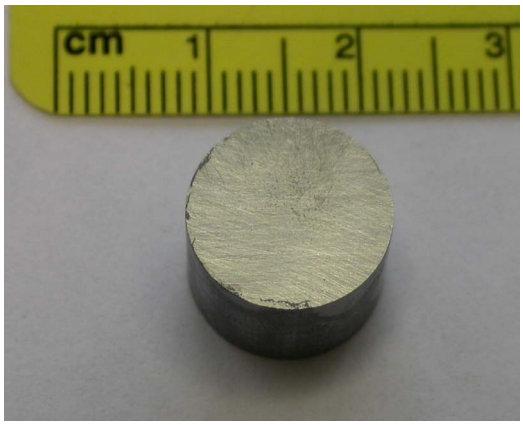

Figure 2.5 SPS sintered filled skutterudite pellet

For all samples, the final sintering temperature and pressure were 620 ˚C and 50 MPa respectively. The temperature was gradually increased to around 550 ~ 580 ˚C at a rate of ~70 ˚C / min. Then the pressure was applied at that temperature. The temperature was slowly increased up to the final temperature (~ 620 ˚C) and held for 2 minutes to ensure the complete sintering. The total sintering time was within 13~15 min for all samples. Then the power was shut off, and cooled to 200 ˚C in 10 minutes. Figure 2.5 shows the SPS sintered pellet. The sintered pellets were designated as MS and AN respectively.

2.2 Phase and structure analysis

2.2.1 X-ray powder diffraction

X-ray powder diffractometry (Philips 3100E) with Cu Kα radiation was used to investigate the phases in the studied samples. Both melt spun ribbon and

sintered pellets were ground into powder using an agate mortar. Then the powder was placed on the surface of a glass plate with the help of Vaseline petroleum jelly. The voltage and current we used for X-ray generation are 40 V and 30 A respectively. Scans are obtained typically from 10 to 70 degrees 2theta, with a step size of 0.02 degrees 2theta and a count time of 1 seconds.

2.2.2 Scanning Electron Microscope (SEM)

The freshly cut sample surfaces were studied with a Hitachi S4800 Scanning Electron Microscope, in order to compare differences in grain size between the MS and AN samples.

2.2.3 Transmission Electron Microscope (TEM)

TEM samples of melt-spun ribbons were prepared by grinding the brittle ribbons into very fine powders. A dilute alcohol-powder suspension was then prepared and a drop of it was placed onto a lacey film coated copper grid as the sample.

The sintered bulk TEM samples were prepared by a traditional dimpling method. After mechanically polishing and dimpling to a thickness of about 20 μm, the samples were thinned to the electron transparent thickness using an ion mill system at low milling angles (6-12^{o}). The specimen stage of the ion mill system was simultaneously cooled by liquid nitrogen, which helped to avoid local specimen overheating during the milling process in order to eliminate artifacts. All TEM samples were ion milled below - 90 ^{o}C.

The TEM work presented in this dissertation was done by Miss Juan Zhou in our group.

2.3 Thermoelectric Properties Characterization

2.3.1 Low temperature thermoelectric properties measurement

The thermoelectric properties data below 400K were collected using Physical Properties Measurement System (PPMS, Quantum Design, Figure 2.6).

Figure 2.6 Physical Properties Measurement System (PPMS, Quantum Design)

2.3.1.1 The resistivity measurement

The resistivities of the samples were measured in PPMS using a standard 4-probe method. A rectangular bar was cut from the sample and polished. The typical geometry was $0.5\times0.5\times5$ mm^3. The samples were fixed on a very thin (0.2

mm) glass substrate. Then four gold wires (0.002” in diameter) were attached to the sample as current and voltage leads using silver paint. The whole assembly was then mounted onto a resistivity sample puck, with the gold wires soldered on the contact posts.

2.3.1.2 Thermopower and thermal conductivity measurement

The thermopower and thermal conductivity below 400K were measured in PPMS using its Thermal Transport Option (TTO). Samples could be either in a 2-probe configuration or 4-probe configuration. In order to make a 2-probe sample, a rectangular bar with the geometry of 3×3×2 mm^3 was cut from the pellet and polished using sand paper. A typical size for 4-probe sample was 1×2×9 mm^3. Gold-coated copper bars were attached onto samples as leads using silver epoxy (H20E, Epoxy Technology, Inc).

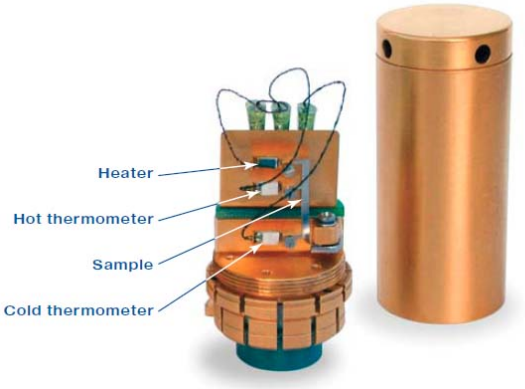

Figure 2.7 Thermal Transport sample puck and radiation shield

A PPMS TTO sample puck (Fig. 2.7) uses a 2000 Ohm heater and two small and highly accurate Cernox chip thermometer. For thermal conductivity and Seebeck coefficient measurements, heat is applied to one end of the sample by running current through the heater (Q+/-). The temperature T_{hot} and T_{cold} are

measured at the thermometer shoes. Also, during the heat pulse, the Seebeck voltage ($\Delta V=V_+-V_-$) is monitored. Heat exits the sample to the cold foot.

Thermal conductivity, κ is measured by applying heat from the heater shoe on one end of the sample in order to create a specific temperature differential between the two thermometer shoes. The TTO system dynamically models the thermal response of the sample to the low-frequency, square-wave heat pulse, thus expediting data acquistition. κ then can be calculated directly from the applied heater power, resulting ΔT, and sample geometry.

Seebeck coefficient (also called the thermopower) α is determined by creating a specified temperature drop between the two thermometer shoes – just as it does to measure thermal conductivity. However, for Seebeck coefficient the voltage drop created between the thermometer shoes is also monitored. The additional voltage-sense leads on the thermometer shoes are connected to the ultra-low-noise preamplifier of the ACT system.

The TTO system includes two measurement modes:

1) Single Measurement Mode

In Single Measurement Mode, data is first taken in the heater “off” state once the system settles. After the user–specified heater power is applied, the system waits for the selected equilibrium condition before making the final measurement in the heater “on” state. This mode is slow because it requires that the system reaches a steady state in both the heater “off” and “on” states, which also implies that temperature or field slewing is unavailable. The advantage of the Single Measurement Mode is that no subtle curve-fitting calculations are required,

so interpretation of the raw data is in principle more straightforward. Researchers who study thermal transport properties usually employ this steady-state technique because of its simplicity and robustness.

2) Continuous Measurement Mode

In Continuous Measurement Mode, measurement are being taken continually and the adaptive software is adjusting parameters (such as heater power and period) to optimize the measurement. This mode is amenable to slow sweep of system variables such as temperature or magnetic field, and it is often the most rapid way of obtaining data because you do not have to wait for the system to reach equilibrium before measuring. The continuous mode is also expedited by the use of a sophisticated curve-fitting algorithm that determines the steady-state thermal properties by extrapolating from the response to a relatively short (typically several minutes) heat pulse.

Because Single Measurement Mode is very time consuming, most of the TTO measurements were performed using the Continuous Mode, and the single mode was used to confirm the data at several different temperature.

1.1.1.1 Hall Effect Measurement

Hall coefficient data were taken in the temperature range from 5 to 300 K and in magnetic fields up to 9T using a four-wire configuration. The samples were polished down to 130 μm in thickness to enhance the signal. They were subsequently mounted on a resistivity measurement sample puck. The highest current, 5 mA, was used for the measurement.

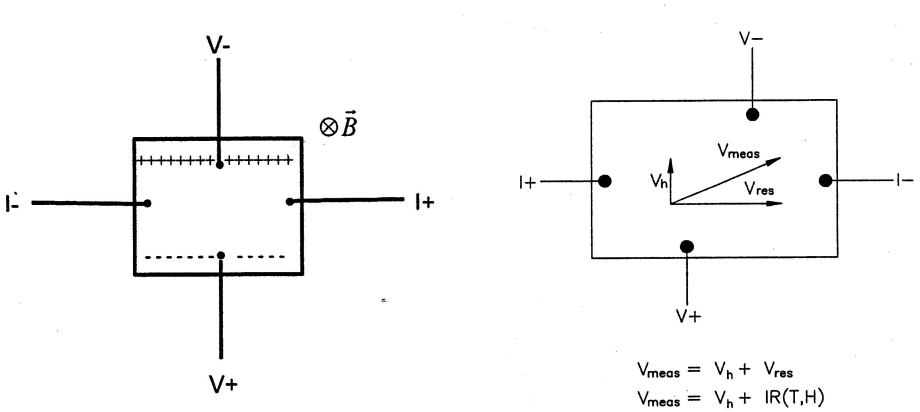

Figure 2.8 Four-wire Hall effect measurement

The potential across the two voltage leads includes two parts. One is the hall potential, and the other one comes from the sample resistance, as shown in Fig. 2.8,

$$V_{meas} = V_h + I \times R_{res} = V_h + I \times R(T, H) \tag{2.1}$$

where, V_{meas}, V_h and I are the voltage we measured, real hall voltage and the current we used for measurement. R is the sample resistance along the current direction between the two voltage leads. We found that the magneto-resistance of filled skutterudites we made was very small. At a specific temperature and current, the R can be treated as a constant.

Given $V_h = \frac{R_h I}{d} B$, and $V_{meas} = I \times R_{meas}$, where d is the thickness of the sample, R_h is the hall coefficient, B is the field and R_{meas} is the resistance we measured using PPMS, equation 2.1 can be rewrite as:

$$R_{meas} = \frac{R_h}{d} B + R \tag{2.2}$$

If we plot R_{meas} vs. B, it would be easy to derive R_h from the slop of the line.

Usually the Hall voltage is much smaller than the voltage from sample resistance. To minimize the error, we repeated the measurement three times for each specific field and temperature. Then linear fitting was used to obtain the slope for each set of data.

2.3.2 High temperature thermoelectric properties measurement

2.3.2.1 High temperature Seebeck Coefficient and Resistivity Measurment

The thermopower above room temperature up to 800K was measured on a ULVAC ZEM-3 Seebeck Coefficient / Electric Resistance Measuring System, as shown in Fig. 2.9.

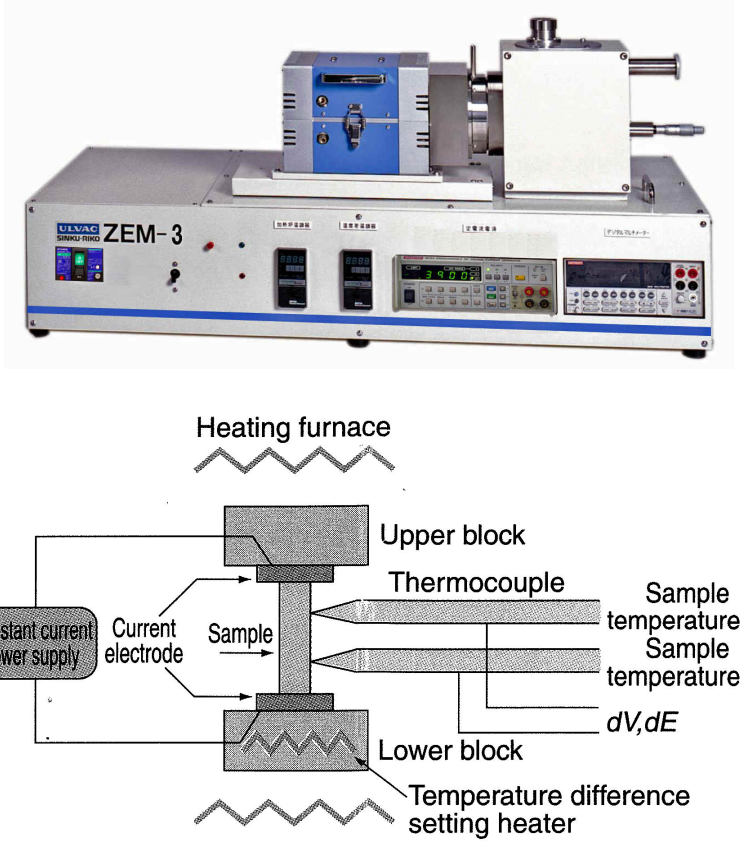

Figure 2.9 A ULVAC ZEM-3 Seebeck Coefficient / Electric Resistance Measuring System and the schematic diagram for the measurement

The samples were set in a vertical position between the upper and lower blocks in the heating furnace. While the sample is heated to, and held, at a specified temperature, a heater embedded in the lower block provided a temperature gradient across it. The Seebeck coefficient was calculated upon measuring the upper and lower temperatures, T1 and T2, with the thermocouples pressed against the side of the sample, followed by measurement of the thermal electromotive force *dE* between the same wires on one side of the thermocouple.

Electric resistance was measured by the dc four-probe method, in which a constant current *I* was applied to both ends of the sample. The voltage drop ΔV between the same wires of the thermocouple was determined by subtracting the thermo-electromotive force between the thermocouples at the same side.

2.3.2.2 High Temperature Thermal Conductivity Measurement

The thermal conductivity (κ) was calculated from the measured thermal diffusivity *D*, specific heat at constant pressure C_p and density *d* using the relationship $\kappa = DC_pd$. The Thermal diffusivity was measured by the laser flash method (Anter Flashline^{TM} 4020 Thermal Properties Analyzer) and specific heat was determined using a Q2000-DSC TA Instrument. The density of the sample was estimated by dividing the mass of polished cubic sample by its volume.

1.1.1.1.1 Thermal Diffusivity

The thermal diffusivity (*D*) of a medium is the thermophysical property that determines the speed of heat propagation by conduction during changes of

temperature with time. The higher the thermal diffusivity, the faster the heat propagates. The thermal diffusivity is related to the thermal conductivity (κ), specific heat (C_p) and density (d) as follows:

$$D = \frac{\kappa}{dC_p} \tag{2.3}$$

According to the above definition, the thermal diffusivity affects any conductive transient heat transfer process within the medium. It has the dimension length²/time and is expressed in the unit m²/s. The most popular method used for measuring thermal diffusivity is the flash method. It has the advantage of being fast while providing values with excellent accuracy and reproducibility. After the sample has been stabilized at a desired temperature T_0, a nearly instantaneous pulse of energy (usually laser or other discharge source) is deposited on its front face, and the temperature increase $dT(t)$ on the rear face of the sample is recorded as a function of time (Fig. 2.10).[67] The thermal diffusivity was then determined from this thermogram.

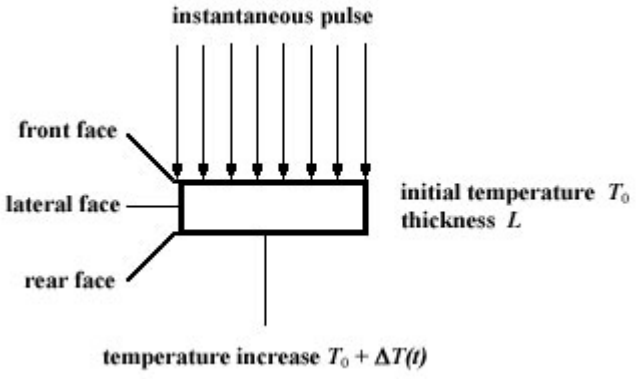

Figure 2.10 Schematic of the flash method

The characteristic shapes of the temperature increase curves are depicted in Fig. 2.11.[67] If no heat loss is involved, the temperature of the rear face will

rise to a maximum and remain at that level indefinitely (curve A). However, with increasing heat losses, the temperature on the rear face decreases after reaching a maximal value (curves B and C).

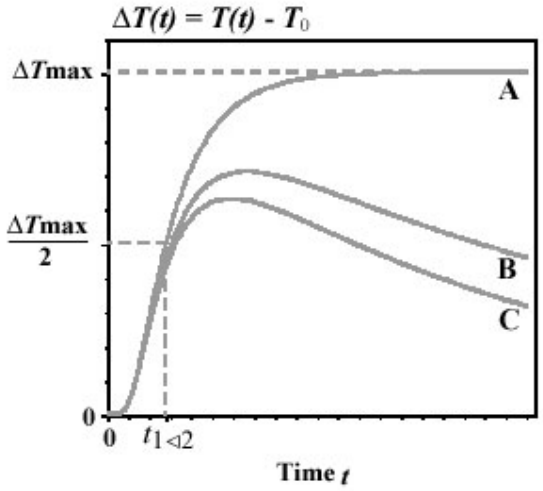

Figure 2.11 Temperature increase for various experimental conditions

The original method proposed by PARKER assumes an isotropic and adiabatic sample (no heat loss). The thermal diffusivity is determined from the thickness, L, of the sample and the time, $t_{½}$, the thermogram takes to reach half of the maximal temperature increase:

$$D = 0.1388\frac{L}{t_{1/2}} \tag{2.4}$$

Since this method assumes ideal conditions of adiabatic sample and instantaneous pulse heating, it is somewhat limited in applicability. To make it more suitable to experimental conditions, other methods have been introduced over the years, which account for heat losses, finite pulse duration, non-uniform pulse heating and composite (non-homogeneous) structures.

Figure 2.12 Anter Flashline™ 4020 Thermal Properties Analyzer

Figure 2.12 shows the instrument we used for thermal diffusivity measurement.[68] The inset at the up-right corner shows the graphite sample holder. The samples around 1 mm in thickness were cut from the ϕ ½" pellets for the measurement.

2.3.2.2.1 Specific Heat Measurement

The specific heat of the samples was determined using a Q2000-DSC TA Instrument with flowing N_2 gas. A reference measurement run was performed first using an Al_2O_3 disk with 4mm in diameter. The samples were cut into similar size and shape for the accuracy of the measurement.

3 Enhanced Thermoelectric Properties in Non-equilibrium Synthesized $Ce_{0.9}Fe_3CoSb_{12}$ Filled Skutterudites

$Ce_{0.9}Fe_3CoSb_{12}$ is a well known p-type filled skutterudite with perhaps the highest known *ZT* value in its category.[2] It is interesting to see if we can further improve the thermoelectric properties of this material. In this part of work, we prepared this material by both non-equilibrium (melt-spinning followed by SPS) and equilibrium process (long term annealing). Substantial improvement in the power factor with a simultaneous reduction in the thermal conductivity was observed in the former one.

3.1 X-ray Powder Diffraction

Figure 3.1 shows very similar X-ray diffraction (XRD) patterns of both MS and AN samples, with predominantly filled skutterudite phase (diffraction peaks marked by X). A trace amount of impurity, $Fe(Co)Sb_2$, was detected in both samples, denoted by the arrows in the figure.

Interestingly, the MS samples appear to have less of impurity, as evident from the lower impurity peaks in the XRD analysis, suggesting this rapid direct conversion process is very effective. Compared with the conventional solid state reaction and long term annealing method, the processing time for melt-spinning and SPS was reduced by several orders of magnitude, and is clearly advantageous for cost-saving in the industrial production.

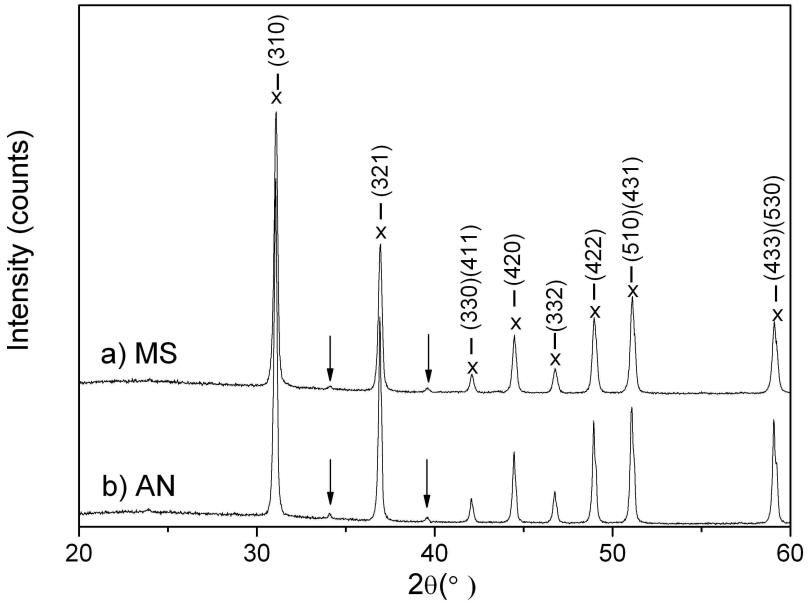

Figure 3.1 X-ray powder diffraction pattern of filled skutterudite $Ce_{0.9}Fe_3CoSb_{12}$ prepared by (a) non-equilibrium (MS) and (b) equilibrium (AN) synthesis. The Miller indices for several of the peaks are marked by X. The arrows denote the $Fe(Co)Sb_2$ impurity peaks observed in the samples.

3.2 Micro-structural Observation by SEM

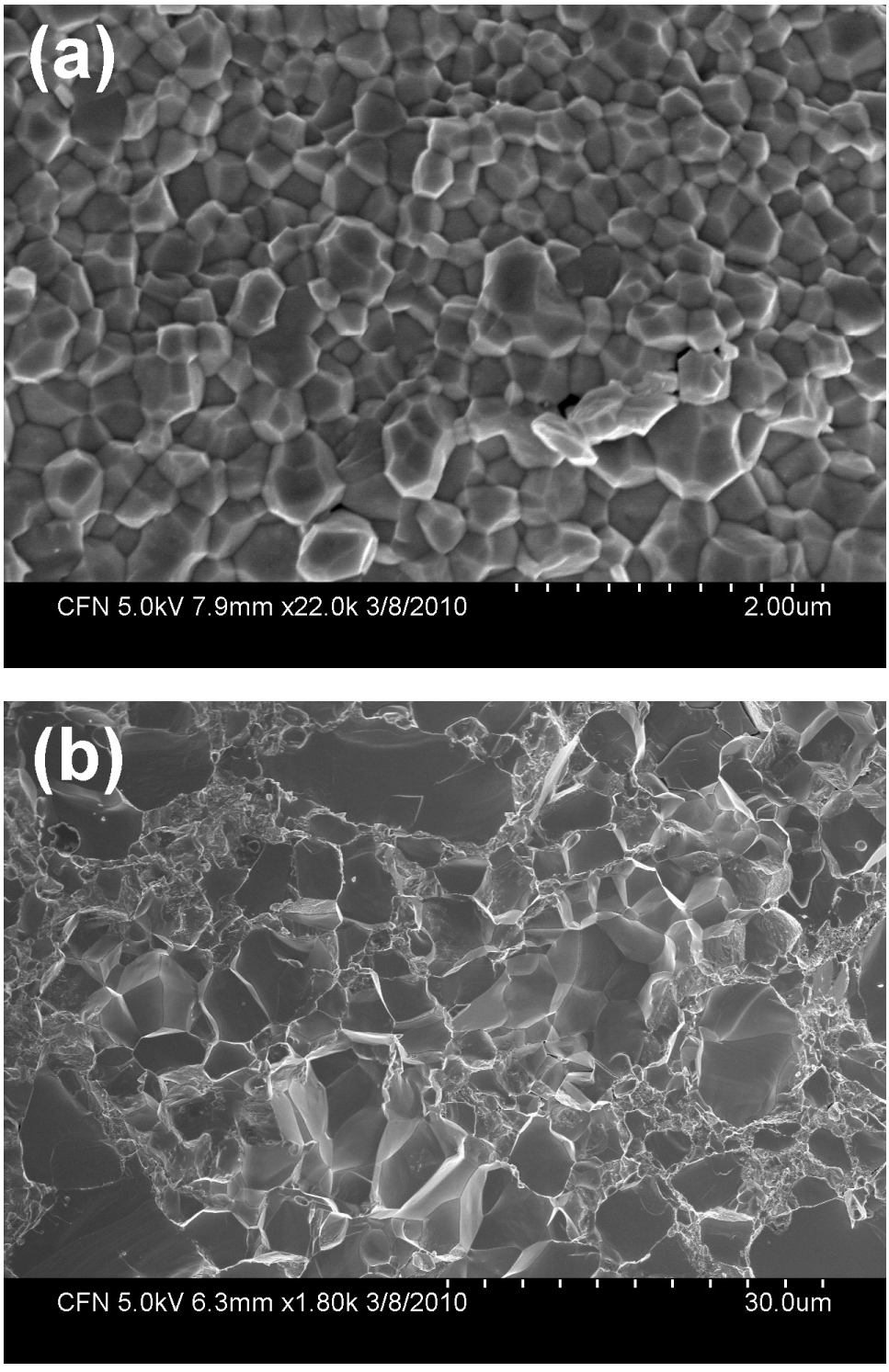

Figure 3.2 SEM images of fracture surfaces of the (a) MS and (b) AN samples

Figure 3.2(a) shows the fracture surface of MS samples. The sample is very dense and has very small grain size. The grain size in the MS samples varies from 150 nm to 500 nm. For a comparison, Figure 3.2(b) shows the fracture surface of AN sample, which has very large grain size distribution. The smallest grains observed in the AN sample are around 10 μm, approximately two orders of magnitude bigger than that in the MS sample.

Remarkably, the fracture surface of the MS sample goes through its grain boundaries, while the fracture surface of the AN sample prefers to go through its grains. That means, when a MS sample breaks, the fracture prefers to propagate along its grain boundary. Thus fractures would need to propagate a longer distances around grains rather than cutting though grains. Usually, a material with this character could have better fracture strength due to the much higher energy cost of fracture propagation.

3.3 Thermoelectric Properties

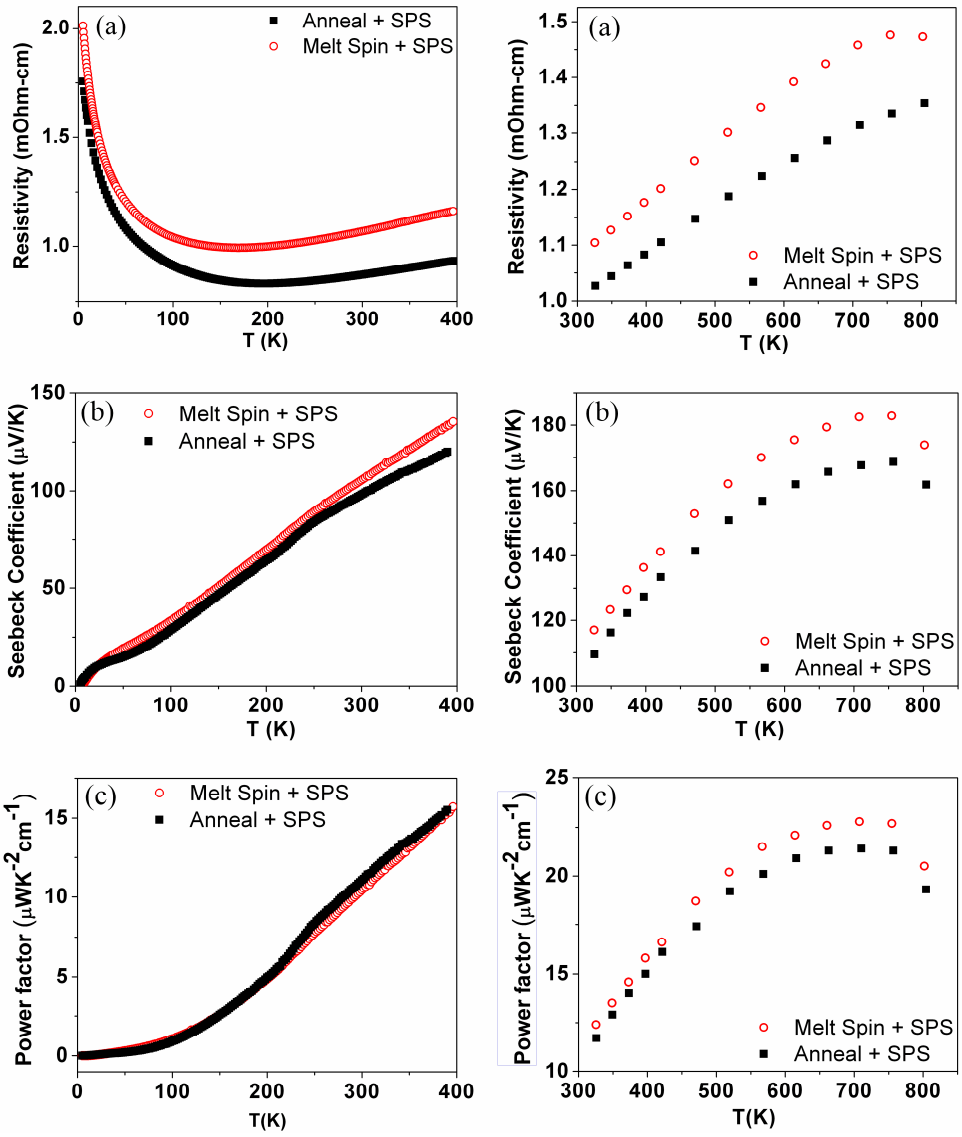

Figure 3.3 Temperature dependences of (a) ρ, (b) S and (c) power factor for the AN (solid square) and MS samples (open circle)

The temperature dependences of ρ, S and power factor for the AN and MS samples are shown in Figure 3.3. Both AN and MS sample show a semiconductor to metal transition at about 200K. Below this temerature, the resistivities decrease quickly with increasing temperature. After the transition, both samples show metallic conduction behavior up to 800K. The MS sample has

highter ρ. The much smaller grain size and hence much higher grain boundary density may play an important role here.

The thermopowers for the MS and AN samples are very close at low temperature, although the MS sample shows a slightly higher *S* above 30K. The difference between *S* for the two samples become obvious above 250K, and this difference increases with increasing temperature until the *S* curves reach their peak at around 750K. Despite the higher electrical resistivity, the higher *S* in the MS sample results in ~ 10% higher power factor compared to the AN sample. Similar power factor enhancement has been reported in $Si_{0.8}Ge_{0.2}B_{0.016}$ nanocomposite material, and was explained as a result of strong interface scattering,[50] which likely alters the energy dependence of the electron scattering rate.

Figure 3.4 displays the temperature dependence of κ, κ_L and *ZT* for the AN and MS samples. Above room temperature, the electronic contribution to the total thermal conductivity is about 25%. Compared to the AN samples, the total κ of the MS sample is reduced by 30% at 50K. The difference decreases with increasing temperature (20% at room temperature and 10% at 800K). Interestingly, a greater reduction of lattice thermal conductivity was found in the MS samples, as shown in Fig. 3.4 (b), where nearly 20% reduction was observed at high temperatures. This is likely the result of smaller grain size in the MS samples, where the greatly increased number of grain boundaries provides additional phonon scattering.

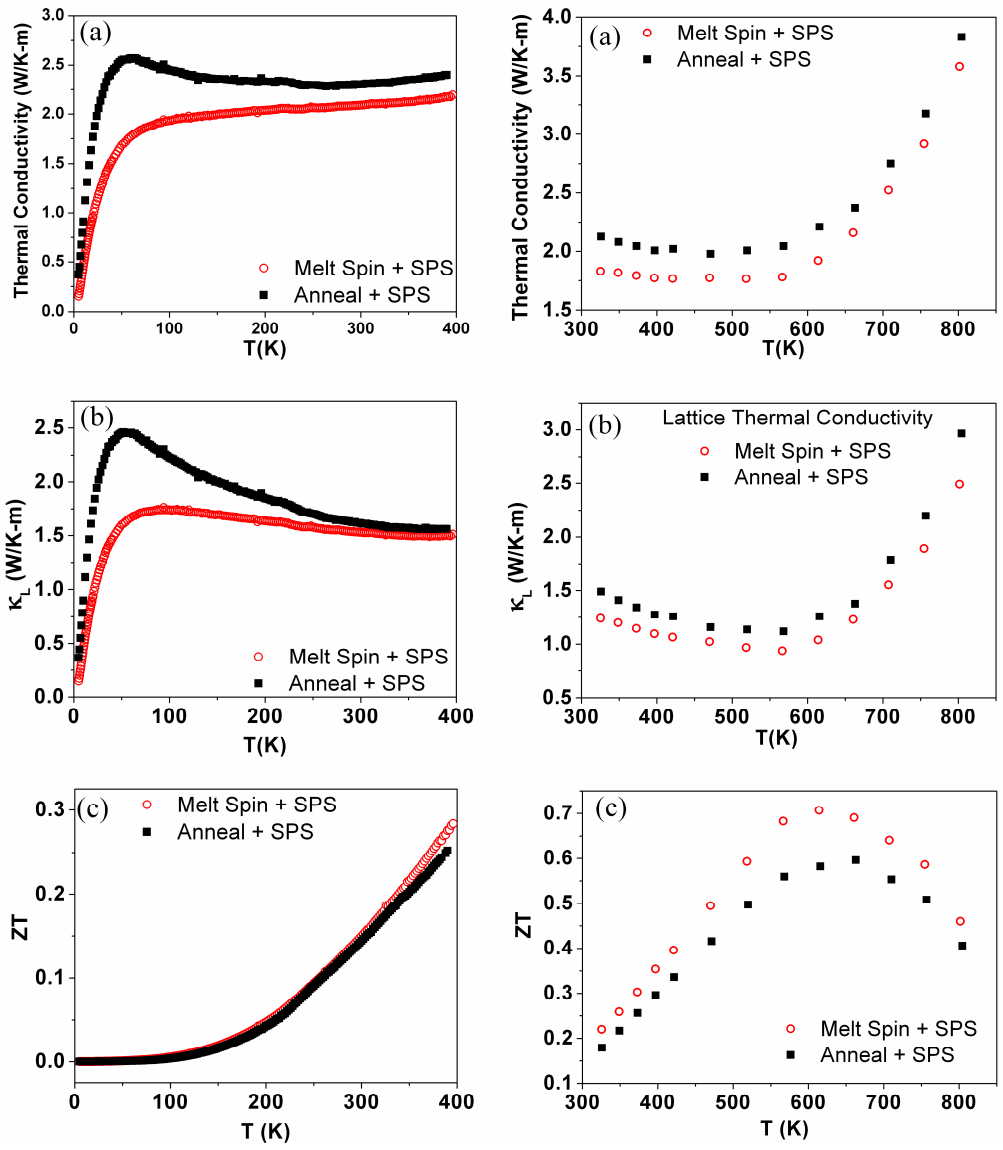

Figure 3.4 Temperature dependence of (a) κ, (b) κ_L and (c) *ZT* for AN (solid square) and MS samples (open circle)

Because of the much higher resistivity, we did not observe the *ZT* enhancement at low temperature. The *ZT* value of MS sample starts to exceed that of the AN sample from about 300K (considering the error on thermal conductivity measurement above 100K using PPMS TTO option, it should be lower than

300K). Above room temperature, the MS sample shows higher *ZT* values over the entire temperature range, with a peak enhancement over 15% around 625K.

3.4 Summary

In this chapter, we presented a comparative study on the thermoelectric properties of the p-type filled skutterudite $Ce_{0.9}Fe_3CoSb_{12}$ prepared by both non-equilibrium and equilibrium methods. It is found that the rapid conversion processing in the non-equilibrium method produces higher performance materials by simultaneously increasing the power factor and reducing the thermal conductivity. The *ZT* value was enhanced over the temperature range from 300K to 800K, with an enhancement of above 15% at 625K. In addition, the structural analysis suggests better mechanical properties can be expected in the non-equilibrium processed samples. This study demonstrated that this non-equilibrium synthesis route was very effective in producing high performance thermoelectric materials.

4 Strong Impact of Grain Boundaries on the Thermoelectric Properties of Non-equilibrium Synthesized p-type $Ce_{1.05}Fe_4Sb_{12.04}$ Filled Skutterudites with Nanostructure

$Ce_{1.05}Fe_4Sb_{12.04}$ is a classical p-type filled skutterudite with well known properties. It is the first type of filled skutterudite that has been reported to have low thermal conductivity due to filling. In Chapter 3, we have shown that the non-equilibrium synthesis method is very effective in reducing the grain size in the $Ce_{0.9}Fe_3CoSb_{12}$ filled skutterudite, and hence improving the thermoelectric properties. $Ce_{1.05}Fe_4Sb_{12.04}$ has lower electrical resistivity compared to $Ce_{0.9}Fe_3CoSb_{12}$. Yet, its lower thermopower and higher thermal conductivity result in a lower *ZT*. In this chapter, we present a comparative study on $Ce_{1.05}Fe_4Sb_{12.04}$ filled skutterudites prepared using non-equilibrium synthesis method and conventional long-term annealing method. The results have shown that the non-equilibrium synthesis method is not only capable of reducing grain size, but also of achieving cleaner grain boundaries in the material. The cleaner

grain boundary helps carrier transport and leads the lower resistivity in the sample we made.

4.1 X-ray Powder Diffraction

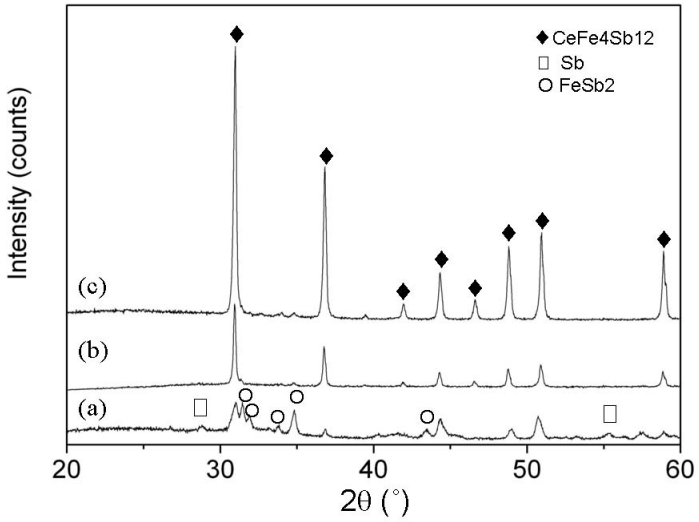

Figure 4.1 A comparison of X-ray diffraction spectrum of melt spin ribbon (a), non-equilibrium synthesized pellet (b) and equilibrium synthesized pellet (c).

The XRD patterns for melt-spun ribbons, MS and AN sample are compared in figure 4.1. According to the peaks, the melt-spun ribbon is a mixture of filled skutterudite, $FeSb_2$ and Sb. The broadened peaks indicate that the characteristic grain size is very small.

Both sintered samples predominantly comprise of a filled skutterudite phase. Interestingly, although the melt spun ribbon is a mixture of $FeSb_2$, Sb and filled skutterudite phase with very small grain size, they have been fully converted to filled skutterudite phase by a very quick sintering process using SPS. Furthermore, the MS samples appear to have less of impurity, as evident with

fewer and lower impurity peaks in the XRD analysis, which suggests this rapid direct conversion process is very effective. Compared to the conventional solid state reaction and long term annealing method, the processing time for the melt-spin and SPS was reduced by several orders of magnitude, and is clearly advantageous for cost-saving in the industrial production.

4.2 Thermoelectric Properties

Fig. 4.2 compares the temperature dependences of ρ, S, and power factor for the MS and AN samples. The figures on the left side show the low temperature data measured using PPMS. Both samples show metal-like behavior except for the temperature regime between 150 and 200K. Both S and ρ curves of the two samples cross at 80K. Below this temperature, the MS sample has higher ρ and lower S compared to the AN sample. Above this temperature, the resistivity of the MS sample becomes lower than that of the AN sample, and the difference continues to increase with temperature. Above 150 K, this resistivity difference maintains the same level with the increase of temperature, while the thermopower of both samples are virtually the same (within 5%).

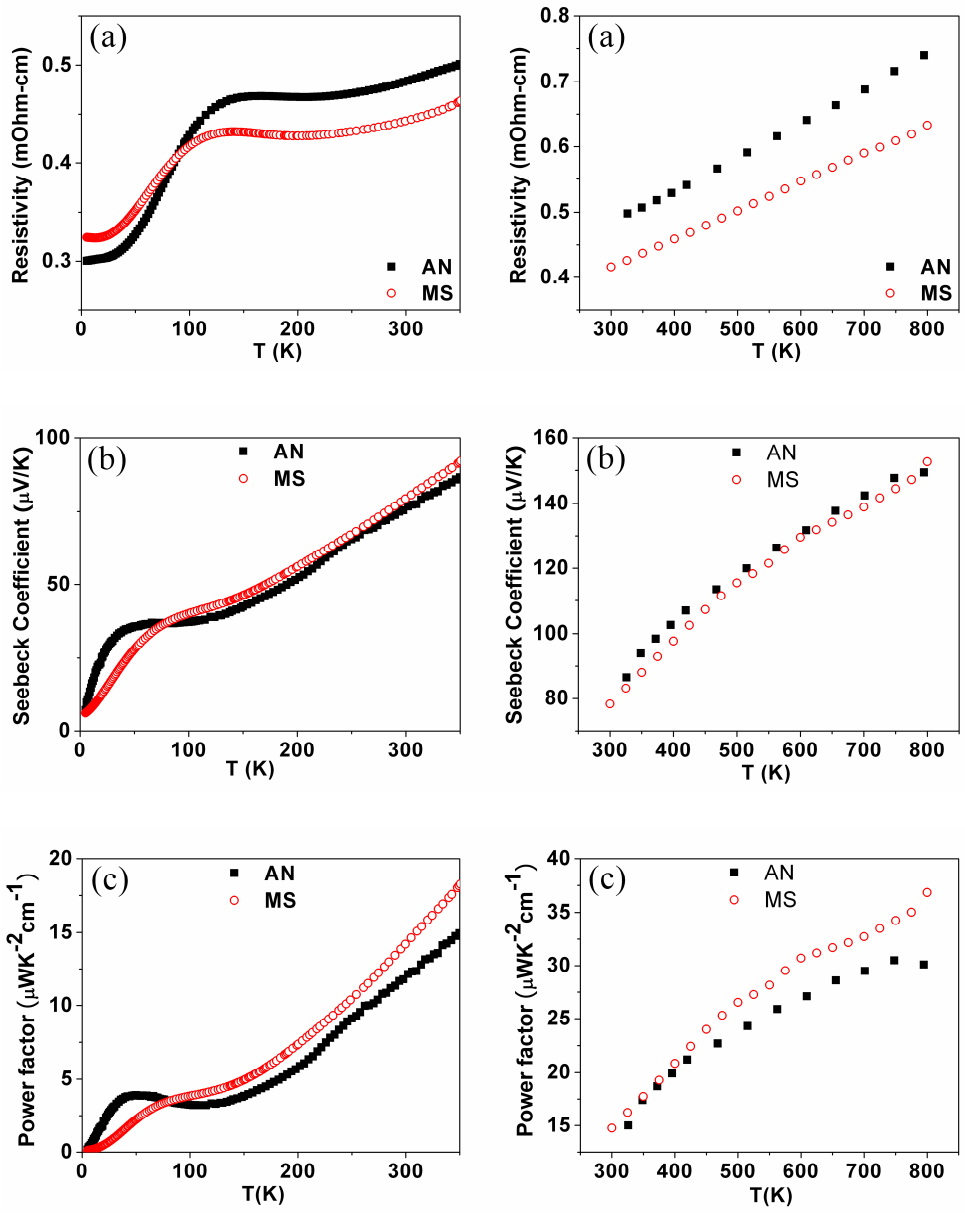

Figure 4.2 The temperature dependence of the electrical resistivity (a), thermopower (b) and power factor ($PF=S^2/\rho$) (c) in samples prepared by non-equilibrium (red circle) and equilibrium (black square) method.

The high temperature data are shown on the right side of Fig. 4.2, which is pretty consistent with the low-T data. From 300 K to 800 K, the resistivity of the MS sample increases with temperature, and is shown to be about 80% of the resistivity of AN sample. This result is quite different from previous reports for

very fine grain material. Usually the much more boundary scattering which introduced by finer grains harms the electrical transport and results in higher resistivity. While our samples exhibit a reversed relationship with a lower ρ above 80K (see Fig. 4.2 a). The Seebeck coefficients of both samples are very close above 300K and reach ~ 150 μV/K at 800K. The power factor of MS sample reaches 36 $\mu WK^{-2}cm^{-1}$, which is a record high value for p-type filled skutterudites.

The temperature dependence of the thermal conductivity, lattice thermal conductivity and *ZT* for the MS and AN samples are shown in Fig. 4.3. Lattice thermal conductivities (κ_L) were obtained by subtracting the electronic contribution (κ_e) from the total thermal conductivity κ. The electronic thermal conductivity was derived by the Wiedemann Franz law: $\kappa_e = LT\sigma$, where L is the Lorenz number (A moderated $L = 2.0 \times 10^{-8}$ $W\Omega K^{-2}$ is used here).

Since the MS sample has smaller grain size and higher interface density (interface area per unit volume), the MS sample has much lower lattice thermal conductivity than the AN sample, especially at low temperature. At 50K, the lattice thermal conductivity of the MS sample is about half of the AN sample's. Above 100K, the thermal conductivities were overestimated by PPMS due to heat loss *via* thermal radiation, and the numbers are related to the size and geometry of the sample. However the difference is still obvious.

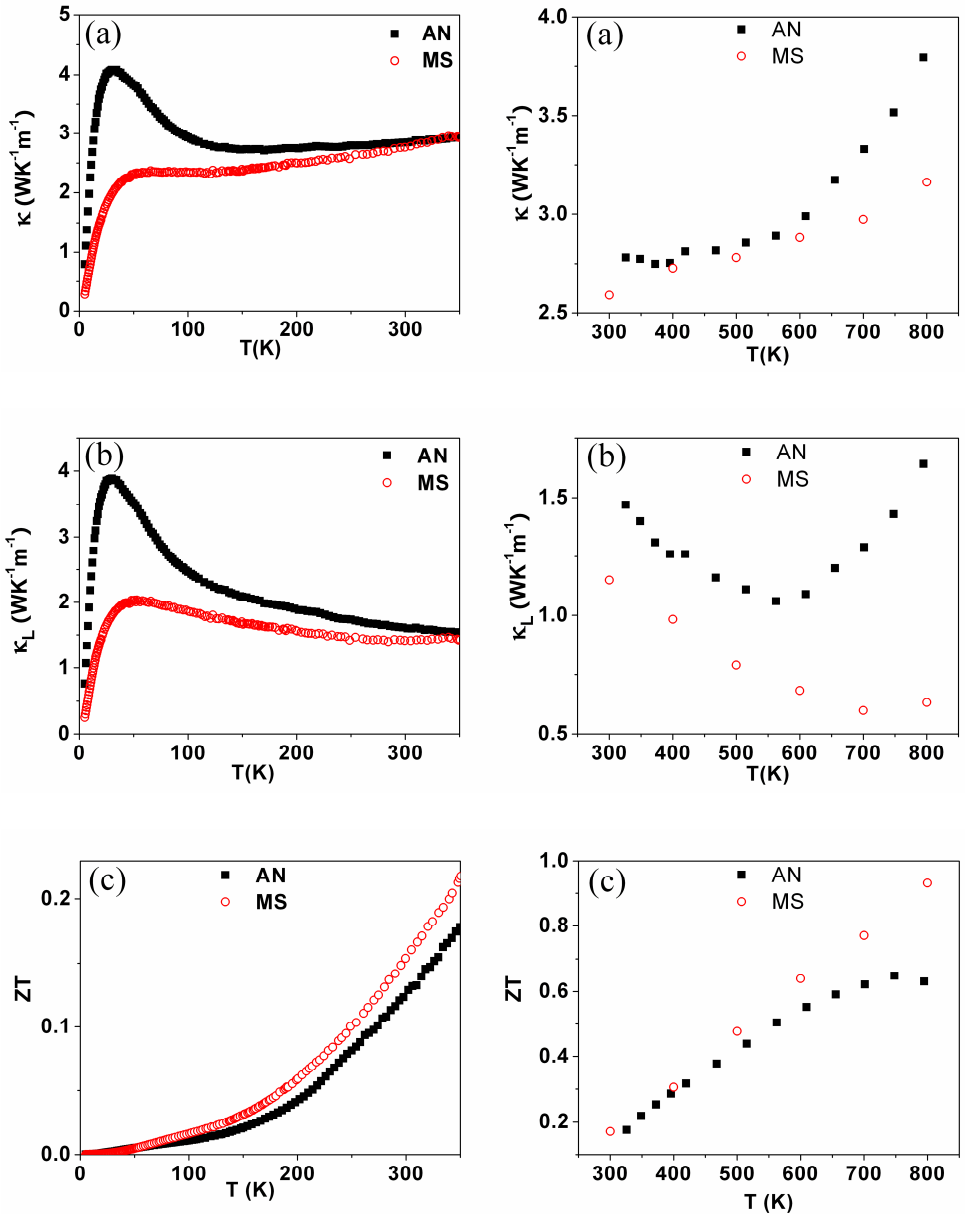

Figure 4.3 Temperature dependence of thermal conductivity κ (a), lattice thermal conductivity κ_L (b) and ZT (c) in samples prepared by non-equilibrium (red circle) and equilibrium (black square) method.

The more accurate thermal conductivity data were obtained at high temperature (above 300K) by using the relationship $\kappa = DC_p d$ and are shown on the right side of Figure 4.3. According to these results, the non-equilibrium synthesis method successfully suppressed the lattice thermal conductivity in this

material for the whole temperature region. The difference of κ_L between MS and AN samples increased above 550K. This phenomenon has not been observed on $Ce_{0.9}Fe_3CoSb_{12}$ samples. Due to the contribution from the electronic part, the total κ of MS and AN samples did not show very big differences between 300 to 550K. The two curves split above 550K due to the huge difference of κ_L (Fig. 4.3 a).

With lower thermal conductivity and higher power factor, the *ZT* of the MS sample is higher than that of the AN sample over the entire temperature region, as shown in Fig. 4.3 (c). The MS sample achieved a *ZT* value of ~0.94 at 800K, which is about 50% higher than the *ZT* of AN sample. The remarkable *ZT* value (close to 1) also makes this material a promising candidate for practical applications.

4.3 Micro-structural Observation by SEM and TEM

To figure out the mechanism behind the lower electrical resistivity in MS samples, SEM and TEM were used to investigate the microstructure of typical MS and AN samples. The results are shown in Fig. 4.4.

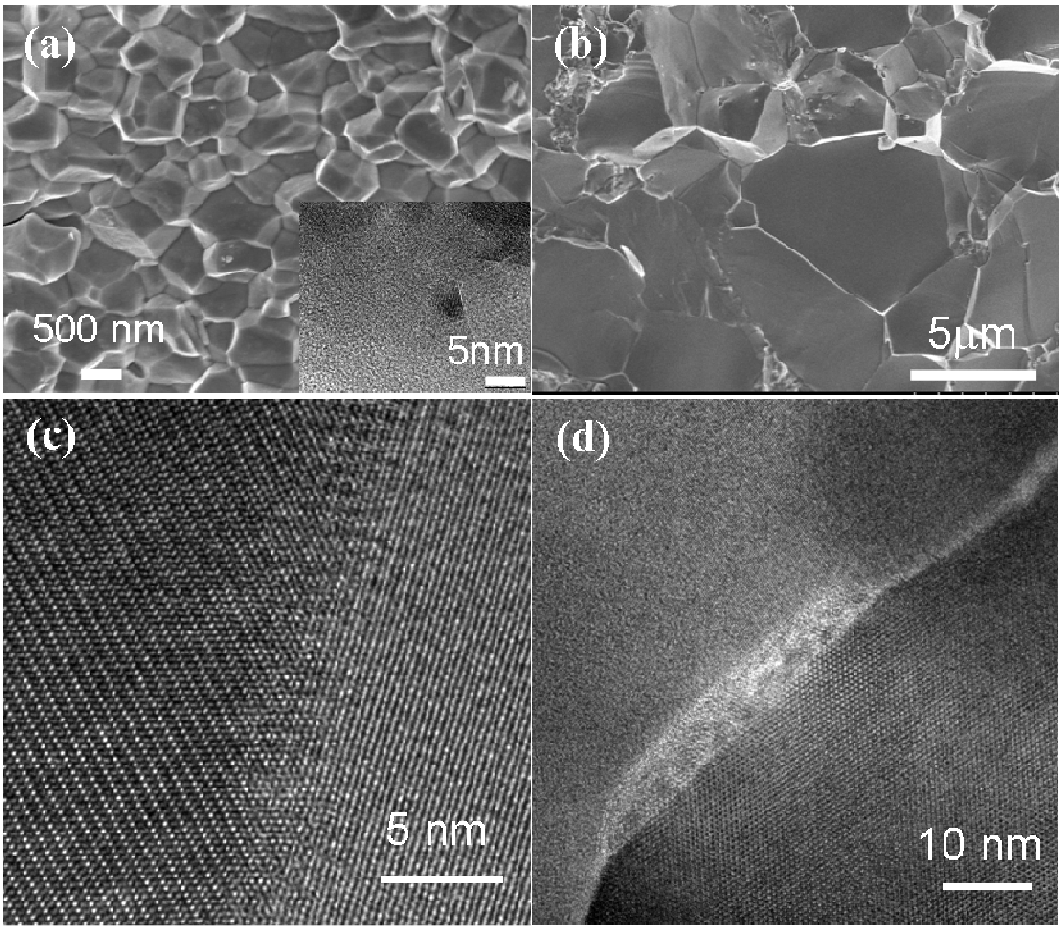

Figure 4.4 SEM images of the fracture surface of (a) non-equilibrium MS and (b) equilibrium AN samples. The inset to (a) is the HRTEM image showing the nanostructure of the melt-spun ribbon prior to SPS. HRTEM images showing typical grain boundaries in the MS samples (c) and the AN samples (d).

Fig. 4.4 (a) shows the fracture surface of the MS sample after SPS, whereas the inset is the HRTEM image showing the structure of the melt-spun ribbon prior to SPS. Nano-sized crystals are found in the amorphous matrix of the melt-spun ribbons, as a result of rapid solidification. In the subsequent 2 minutes of SPS, the amorphous materials were completely converted into crystalline phase and limited grain growth is observed, that results in highly dense MS pellets (above 99% theoretical density) with an average grain size of ~ 300 nm. In

contrast, the grain size of the AN sample (tens of μm), as shown in Fig. 4.4 (b), is more than one order of magnitude bigger than that in the MS sample.

Fig. 4.4 (c) and (d) show the typical results of HRTEM characterization of grain boundaries in both the MS samples and the AN samples. Well-coupled grains with structurally intact grain boundaries are mostly found in the MS samples, while poorly coupled grains with second phase at grain boundaries are mostly found in the AN samples. The width of this second phase region ranges from 1 to 10 nm. By using energy dispersive spectroscopy (EDS), we determined the atomic ratio of the component elements at the grain boundaries and within the grains of the AN samples. These grain boundaries are Ce-rich (as much as 5-10 times higher than the starting composition). For example: the Ce:Fe:Sb ratio in two of the grain boundaries is 58.5 : 1.5 : 40 and 38.9 : 8.1 : 53 respectively, while the compositions within each grain are very close to the stoichiometric ratio. It is apparent that long term annealing necessary for the preparation of AN samples is also causing impurity or filler atoms to segregate at grain boundaries. In contrast, the non-equilibrium process produces much cleaner grain boundaries in the MS samples.

4.4 Impact of Grain Boundaries on Carrier Transport

The temperature dependences of the hole concentration (p, the inset) and hole mobility (μ) in the MS and AN specimens were displayed in Fig 4.5. Both of them have relatively high carrier concentrations (~10^{21}/cm^3), with a temperature dependence similar to a previous observation in this system.[69] Remarkably, at

room temperature, the hole mobility of the MS sample is about twice as high as that of the AN sample, while its carrier concentration stays lower. This indicates that the low resistivity observed in the MS samples at elevated temperatures (> 80K) can be mainly attributed to its high mobility.

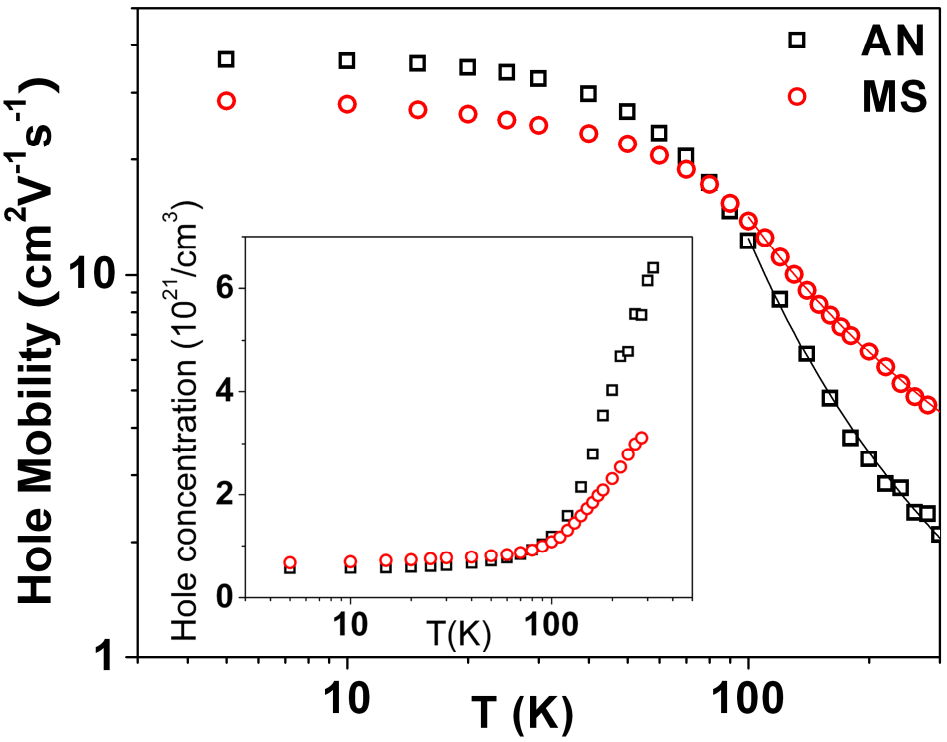

Figure 4.5 The temperature dependence of hole mobility and hole concentration (the inset) in p-type $Ce_{1.05}Fe_4Sb_{12.04}$ filled skutterudites prepared by non-equilibrium (red circle) and equilibrium (black square) method. The hole mobilities of two samples were calculated using equation $\sigma = pe\mu$, where e is the electric charge of the carrier. The lines are corresponding fitting curves (see text).

The temperature dependence of carrier mobility below 80K is very small, which suggests the predominant scattering mechanism at low temperatures is neutral impurity scattering. Similar behavior has been reported for several antimonide materials [5, 60]. Usually, acoustic phonon scattering dominates at higher temperatures, and results in a quick decrease of carrier mobility with

increasing temperature, which follows a $T^{3/2}$ behavior. However, the high temperature parts of the mobility curves in Fig 4.5 could not be fit by using this equation. This indicates that there are some other scattering mechanisms dominating the carrier transport behavior in our samples.

Actually, the temperature dependence of the carrier mobility we observed above 80 K follow the relation $\mu \propto T^{-\frac{1}{2}} \exp(-\frac{E_b}{k_B T})$ very well, where E_b is the boundary potential barrier height,[70] and k_B is Boltzmann's constant. The solid lines shown in Fig.4.5 are the corresponding fitting curves with fitting parameters E_b ~ 187K (~ 16 meV) for the AN samples and E_b ~ 90K (~ 7.8 meV) for the MS samples. The derived energy barriers are qualitatively consistent with the results of structural characterization. This is because the thicker and dirty grain boundary in the AN samples is capable to trap more carriers and build up a higher potential barrier. The overall temperature dependence of the mobility behavior is explained as follows: At low temperatures (<80K), the kinetic energy of the electrons is much lower than the energy barrier height, so that the number of barriers dominates the transport behavior. Higher density of grain boundaries (more scattering events) lead to lower mobility and hence higher resistivity in the nano-structured MS samples. As temperature increases, the phonon scattering becomes important and leads to the quick decrease of carrier mobility in both samples. On the other hand, the kinetic energies of electrons increase and get close to the barrier height (E_b ~ 90K) at T >80 K in the MS sample, giving rise to the higher

hole mobility and lower resistivity observed in the MS sample. The 80 K is more or less a crossover temperature.

4.5 Summary

We have shown that non-equilibrium synthesis is a fast and effective method for preparing high performance thermoelectric filled skutterudites. The thermoelectric figure of merit (*ZT*) in filled skutterudite $CeFe_4Sb_{12}$ has been enhanced by ~ 50% at 800K using this technique. This rapid conversion process produces nano-sized grains with cleaner grain boundaries. By comparison, the conventional long term annealing method produces large grains with dirty grain boundaries, where the filler atoms and second phases segregate. Combined structural and transport measurements provide clear evidence that the grain boundaries play a major role in the electron scattering in these materials. The temperature dependence of the carrier conduction behavior is explained in terms of the crossover from the dominance of the energy barrier density at low temperature to the energy height at elevated temperature.

5 Fure Perspectives

This study firmly demonstrated that this non-equilibrium synthesis route is very effective in producing high performance thermoelectric materials by reducing their thermal conductivities while maintaining or even enhancing the power factor. It is especially useful for thermoelectric materials when the effect of doping reaches its limit. The only requirement is that the materials should have relatively low electrical resistance in order to be able to be heated by the radio frequency heating power.

This technique is expected to be applicable to other thermoelectric materials. Two examples are given here:

5.1 Double Filled p-type Antimonide Skutterudites

The *ZT* value of n-type filled antimonide skutterudites has been raised to higher than 1.4 by multiple filling.[9-10] It is an urgent task now to produce p-type filled antimonide skutterudites with similar *ZT* value to match the n-type leg in the thermoelectric power generation module. However, the *ZT* of the p-type filled skutterudite has not gotten satisfactory improvement since 1997. The non-equilibrium synthesized single filled skutterudites we prepared in this work have a *ZT* value less than 0.8. Tang *et al.*[71] observed the highest *ZT* value of ~1.2 on a

double filled p-type filled skutterudite $Ca_{0.18}Ce_{0.12}Fe_{1.45}Co_{2.55}Sb_{12}$. If we apply our non-equilibrium synthesis method to this double filled skutterudite, we expect to produce p-type double filled skutterudite with a *ZT* value of around 1.4.

5.2 Half-Heusler Compounds

Another possible application of our non-equilibrium synthesis method is on Half-Heusler (HH) inter-metallic alloys. These alloys have recently received increasing attention as potential TE materials for high temperature applications. HH phases have the MgAgAs (space group $F\bar{4}3m$)[72] or "half-stuffed GaAs" crystal structure, consisting of three interpenetrating fcc sublattices. Their chemical formula is XYZ, where X, Y, and Z can be selected from many different elemental groups.[73] Figure 5.1 shows the unit cell of TiNiSn, in which Ti and Sn occupy a NaCl lattice and Ni occupies an fcc sublattice.

The half-Heulser alloys are attractive as high-temperature TE materials, because they can be relatively easily synthesized as 100% dense samples. In particular, the refractory-based HH alloys exhibit high melting points of 1100–1300°C as well as chemical stability and essentially zero sublimation at temperatures near 1000°C. Many of the refractory metal[74-77] and lanthanide metal[78] thermoelectric HH alloys exhibit large room-temperature Seebeck coefficients of ~100 μV/K and moderate electrical resistivities of ~1–10 μΩm. Sb-doped TiNiSn alloys exhibit power factors as high as 4.6 $Wm^{-1}K^{-1}$ at 650 K (380°C).[79] However the high thermal conductivity (κ>10 $Wm^{-1}K^{-1}$) prevents it from being a good thermoelectric material.

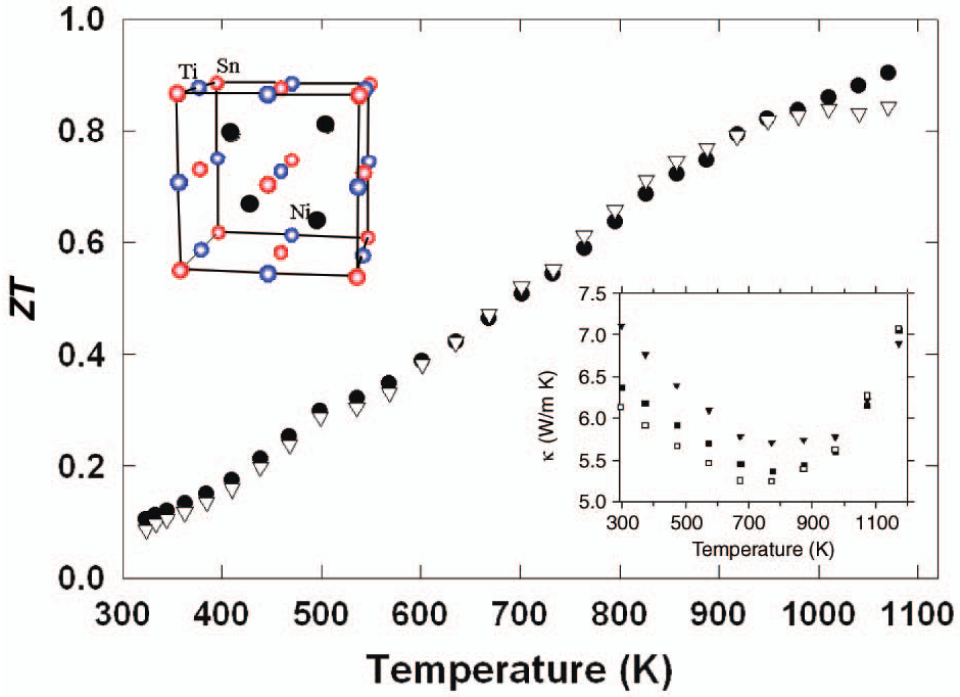

Figure 5.1 Figure of merit *ZT* versus T for $Hf_{0.75}Zr_{0.25}NiSn_{0.975}Sb_{0.025}$ obtained from measured (▽) and extrapolated (●) thermal conductivities. The upper left inset shows the unit cell of TiNiSn half-Heusler phase. The lower right inset shows thermal conductivities obtained from laser-flash thermal diffusivity and specific heat, with data points starting at 300 K:$Hf_{0.75}Zr_{0.25}NiSn_{0.975}Sb_{0.025}$(▼), $Hf_{0.6}Zr_{0.25}Ti_{0.15}NiSn_{0.975}Sb_{0.025}$ (■), and $Hf_{0.75}Zr_{0.25}Ni_{0.9}Pd_{0.1}Sn_{0.975}Sb_{0.025}$(□)[74].

The effectiveness of isoelectronic alloying in achieving improved TE properties has been demonstrated in several HH alloys. In 2001 Shen *et al.* reported a maximum *ZT* of 0.7 at 800 K in n-type Sb-doped ZrNiSn alloys partially substituted with the heavier Pd atoms in the Ni sublattice.[77] Qiu *et al.* also reported a maximum dimensionless figure of merit of 0.70 at 900 K for n-type $Ti_{0.6}Hf_{0.4}Co_{0.87}Ni_{0.13}Sb$ in 2009.[76] A *ZT* value close to 0.5 has been reported by Culp *et al* for p-type $Zr_{0.50}Hf_{0.50}CoSb_{0.8}Sn_{0.2}$material.[75] Up to now, the highest *ZT* value for n-type HH alloys is about 0.8 for $Hf_{0.75}Zr_{0.25}NiSn_{0.975}Sb_{0.025}$ at 900K (Fig. 5.1).[74] The thermal conductivities of these materials are still high (> 5 $Wm^{-1}K^{-1}$). So we should be able to improve the

ZT if we can reduce their κ without deteriorating the power factor too much by introducing more boundary scattering into the material. Sharp *et al*[49] estimated the relative magnitudes of boundary scattering effects on phonons and charge carriers, and predicted that reducing grain size could greatly enhance the *ZT* values of half-Heusler alloys. It could be a promising application for the non-equilibrium synthesis method to reduce the thermal conductivity, and hence improve the *ZT* of HH alloys.

Part II

The Enhancement of Thermoelectric Power Factor in $FeSb_2$ single crystal and $Ca_3Co_4O_9$

6 Giant Thermoelectric Power Factor Induced by Metal-Insulator Transition in $FeSb_2$ Single Crystal

6.1 Introduction

Solid-state thermoelectric (TE) cooling and electrical power generation devices have many attractive features compared to other methods, such as long life, no moving parts, no emissions of toxic gases, low maintenance, and high reliability. However, their use has been limited by the relatively low energy conversion efficiency of present thermoelectric materials. There are two distinct approaches used to increase the figure of merit: thermal conductivity reduction and power factor enhancement. Thermal conductivity reduction techniques, such as alloy scattering[80], "phonon glass electron crystal"[2, 81], and very recently the introduction of nanostructure to reduce the phonon mean free path, have been successfully used to produce high *ZT*[16, 82]. In the first part of this thesis, I have introduced one example of these techniques.

However, there is a limit to increase the figure of merit by reducing the thermal conductivity alone. In principle thermal conductivities of all crystalline solids have a lower limit because the phonon mean free path cannot be reduced

below the interatomic spacing.[83] Even if the lattice part contribution to the total thermal conductivity were zero, the electronic contribution can still play a significant role. A simple estimation shows that $ZT \sim S^2/L_o$, when κ_L is negligibly small and the Wiedemann-Franz law ($\kappa_e \sim L_o \sigma T$) is used as a crude approximation. The traditional way to enhance power factor is by varying the doping concentration, which alters the carrier density. Usually, higher electric conductivity comes with higher carrier concentration, while higher carrier concentration typically comes with the penalty of lower thermopower.[39] It is difficult to enhance thermopower and electric conductivity at the same time by doping, because these two variables are coupled. The improvement by this method is very limiting in practice. So searching for new material systems with higher power factor is always highly desirable, but also very challenging.

In a very general theoretical analysis, G. Mahan and J. Sofo showed that the best electronic structure for thermoelectric materials is a delta function in the transport distribution centered about 2-3 k_BT from the Fermi energy.[84] Kondo insulators may represent a closer approximation of the ideal electronic structure suggested by Mahan and Sofo. Localized d or f states hybridize with conduction electron states leading to the formation of a small hybridization gap in Kondo insulators and strongly correlated electron systems. The density of states (g) just below and above the hybridization gap becomes very large. The thermopower is sensitive to variations in g in the vicinity of the Fermi level, and very large absolute values of S can be expected in Kondo insulators and strongly correlated electron systems. Large S has been reported in a number of compounds, e.g.,

FeSi[85], $Ce_3Pt_3Sb_4$ [86-87], $CeFe_4P_{12}$ [88], $CeRu_4Sb_{12}$ [89], and CeB_6 [90], which all have pronounced peaks in *S(T)* at low temperatures, where $|S|>100$ μV/K. $FeSb_2$ is another well-studied compound[91] and has been characterized as a strongly correlated Kondo insulator based on measurements of the electrical resistivity, magnetic susceptibility, thermal expansion, heat capacity and optical conductivity[92-94]. We performed an exploratory investigation into the thermoelectric property of this class of materials, and discovered that giant (record high) thermoelectric power factor can be realized through a metal-insulator transition. This finding opens up a new direction for thermoelectric material research, although there are many questions which remain to be answered at this early stage.

$FeSb_2$ crystallizes in *Pnnm* orthorhombic structure, as shown in Fig. 6.1. The basic structural unit is made of Fe ions surrounded by deformed Sb octahedra. The Sb octahedra form edge sharing chains along the *c*-axis, sharing corners between chains. A. Bentien *et al.* grew $FeSb_2$ single crystals from modified Sb flux by decanting crystals at 690°C, after cooling down to 640°C.[95] A colossal thermopower of ~-45000 μV/K was observed at 10K, which is two orders of magnitude higher than other strongly correlated electron systems. Furthermore, the thermoelectric power factor reaches its high record value of ~ 2300 $\mu WK^{-2}cm^{-1}$ at 12K. However, these crystals exhibit small resistivity anisotropy and have semiconductor behavior and relatively high resistivity along three principle crystalline axes. Our earlier investigation on large single crystals of $FeSb_2$ showed huge resistivity anisotropy in $FeSb_2$ single crystals. In these single crystals,

electric transport along the *a*-axis and the *b*-axis shows semiconductor behavior throughout the entire temperature regime, while the c-axis is metallic at high temperatures and exhibits metal to insulator transition (MIT) at 40K[92]. Introducing low resistivity by MIT in a system with exceptional high thermopower can produce an even higher thermoelectric power factor.

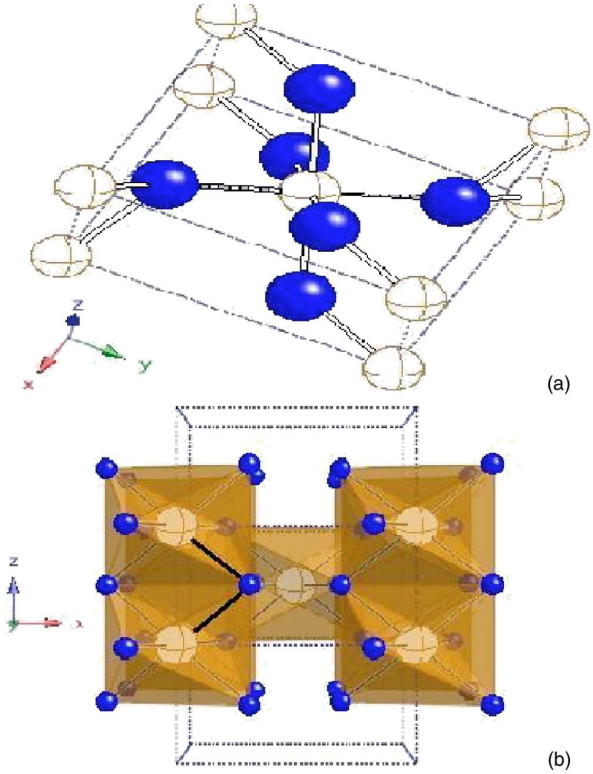

Figure 6.1 Crystal structure of $FeSb_2$ [92] showing Fe (open, brown crosses) surrounded by Sb (full blue) octahedral.

In this work, single crystals of $FeSb_2$ with and without MIT have been successfully prepared by the original flux method in ref.[92] and by the modified method in ref.[95] respectively. Thermoelectric properties along different axes are determined and compared. Electrical resistivity (ρ), *S* and their anisotropy along *b* and *c*-axes were measured in both zero and 9 T magnetic field. Single crystal X-ray diffraction was employed to evaluate crystal disorder. Our results show that

$FeSb_2$ single crystals with MIT have much higher power factor than those without MIT due to the low resistivity introduced by MIT.

6.2 Single Crystal Growth

Single crystals of $FeSb_2$ were grown by the flux method by Rongwei Hu in Brookhaven National Laboratory. Two batches of crystals were grown by slightly different procedures. The first batch was grown by the traditional method we used here at Brookhaven National Laboratory. The second batch was grown by the modified method used by A. Bentien *et al.* The detailed procedure is shown in Figure 6.2 and 6.3.

6.3 Thermoelectric Properties Measurement

The crystals were oriented using a Laue camera and were polished into rectangular bars along specific crystalline axes. *S(T)* and $\rho(T)$ along different axes were measured on a Physical Properties Measurement System (PPMS) from Quantum Design. *S(T)* were determined by thermal transport measurements. The typical sample geometry is about $4.5\times0.6\times0.5$ mm^3. In these measurements, crystals were made into two-probe samples with two ends soldered on disk-shaped leads using Indium. $\rho(T)$ was determined with a standard four-point DC method.

The thermal transport measurement is very challenging here. Because the crystal is very brittle, the samples made by the traditional way are very easy to break during mounting. A special sample holder was made for the measurement.

This sample holder has two disk-shaped leads. A G10 bar with the same length as the sample was attached between the leads to stabilize the holder. The crystal was then soldered between the leads using indium.

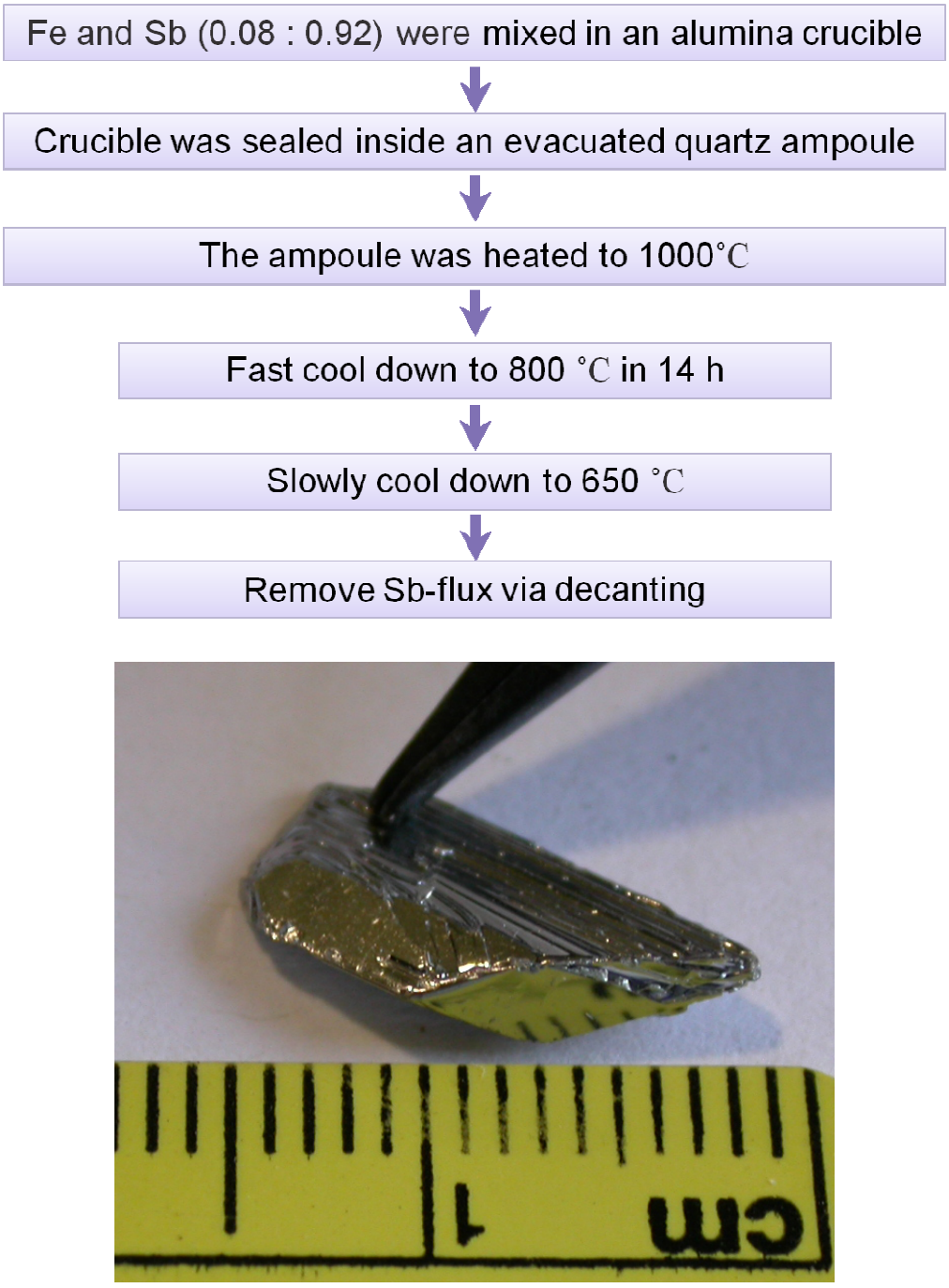

Figure 6.2 The traditional Flux method for $FeSb_2$ single crystal preparation and the single crystal grown by this method.

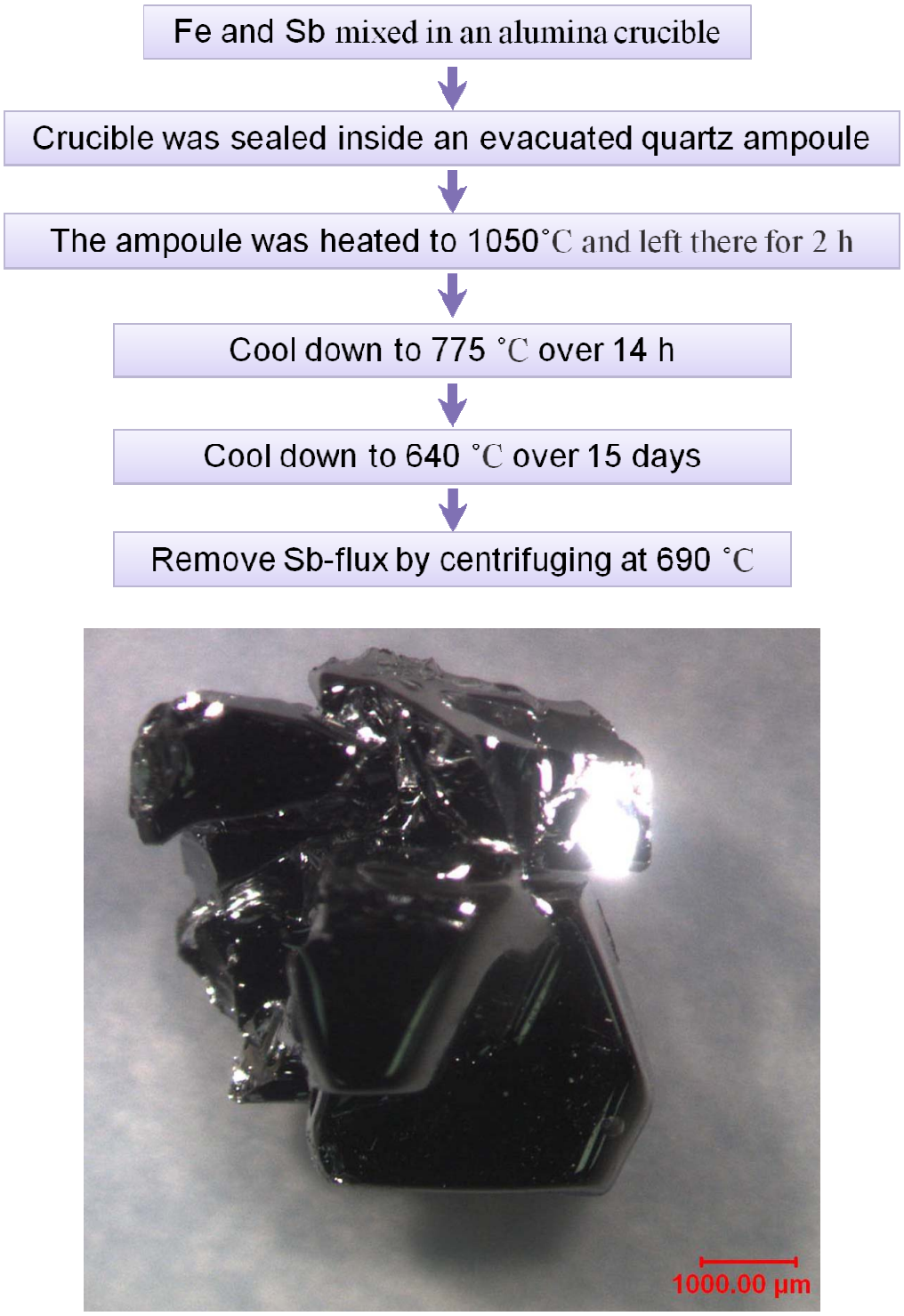

Figure 6.3 The modified Flux method for $FeSb_2$ single crystal preparation and the single crystal grown by this method

6.4 Results and Discussion

The single crystals prepared by the original flux method show semiconductor behavior along the *a* and *b* – axes and MIT along the *c*–axis.[92] Figure 6.4 (a) shows the resistivity along the high conductivity *c*-axis of the single crystal prepared by the original flux method as a function of temperature in zero magnetic field and in a field of 9T. The temperature dependence of the resistivity shows the onset of metal-insulator transition at about 40K. And the resistivity reaches its minimum of $7x10^{-7}$ Ω·m at about 34K. This sample also has a very high magneto-resistance in the field which is perpendicular to the *c*-axis.

The resistivity of the crystal prepared using the modified method does not show metallic behavior along any principle axis. This is similar to the results reported by Bentien, *et al* [95]. Magnetic field was applied along 3 principal crystalline axes. For both current // b – axis and c – axis the longitudinal magneto-resistance is positive and very small. Figure 6.4 (b) shows ρ(T) for $FeSb_2$ single crystals grown by modified method along *c*-axis. In zero field, the resistivity of this sample is about three order of magnitude higher than the crystal with MIT, in the temperature region between 10 K to 50K. Magnetic field along *b*-axis results in the highest *c*-axis MR.

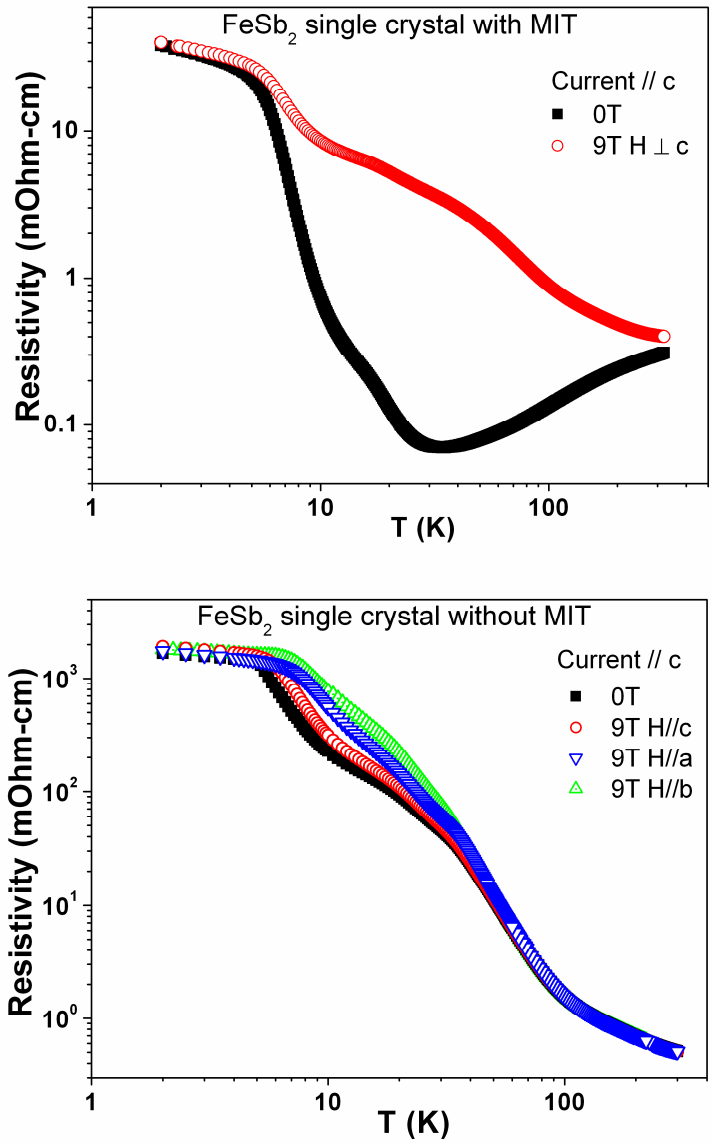

Figure 6.4 The temperature dependence of the resistivity of $FeSb_2$ single crystals along the highly conductive *c*-axis

Figure 6.5(a) shows *c*-axis Seebeck Coefficient of $FeSb_2$ single crystals with MIT in magnetic fields of 0T and 9T. Thermopower shows relatively weak temperature dependence above the metal-insulator transition temperature. The absolute value of the Seebeck coefficient rises rapidly below 40K and reaches its maximum value of -1000V/K at about 10K. The Seebeck Coefficient was obviously suppressed in magnetic fields at temperatures from 5K to 20K.

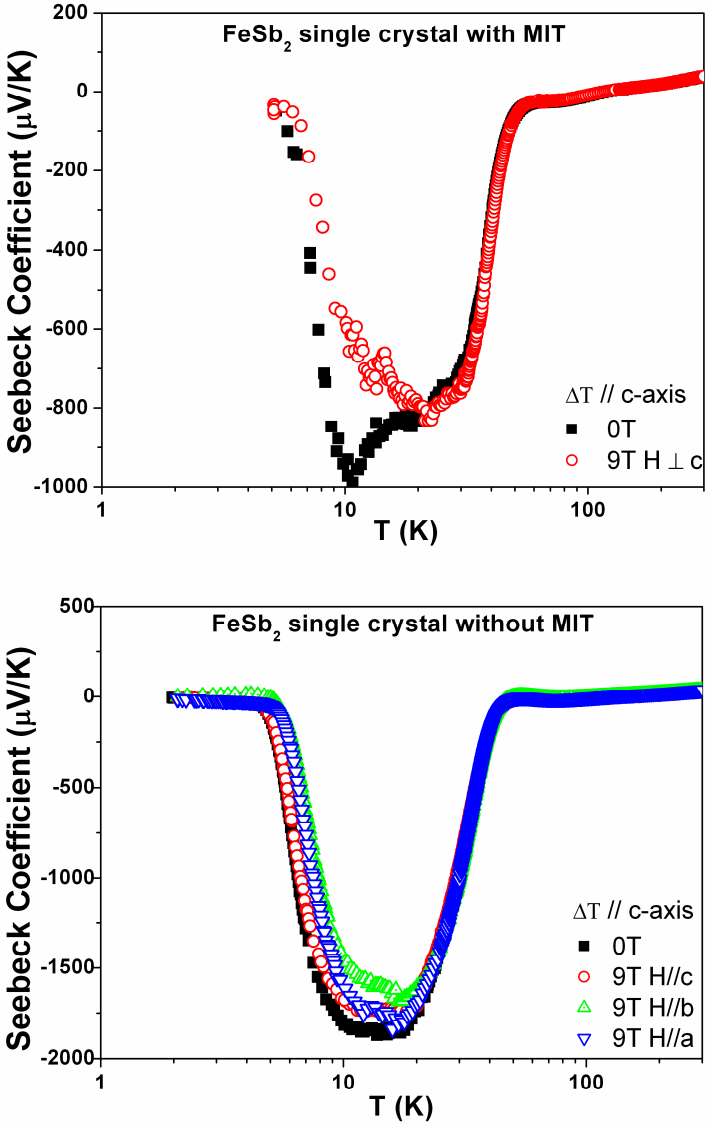

Figure 6.5 The temperature dependence of the Seebeck coefficient of $FeSb_2$ single crystals along *c*-axis

The *c*-axis Seebeck Coefficient of $FeSb_2$ single crystals without MIT is shown in Figure 6.5 (b). *S(T)* reaches ~ -1900V/K at about 10K, then diminishes in magnitude to nearly 0V/K at 55K but remains negative up to 110K. This is different from Ref.[95]. Above 110K, *S(T)* increases almost linearly to at least

300 K, where *S* = 40V/K. The absolute value *S(T)* is a little bit lower in magnetic field along c-axis. When we apply field along b- and a-axes, *S(T)* was obviously depressed between 5K and 10K. Another interesting phenomenon is that, when we apply magnetic field along b axis, *S(T)* is positive at two temperature regions: between 2K and 5K where *S (T)* has maximum of 14.2V/K at 4.2K and between 50 K and 60 K where *S (T)* nearly reaches 4.7V/K at about 53.2K. When magnetic field is applied along a- and c-axis, *S (T)* remains negative below 110K.

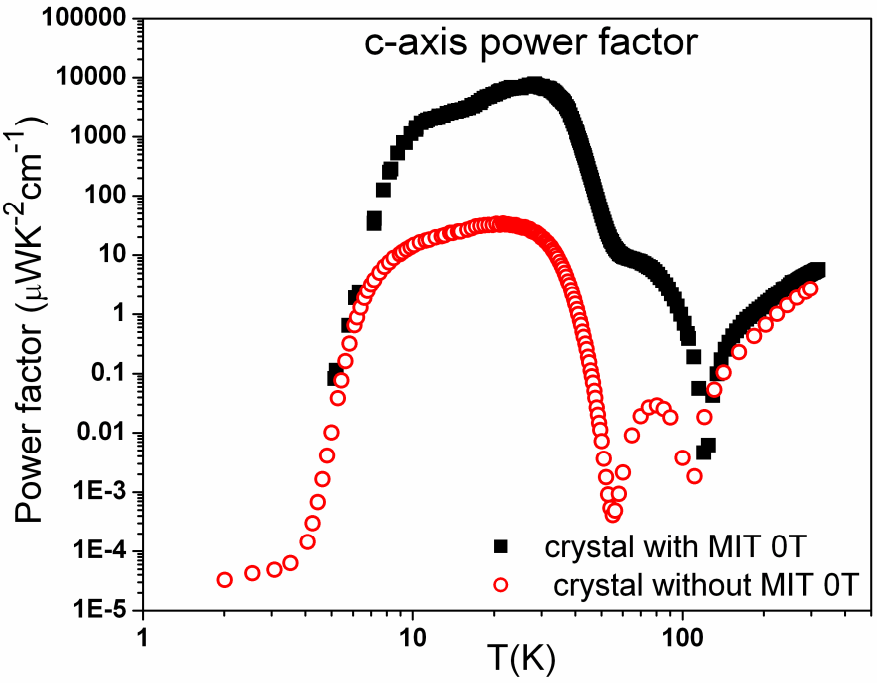

Figure 6.6 The temperature dependence of thermoelectric power factor of $FeSb_2$ single crystals along *c*-axis

Figure 6.6 depicts the thermoelectric power factors of the two types of $FeSb_2$ single crystal. Comparing to the crystals without MIT, the crystal with MIT has lower thermopower. However, it has much higher power factor between 8 K and 100K due to its low resistivity. The thermoelectric power factor of traditional grown single crystal reaches its maximum of ~ 7800 $\mu WK^{-2}cm^{-1}$ at about 28 K.

This is more than two orders of magnitude higher than the crystal without MIT (grown using modified method).

It is worth noticing that the power factor peak for crystals with MIT locates at 28K, which is higher than that for crystals without MIT (our observation is at 20K; the power factor peak observed by A. Bentien *et al*. is even lower, at 12K).

In thermoelectric research, varying doping level is a traditional way to improve thermoelectric properties in a specific system. However, its effect is usually limited, because the increase of electric conductivity by raising carrier concentration will broaden the transport distribution, which deteriorates thermopower. The transport properties of transition metal antimonides are very sensitive to the synthesis procedure and doping level. In this work, the slightly different Sb flux decanting procedure might have resulted in a small change on the Fe and Sb ratio in the crystal, and hence introduced a little bit disorder in the structure. In the crystal which shows anisotropic behavior, thermopower has been kept at a relatively high level, while the electric conductivity is dramatically enhanced by MIT. This produced a record high power factor, ~ 7800 $\mu WK^{-2}cm^{-1}$, in $FeSb_2$ single crystal. This exceeds the largest value reported for the strongly correlated metal $YbAgCu_4$ (235 $\mu WK^{-2}cm^{-1}$), by more than one order of magnitude and is about 200 times larger than the PF of the state-of-art thermoelectric Bi_2Te_3-based material (40 $\mu WK^{-2}cm^{-1}$).[42]

6.5 Some Unsolved and Important Issues

Both theoretical and experimental studies are being carried out by our collaborators, in order to understand the origin of the high power factors observed in this material. These studies may provide new and much more effective route to enhance thermoelectric power factor. Although some progress has been made, many important issues are still not solved. Two key issues are listed here that are either currently being studied or for future investigation on the structure and chemical compositional difference in the samples with MIT and without MIT.

1) We have performed extensive X-ray diffraction studies of both crystals based on the synchrotron light source, and found little difference. Perhaps more sophisticated techniques are needed, such as nuclear magnetic resonance (NMR),[96-97] and the atomic pair distribution function (PDF) analysis.[98-100]

2) Spin contribution: Some theoretical studies have been performed and show the system is in a weak ferromagnetic ground state that can produce high Seebeck coefficient.[101] However, magnetization measurement shows little magnetic moment in both single crystals, which disagrees with the theoretical prediction. This discrepancy needs to be solved.

7 Thermoelectric Misfit Layered Cobaltite $Ca_3Co_4O_9$: High Temperature Properties and *in-situ* X-ray Investigation

7.1 Introduction

In 1997, it was discovered that large thermoelectric power (~100μV/K at room temperature) and low resistivity could coexist in $Na_{0.5}CoO_2$,[102] which made this compound an attractive candidate for thermoelectric (TE) applications. Soon the related cobaltites, which possess similar properties, have been synthesized and investigated.

Layered cobaltites feature alternatively stacked conducting CoO_2 blocks and insulating blocks with incoherent layer boundaries, producing highly anisotropic properties along their crystallographic directions. Unlike cuprates with Cu ions defining square lattice, cobaltite have mixed valent Co ions define a layered triangular lattice. The CoO_2 layer consists of edge-sharing CoO_6 octahedra, with a significant rhombohedral distortion. Na_xCoO_2 has relatively simple structure because of the smaller size of the Na atoms. $Ca_3Co_4O_9$ has misfit-layered structure consisting of a single [CoO_2] layer of CdI_2-type stacked with [Ca_2CoO_3] rock salt type layers, with a different in-plane lattice parameter *b* [103-

104]. The charge-carrier transport in those misfit cobaltates is thought to be restricted mainly to these CoO_2 planes, and they seem to be crucial in the high thermoelectric power properties.

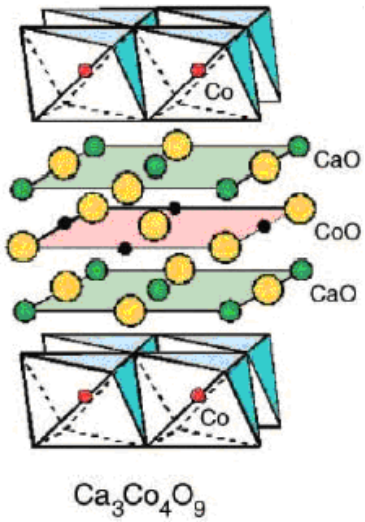

Figure 7.1 Schematic illustration of the crystal structure of $Ca_3Co_4O_9$

$Ca_3Co_4O_9$ (also written as $[Ca_2CoO_3]_{0.62}[CoO_2]$), is regarded as a very promising material to be used at high temperature, because it is nontoxic and has good thermal and chemical stability at high temperature in air. Many efforts have been made to make $Ca_3Co_4O_9$ into an applicable module. And pretty good results have been achieved in both $Ca_3Co_4O_9/LaNiO_3$ and $Ca_3Co_4O_9/CaMnO_3$ systems [105-106]. Several methods, including porous thermoelectric oxides, have been used to improve the efficiency of modules.[107] However, there are still two major challenges in constructing thermoelectric oxides modules. One is the metal to ceramic contact preparation, the other one is the performance deterioration. The investigations on high temperature structure and thermoelectric properties can provide insights that may help us to address these two challenges.

The thermoelectric devices using $Ca_3Co_4O_9$ is primarily aiming at the application above 800 K. However, few detailed investigation of its thermoelectric properties in this high temperature region has been made. We carried out a coordinated investigation of high temperature structure transition and thermoelectric properties on $Ca_3Co_4O_9$ single crystals and polycrystals, in order to understand the correlation between their structure and properties.

7.2 Experiments

7.2.1 Sample Preparation

Single crystals were prepared using a similar flux method as described in elsewhere.[108] The reactant ($CaCO_3$, Co_3O_4) and flux ($SrCl_2$) were carefully weighed. The grown crystals were washed with distilled water in order to remove the $SrCl_2$ flux, and then annealed at 450°C in an oxygen gas flow for 12 h. A Philips 3100E X-ray generator was used to check the quality of the crystals. X-ray powder diffraction was collected on the growth surface of the single crystal by step scanning of 2θ from 10º to 80º.

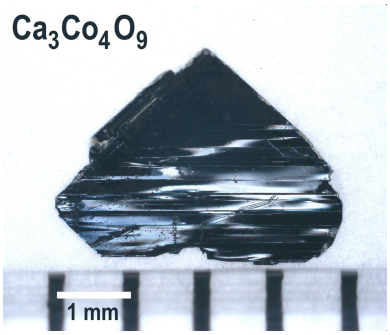

Figure 7.2 Photograph of the as grown $Ca_3Co_4O_9$ single crystal prepared by the flux method

Polycrystalline $Ca_3Co_4O_9$ samples were prepared via standard solid state reaction. A stoichiometric mixture of $CaCO_3$ and Co_3O_4 was first heated to 680 ºC and kept at this temperature for 1 hour. Then the temperature was raised to 880 ºC and kept for 22 h. The sintered powder was taken out and ground thoroughly, and then heated at 900 ºC for 24 h. This process was repeated twice. Then the powders were pressed into ϕ 1" pellets, and sintered at 920 ºC in flowing O_2 environment.

7.2.2 Home-made High-T TE Properties Measurement System

High temperature thermoelectric properties were measured using a home-made systems. A horizontal tube furnace is used to control the environmental temperature.

The Seebeck coefficient was measured as follows: one end of the sample was fixed on the probe, while the other end was extended into the tube furnace. The probe temperature is controlled by separate flowing gas through a thin-wall stainless steel tube bonded to the sample holder. By this means, a temperature gradient of ~ 5K can be easily created across the sample. Fig. 7.3 c shows the schematic diagram of this measurement. Two type K thermocouples (0.005" in diameter) were attached at each end of the sample in order to measure thermoelectric power of the sample. The thermocouples are used to measure the temperature of the sample as well as the voltage bias. A two-channel thermometer (Fluke 54II) was used to read temperatures. Two Keithley 182 digital Voltmeters were used to read voltage V_{AA} (the voltage across the alumel legs) and V_{CC} (the voltage across the chromel legs).

The absolute Seebeck coefficient values are calculated by similar methods previously used by A.K. Singh[109] and R.T. Littleton[110]. The thermoelectric power of the sample, S_S, is related to the measured sample voltages V_{AA} and V_{CC} by:

$$V_{AA} = (S_S - S_A) \bullet \Delta T \quad \text{and} \quad V_{CC} = (S_S - S_C) \bullet \Delta T \qquad \textbf{(}7.1\textbf{)}$$

where S_A and S_C are the absolute thermoelectric power of each of the thermocouple legs (alumel and chromel respectively), and ΔT is the temperature difference between the two thermocouple junctions. Eliminating ΔT in expression (4), the sample's thermoelectric power is given by:

$$S_S = \frac{V_{AA} S_C - V_{CC} S_A}{V_{AA} - V_{CC}} \qquad \textbf{(}7.2\textbf{)}$$

For the resistivity measurement, the whole sample was attached on the probe. Four gold wires (0.002" in diameter) were attached on the crystal separately to make it a four-probe configuration. The temperature of the sample was measured by using a type K thermocouple. This thermocouple was attached to the back of a substrate which was used to support the sample. LakeShore Cryotronics 120 current source was used to supply sample current +I and –I. A Keithley 182 digital Voltmeter was used to measure the voltages V+ and V-. The voltage differences due to reversed currents were used to factor out any induced thermal electromotive forces to determine the sample resistance:

$$R = \frac{V_+ - V_-}{2|I|} \qquad (7.3)$$

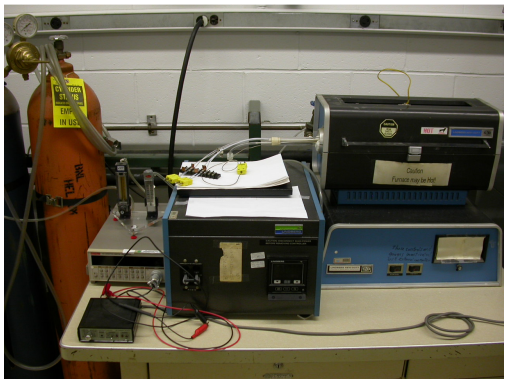

(a)

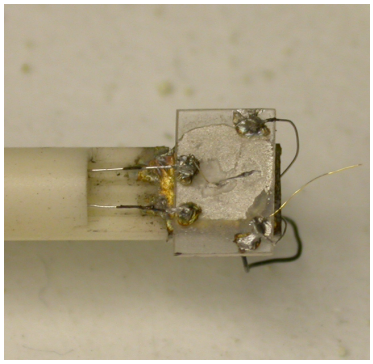

(b)

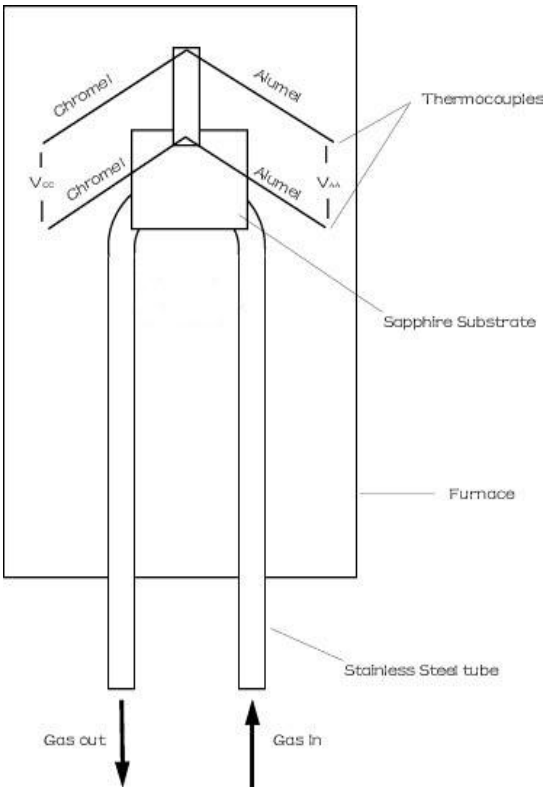

(c)

Figure 7.3 The home-made high temperature thermoelectric properties measurement system: (a) the whole system, (b) the probe for resistivity measurement, (c) the schematic diagram of the thermopower measurement

7.2.3 High temperature *in-situ* X-ray powder diffraction experiment

High temperature *in-situ* X-ray powder diffraction experiment up to 1000K was performed at the National Synchrotron Light Source Brookhaven National Lab by Haiyan Chen. CCO poly-crystal powder sample was loaded into a quartz tube, then heated to 900K using a rate of 0.67 °C/min with air flow (rate = 10 mL/min). Every data point was acquired in 2 minutes. The wavelength of the X-ray used in this experiment was 0.72343Å.

7.3 Results and Discussion

7.3.1 Single crystal quality investigation by X-ray diffraction

Figure 7.4 shows the X-ray diffraction pattern of an as grown CCO single crystal. The result shows that the growth surface of the platelets was the a-b plane.

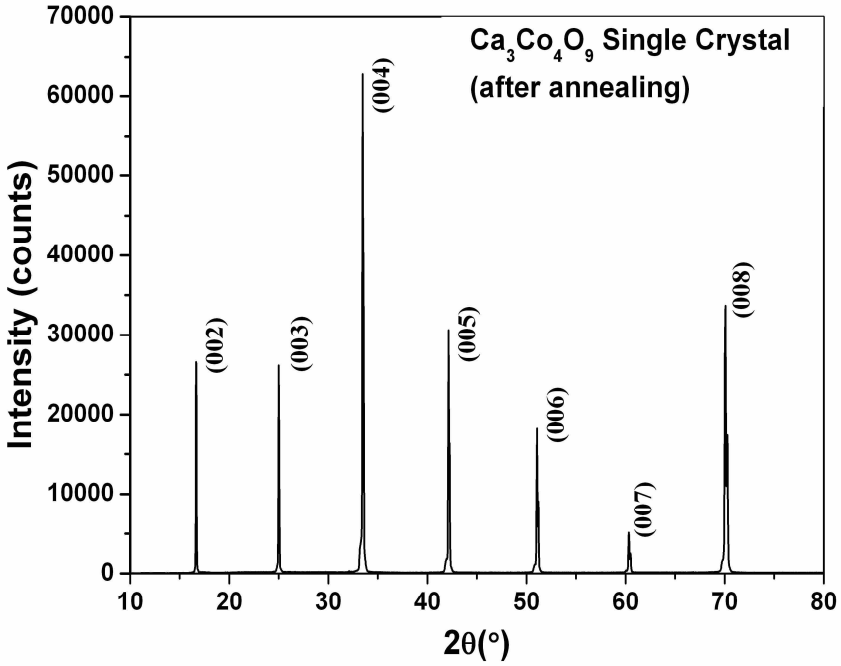

Figure 7.4 The XRD pattern of a $Ca_3Co_4O_9$ single crystal (the thickness ~ 0.1mm) shows the crystalline c-axis perpendicular to the surface (a-b plane) of the crystal.

7.3.2 Thermoelectric Properties

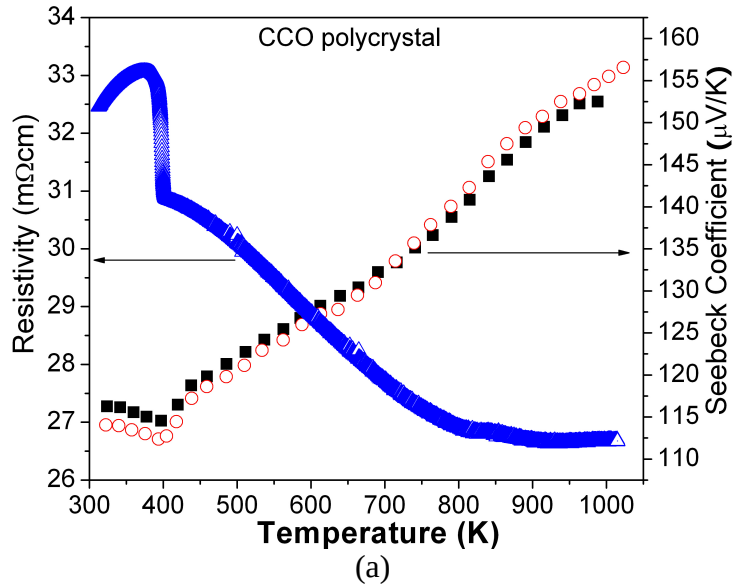

(a)

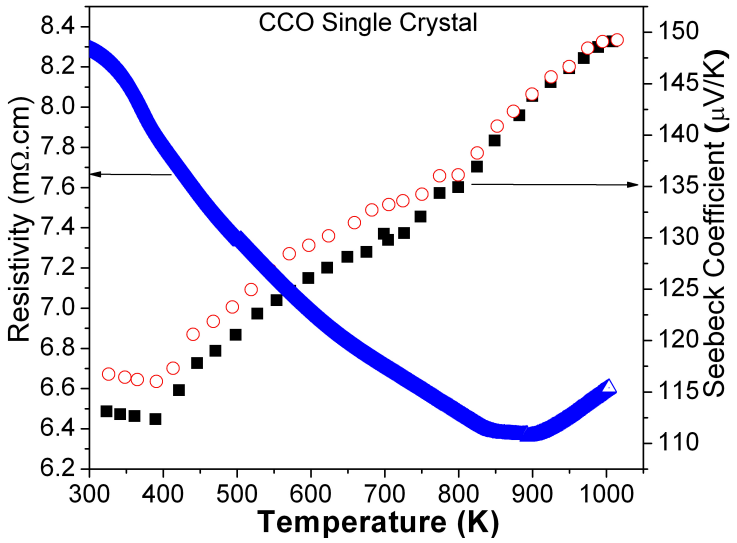

(b)

Figure 7.5 Temperature dependence of thermopower and resistivity of $Ca_3Co_4O_9$ (a) polycrystalline sample, and (b) single crystal (a-b plane) above 300K

Figure 7.5 shows the temperature dependence of thermopower and resistivity of $Ca_3Co_4O_9$ polycrystalline and single crystal (a-b plane) samples. The temperature dependences of both resistivity and thermopower show two transitions above room temperature. One is at 400K, the other one is at around

800K. At 400K, there is a metal-to-semiconductor transition. ρ-T curve shows semiconductor pattern above 400K. Resistivity decreases with increasing temperature. A sharp resistivity drop was observed in CCO polycrystal; while single crystal only showed a slope change. This indicates that this transition has much stronger effect on c-axis electronic transport. The behavior of the temperature dependence of thermopower changed at the same temperature: for both poly-crystal and single crystal samples, the thermopowers have very weak temperature dependence from 130K to 400K, then increase with temperature quickly from 400K up to 1000K.

The increase in S and decrease in ρ with increasing temperature is different from what has been observed in common semiconductors, in which both S and ρ decrease with increasing temperature. It has been suggested that, both electronic correlation and the entropy of electrons localized in degenerated states contribute to the high S of cobaltates.[111] And the transport behavior should be understood within the frame of spin dependent hopping.[112]

What happened at 400K in CCO and lead to such a special transport behavior is still not very clear. Cheng *et al*. observed a distinct endothermic peak by differential scanning calorimetry (DSC) and a sharp peak of thermal expansion coefficient at 396K on heating. They suggested that this is a first-order phase transition.[113]

By carefully measuring the thermopower above 400K, we observed another transition around 800K, and thermopower increased faster above this temperature, which happened at the same temperature as the second transition on

ρ-T curve. When temperature was raised to around 1000K, the slope changed again and become smaller.

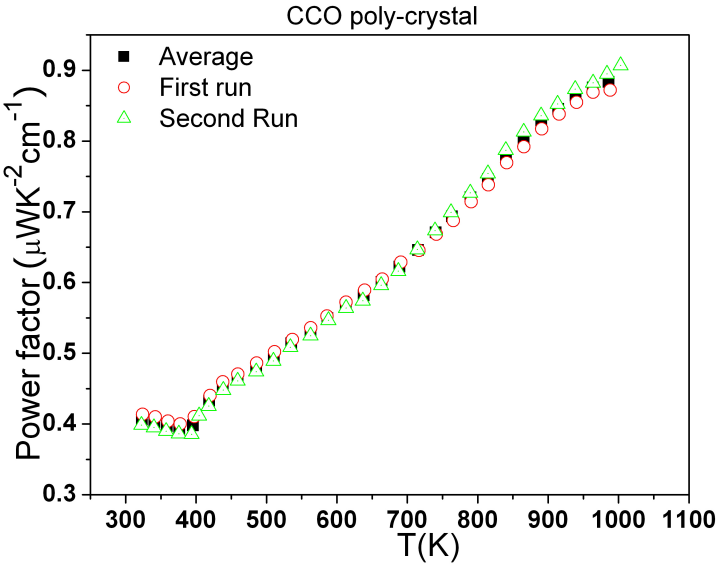

(a)

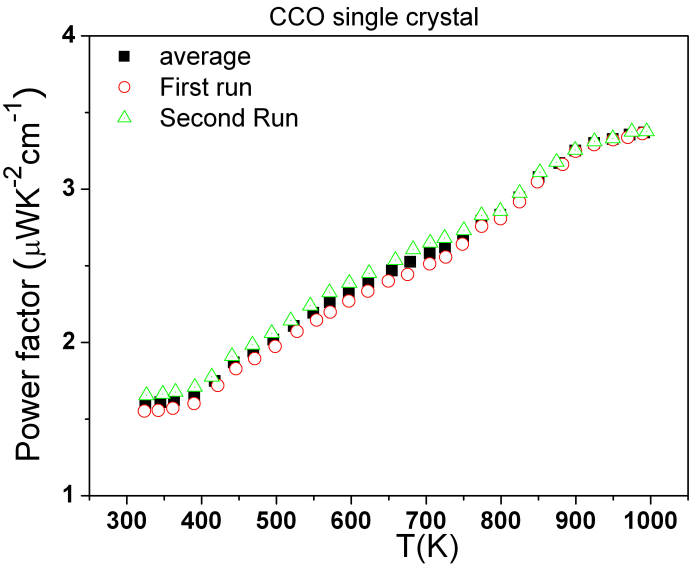

(b)

Figure 7.6 The temperature dependence of power factors for CCO polycrystal (a) and single crystal a-b plane (b).

The increase of thermopower and electric conductivity with rising temperature gave rise to a great enhancement of power factor at higher temperature, especially above 800K, in both CCO polycrystal and single crystal

(as shown in figure 7.6). The power factors are more than doubled from 400K to 1000K. And about half of the increase was achieved from 800K to 1000K. So the high temperature phase is promising for thermoelectric applications.

7.3.3 Structural Transition Identified by i*n-situ* X-ray Powder Diffraction

Our *in-situ* X-ray investigation, as shown in Figure 7.7, confirmed that a structural transition occurrs at 400 K, where a sharp drop of resistivity in polycrystalline samples was observed. The room temperature x-ray diffraction pattern of CCO shows a small peak between 001 and 002 peak, which has also been observed by A.C. Masset *et al*.[103] This peak presumably related to some small structural change of superstructures, which are yet to be clarified. When the sample temperature was increased to 393 K, another peak appeared and the original peak disappeared at 398 K. According to the TEM work, performed by our collaborators at BNL, this peak is associated with a set of extra weak satellite reflections described by the $q_2=2/3a^*_1-1/3c^*_1$ vector. Herve Muguerra *et al.*'s TEM study as a function of temperature on these satellite reflections shows that their intensities rapidly increase around 400K and finally reach a constant maximal value. And they suggest that this intensity variations result from a modification of the structural configuration of the [CoO] layer.[114] Accompanying this structural change, there is change of spin state of Co-ions from low spin configuration to intermediate spin state, that affect the transport properties.[103]

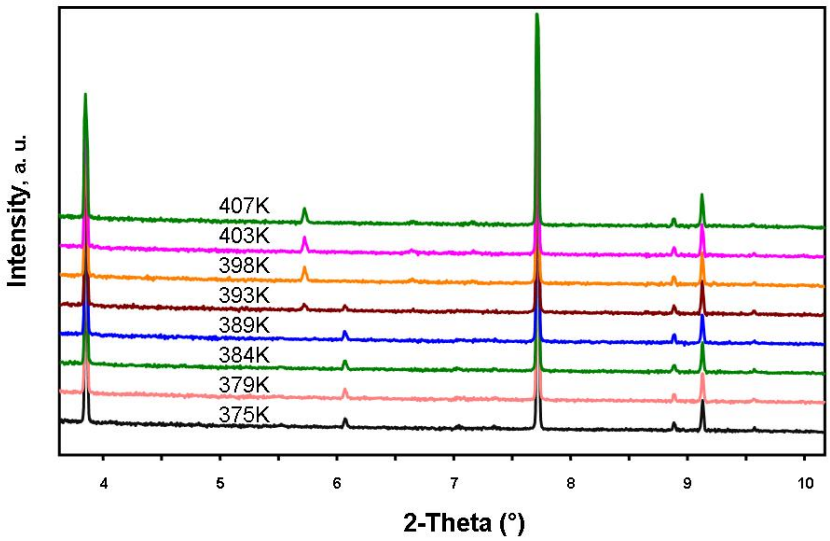

Figure 7.7 The X-ray powder diffraction spectrum of $Ca_3Co_4O_9$ recorded from 375 to 407K

The transition at 800K is also confirmed by our *in-situ* high-T X-ray investigation. Figure 7.8 (a) shows the 004 peak of CCO powder X-ray diffraction pattern at four different temperatures. It is clear that a transition happened between 780 K and 820 K. This transition leads 004 to shift towards the small angle side. By calculating the temperature dependence of lattice parameter along c-axis according to the peak position, which is shown in Figure 7.8 (b), we observed a sharp change around 800K. Lattice parameter along c-axis was expanded from 10.70Å to 10.76Å through this transition.

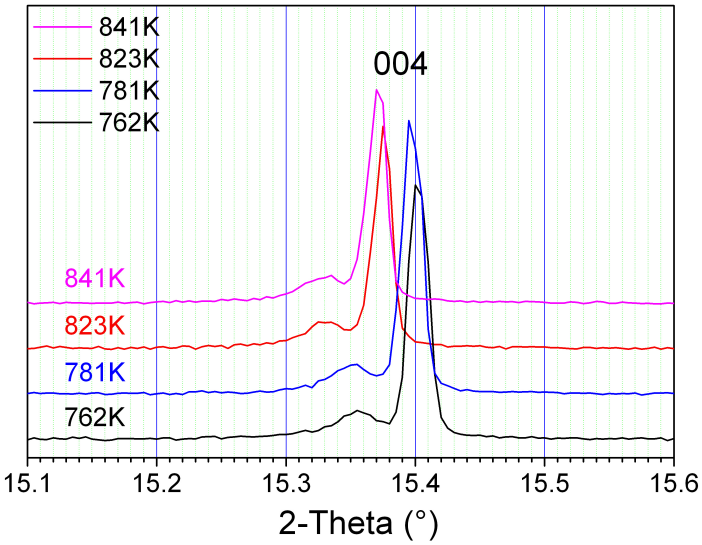

(a)

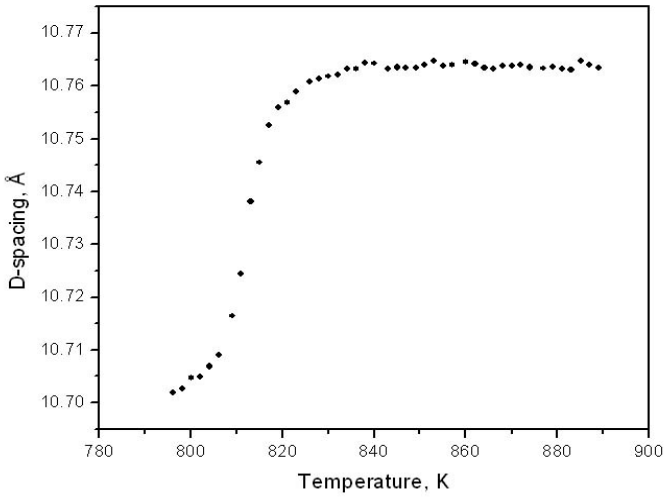

(b)

Figure 7.8 The 004 Peak shifting (a) and d-spacing change (b) of $Ca_3Co_4O_9$ around 800K

7.4 Suggestions for theoretical modeling

We have shown that a coordinated experimental investigation, by *in-situ* high temperature X-ray powder diffraction and thermoelectric properties measurements, identified two structural transitions above room temperature. One is observed at 400K, which changes the transport behavior from metal-like behavior to hopping mechanism and results in the power factors to increase with temperature. The second transition at 800K makes the power factors to increase even faster and reach a plateau above 900K. An important question which arises as a result of our findings is how the electronic structures of this material are modified by these structure changes. To answer this question, extensive theoretical modeling is necessary, and is beyond the scope of present studies. We believe these observations provide strong evidence that a small structural perturbation in complex, electron correlated materials, such as cobaltites, can give rise to a large response in their electronic structure which can lead to a big change in their properties. Furthermore, our observations provide important technical data for the practical application of these materials in thermoelectric modules, where thermal expansion matching is an important issue.

REFERENCES

1. Sales, B.C., D. Mandrus, and R.K. Williams, *Filled skutterudite antimonides: A new class of thermoelectric materials.* Science, 1996. **272**(5266): p. 1325-1328.
2. Sales, B.C., et al., *Filled skutterudite antimonides: Electron crystals and phonon glasses.* Physical Review B, 1997. **56**(23): p. 15081-15089.
3. Jean-Pierre Fleurial, A.B., Thierry Caillat, donald T. Morelli and Gregory P. Meisner, *High figure of merit in Ce-filled skutterudites.* Fifteenth International Conference on Thermoelectrics, 1996: p. 91 - 95
4. Salvador, J.R., et al., *Transport and mechanical properties of Yb-filled skutterudites.* Philosophical Magazine, 2009. **89**(19): p. 1517-1534.
5. Morelli, D.T., et al., *Low-Temperature Transport-Properties of p-type CoSb3.* Physical Review B, 1995. **51**(15): p. 9622-9628.
6. Morelli, D.T. and G.P. Meisner, *Low-Temperature properties of the filled skutterudite CeFe4Sb12.* Journal of Applied Physics, 1995. **77**(8): p. 3777-3781.
7. Nolas, G.S., J.L. Cohn, and G.A. Slack, *Effect of partial void filling on the lattice thermal conductivity of skudderudites.* Physical Review B, 1998. **58**(1): p. 164-170.
8. Nolas, G.S., et al., *High figure of merit in partially filled ytterbium skutterudite materials.* Applied Physics Letters, 2000. **77**(12): p. 1855-1857.
9. Shi, X., et al., *Low thermal conductivity and high thermoelectric figure of merit in n-type BaxYbyCo(4)Sb(12) double-filled skutterudites.* Applied Physics Letters, 2008. **92**: p. 182101.
10. Shi, X., et al., *Thermoelectric Properties of n-Type Multiple-Filled Skutterudites.* Journal of Electronic Materials, 2009. **38**(7): p. 930-933.
11. Tang, X.F., et al., *Synthesis and thermoelectric properties of p-type- and n-type-filled skutterudite RyMxCo4-xSb12(R : Ce,Ba,Y; M : Fe,Ni).* Journal of Applied Physics, 2005. **97**(9): p. 093712
12. Morelli, D.T., et al., *Cerium filling and doping of cobalt triantimonide.* Physical Review B, 1997. **56**(12): p. 7376-7383.
13. Chen, G., *Thermal conductivity and ballistic-phonon transport in the cross-plane direction of superlattices.* Physical Review B, 1998. **57**(23): p. 14958-14973.
14. Venkatasubramanian, R., et al., *Thin-film thermoelectric devices with high room-temperature figures of merit.* Nature, 2001. **413**(6856): p. 597-602.
15. Harman, T.C., et al., *Quantum dot superlattice thermoelectric materials and devices.* Science, 2002. **297**(5590): p. 2229-2232.
16. Poudel, B., et al., *High-thermoelectric performance of nanostructured bismuth antimony telluride bulk alloys.* Science, 2008. **320**(5876): p. 634-638.
17. Li, H., et al., *Preparation and thermoelectric properties of high-performance Sb additional Yb0.2Co4Sb12+y bulk materials with nanostructure.* Applied Physics Letters, 2008. **92**: p. 202114.

18. Li, H., et al., *Rapid preparation method of bulk nanostructured Yb0.3Co4Sb12+y compounds and their improved thermoelectric performance.* Applied Physics Letters, 2008. **93**: p. 252109.
19. Li, H., et al., *Nanostructured bulk YbxCo4Sb12 with high thermoelectric performance prepared by the rapid solidification method.* Journal of Physics D-Applied Physics, 2009. **42**(14).
20. MacDonald, D.K.C., *Thermoelectricity: an introduction to the principles*. 1962, New York . London: John Wiley & Sons, Inc.
21. Yang, J.H. and T. Caillat, *Thermoelectric materials for space and automotive power generation.* Mrs Bulletin, 2006. **31**(3): p. 224-229.
22. Tritt, T.M. and M.A. Subramanian, *Thermoelectric materials, phenomena, and applications: A bird's eye view.* Mrs Bulletin, 2006. **31**(3): p. 188-194.
23. DiSalvo, F.J., *Thermoelectric cooling and power generation.* Science, 1999. **285**(5428): p. 703-706.
24. Sootsman, J.R., D.Y. Chung, and M.G. Kanatzidis, *New and Old Concepts in Thermoelectric Materials.* Angewandte Chemie-International Edition, 2009. **48**(46): p. 8616-8639.
25. Goldsmid, H.J. and R.W. Douglas, *THE USE OF SEMICONDUCTORS IN THERMOELECTRIC REFRIGERATION.* British Journal of Applied Physics, 1954. **5**(NOV): p. 386-390.
26. Rosi, F.D., E.F. Hockings, and N.E. Lindenblad, *SEMICONDUCTING MATERIALS FOR THERMOELECTRIC POWER GENERATION.* Rca Review, 1961. **22**(1): p. 82-121.
27. Rosi, F.D., *THERMOELECTRICITY AND THERMOELECTRIC POWER GENERATION.* Solid-State Electronics, 1968. **11**(9): p. 833-&.
28. Wood, C., *MATERIALS FOR THERMOELECTRIC ENERGY-CONVERSION.* Reports on Progress in Physics, 1988. **51**(4): p. 459-539.
29. Scherrer, H. and S. Scherrer, *THERMOELECTRICS HANDBOOK: MACRO TO NANO* ed. D.M. Rowe. Vol. Chapter 27. 2006, Boca Raton, London, New York: Taylor & Francis Group, LLC.
30. Kutasov, V.A., L.N. Lukyanova, and M.V. Vedernikov, *THERMOELECTRICS HANDBOOK: MACRO TO NANO*, ed. D.M. Rowe. Vol. Chapter 37. 2006, Boca Raton, London, New York: Taylor & Francis Group, LLC.
31. Kuznetsov, V.L., et al., *High performance functionally graded and segmented Bi2Te3-based materials for thermoelectric power generation.* Journal of Materials Science, 2002. **37**(14): p. 2893-2897.
32. Snyder, G.J. and E.S. Toberer, *Complex thermoelectric materials.* Nature Materials, 2008. **7**(2): p. 105-114.
33. Gelbstein, Y., Z. Dashevsky, and M.P. Dariel, *High performance n-type PbTe-based materials for thermoelectric applications.* Physica B-Condensed Matter, 2005. **363**(1-4): p. 196-205.
34. Hsu, K.F., et al., *Cubic AgPbmSbTe2+m: Bulk thermoelectric materials with high figure of merit.* Science, 2004. **303**(5659): p. 818-821.
35. Skrabek, E.A. and D.S. Trimmer, *CRC Handbook of Thermoelectrics*, ed. D.M. Rowe. 1995, Boca Raton: CRC.

36. Yim, W.M. and A. Amith, *BI-SB ALLOYS FOR MAGNETO-THERMOELECTRIC AND THERMOMAGNETIC COOLING.* Solid-State Electronics, 1972. **15**(10): p. 1141-&.
37. Sidorenko, N.A. and L.D. Ivanova, *Bi-Sb solid solutions: Potential materials for high-efficiency thermoelectric cooling to below 180 K.* Inorganic Materials, 2001. **37**(4): p. 331-335.
38. Kittel, C., *Introduction to Solide State Physics*. 7th ed. 1996, New York, Chichester, Brisbane, Toronto, Singapore: John Wiley &Sons, Inc.
39. Mahan, G., B. Sales, and J. Sharp, *Thermoelectric materials: New approaches to an old problem.* Physics Today, 1997. **50**(3): p. 42-47.
40. Mahan, G.D., *FIGURE OF MERIT FOR THERMOELECTRICS.* Journal of Applied Physics, 1989. **65**(4): p. 1578-1583.
41. Goldsmid, H.J., *Electronic Refrigeration*. 1986, London: Pion Limited.
42. Mahan, G.D., *Good thermoelectrics*, in *Solid State Physics, Vol 51*. 1998, Academic Press Inc: San Diego. p. 81-157.
43. Slack, G.A., *New Materials and Performance Limits for Thermoelectric Cooling*, in *CRC Handbook of Thermoelelctrics*, D.M. Rowe, Editor. 1995, CRC Press, Inc. p. 407.
44. Keyes, R.W., *HIGH-TEMPERATURE THERMAL CONDUCTIVITY OF INSULATING CRYSTALS - RELATIONSHIP TO THE MELTING POINT.* Physical Review, 1959. **115**(3): p. 564-567.
45. Neil W. Ashcroft, N.D.M., *Solid State Physics*. 1976: Thomson Learning, Inc.
46. Allen, P.B. and J.L. Feldman, *THERMAL-CONDUCTIVITY OF DISORDERED HARMONIC SOLIDS.* Physical Review B, 1993. **48**(17): p. 12581-12588.
47. Spitzer, D.P., *LATTICE THERMAL CONDUCTIVITY OF SEMICONDUCTORS . A CHEMICAL BOND APPROACH.* Journal of Physics and Chemistry of Solids, 1970. **31**(1): p. 19-&.
48. Cohn, J.L., et al., *Glasslike heat conduction in high-mobility crystalline semiconductors.* Physical Review Letters, 1999. **82**(4): p. 779-782.
49. Sharp, J.W., S.J. Poon, and H.J. Goldsmid, *Boundary scattering and the thermoelectric figure of merit.* Physica Status Solidi a-Applied Research, 2001. **187**(2): p. 507-516.
50. Dresselhaus, M.S., et al., *New directions for low-dimensional thermoelectric materials.* Advanced Materials, 2007. **19**(8): p. 1043-1053.
51. Xie, W.J., et al., *Unique nanostructures and enhanced thermoelectric performance of melt-spun BiSbTe alloys.* Applied Physics Letters, 2009. **94**(10).
52. Cao, Y.Q., et al., *Syntheses and thermoelectric properties of Bi2Te3/Sb2Te3 bulk nanocomposites with laminated nanostructure.* Applied Physics Letters, 2008. **92**(14).
53. Bhattacharya, S., et al., *Grain structure effects on the lattice thermal conductivity of Ti-based half-Heusler alloys.* Applied Physics Letters, 2002. **81**(1): p. 43-45.

54. Jeitschko, W. and D. Braun, *LAFE4P12 WITH FILLED COAS3-TYPE STRUCTURE AND ISOTYPIC LANTHANOID-TRANSITION METAL POLYPHOSPHIDES.* Acta Crystallographica Section B-Structural Science, 1977. **33**(NOV): p. 3401-3406.
55. Braun, D.J. and W. Jeitschko, *PREPARATION AND STRUCTURAL INVESTIGATIONS OF ANTI-MONIDES WITH THE LAFE4P12 STRUCTURE.* Journal of the Less-Common Metals, 1980. **72**(1): p. 147-156.
56. Braun, D.J. and W. Jeitschko, *TERNARY ARSENIDES WITH LAFE4P12-TYPE STRUCTURE.* Journal of Solid State Chemistry, 1980. **32**(3): p. 357-363.
57. Braun, D.J. and W. Jeitschko, *THORIUM-CONTAINING PNICTIDES WITH THE LAFE4P12 STRUCTURE.* Journal of the Less-Common Metals, 1980. **76**(1-2): p. 33-40.
58. Singh, D.J. and W.E. Pickett, *SKUTTERUDITE ANTIMONIDES - QUASI-LINEAR BANDS AND UNUSUAL TRANSPORT.* Physical Review B, 1994. **50**(15): p. 11235-11238.
59. Mandrus, D., et al., *ELECTRONIC TRANSPORT IN LIGHTLY DOPED COSB3.* Physical Review B, 1995. **52**(7): p. 4926-4931.
60. Anno, H., et al., *Structural and electronic transport properties of polycrystalline p-type CoSb3.* Journal of Applied Physics, 1998. **83**(10): p. 5270-5276.
61. Li, Q., Z.W. Lin, and J. Zhou, *Thermoelectric Materials with Potential High Power Factors for Electricity Generation.* Journal of Electronic Materials, 2009. **38**(7): p. 1268-1272.
62. Tritt, T.M., et al., *Low-temperature transport properties of the filled and unfilled IrSb3 skutterudite system.* Journal of Applied Physics, 1996. **79**(11): p. 8412-8418.
63. Nolas, G.S., et al., *The effect of rare-earth filling on the lattice thermal conductivity of skutterudites.* Journal of Applied Physics, 1996. **79**(8): p. 4002-4008.
64. Cahn, R.W., *Physical Metallurgy*. Third ed. 1983: Elsevier Science Publishers B.V. .
65. Liebermann, H.H. and C.D. Graham, *PRODUCTION OF AMORPHOUS ALLOY RIBBONS AND EFFECTS OF APPARATUS PARAMETERS ON RIBBON DIMENSIONS.* Ieee Transactions on Magnetics, 1976. **12**(6): p. 921-923.
66. *http://www.scm-sps.com/*.
67. *http://anter.com/TN68.htm*.
68. *http://anter.com*.
69. Chen, B.X., et al., *Low-temperature transport properties of the filled skutterudites CeFe4-xCoxSb12.* Physical Review B, 1997. **55**(3): p. 1476-1480.
70. Seto, J.Y.W., *ELECTRICAL PROPERTIES OF POLYCRYSTALLINE SILICON FILMS.* Journal of Applied Physics, 1975. **46**(12): p. 5247-5254.

71. Tang, X.F., et al., *Synthesis and thermoelectric properties of double-atom-filled skutterudite compounds CamCenFexCo4-xSb12.* Journal of Applied Physics, 2006. **100**(12).
72. Jeischko, W., Metall. Trans. A, 1970. **1**: p. 3159.
73. Poon, S.J., *Electronic and thermoelectric properties of half-Heusler alloys*, in *Recent Trends in Thermoelectric Materials Research Ii*. 2001, Academic Press Inc: San Diego. p. 37-75.
74. Culp, S.R., et al., *Effect of substitutions on the thermoelectric figure of merit of half-Heusler phases at 800 degrees C.* Applied Physics Letters, 2006. **88**(4).
75. Culp, S.R., et al., *(Zr,Hf)Co(Sb,Sn) half-Heusler phases as high-temperature (> 700 degrees C) p-type thermoelectric materials.* Applied Physics Letters, 2008. **93**(2).
76. Qiu, P.F., et al., *Enhanced thermoelectric performance by the combination of alloying and doping in TiCoSb-based half-Heusler compounds.* Journal of Applied Physics, 2009. **106**(10).
77. Shen, Q., et al., *Effects of partial substitution of Ni by Pd on the thermoelectric properties of ZrNiSn-based half-Heusler compounds.* Applied Physics Letters, 2001. **79**(25): p. 4165-4167.
78. Larson, P., et al., *Electronic structure of rare-earth nickel pnictides: Narrow-gap thermoelectric materials.* Physical Review B, 1999. **59**(24): p. 15660-15668.
79. Bhattacharya, S., et al., *Effect of Sb doping on the thermoelectric properties of Ti-based half-Heusler compounds, TiNiSn1-xSbx.* Applied Physics Letters, 2000. **77**(16): p. 2476-2478.
80. Ioffe, A.F., *Physics of Semiconductors* 1960, New York: Academic. 282.
81. Nolas, G.S., et al., *Semiconducting Ge clathrates: Promising candidates for thermoelectric applications.* Applied Physics Letters, 1998. **73**(2): p. 178-180.
82. Kim, W., et al., *Thermal conductivity reduction and thermoelectric figure of merit increase by embedding nanoparticles in crystalline semiconductors.* Physical Review Letters, 2006. **96**(4).
83. Cahill, D.G., S.K. Watson, and R.O. Pohl, *LOWER LIMIT TO THE THERMAL-CONDUCTIVITY OF DISORDERED CRYSTALS.* Physical Review B, 1992. **46**(10): p. 6131-6140.
84. Mahan, G.D. and J.O. Sofo, *The best thermoelectric.* Proceedings of the National Academy of Sciences of the United States of America, 1996. **93**(15): p. 7436-7439.
85. Sales, B.C., et al., *MAGNETIC, TRANSPORT, AND STRUCTURAL-PROPERTIES OF FE1-XIRXSI.* Physical Review B, 1994. **50**(12): p. 8207-8213.
86. Jones, C.D.W., K.A. Regan, and F.J. DiSalvo, *Thermoelectric properties of the doped Kondo insulator: NdxCe3-xPt3Sb4.* Physical Review B, 1998. **58**(24): p. 16057-16063.

87. Jones, C.D.W., K.A. Regan, and F.J. DiSalvo, *Ce3CuxPt3-xSb4: Modifying the properties of a Kondo insulator by substitutional doping.* Physical Review B, 1999. **60**(8): p. 5282-5286.
88. Sato, H., et al., *Anomalous transport properties of RFe4P12 (R = La, Ce, Pr, and Nd).* Physical Review B, 2000. **62**(22): p. 15125-15130.
89. Abe, K., et al., *Transport properties in the filled-skutterudite compounds RERu4Sb12 (RE-La, Ce, Pr and Nd); an exotic heavy fermion semimetal CeRu4Sb12.* Journal of Physics-Condensed Matter, 2002. **14**(45): p. 11757-11768.
90. Harutyunyan, S.R., et al., *Thermoelectric cooling at cryogenic temperatures.* Applied Physics Letters, 2003. **83**(11): p. 2142-2144.
91. Hulliger, F., *MARCASITE-TYPE SEMICONDUCTORS.* Nature, 1963. **198**(488): p. 1081-&.
92. Petrovic, C., et al., *Anisotropy and large magnetoresistance in the narrow-gap semiconductor FeSb2.* Physical Review B, 2003. **67**(15).
93. Petrovic, C., et al., *Kondo insulator description of spin state transition in FeSb2.* Physical Review B, 2005. **72**(4).
94. Perucchi, A., et al., *Optical investigation of the metal-insulator transition in FeSb2.* European Physical Journal B, 2006. **54**(2): p. 175-183.
95. Bentien, A., et al., *Colossal Seebeck coefficient in strongly correlated semiconductor FeSb2 (vol 80 pg 17008, 2007).* Epl, 2007. **80**(3).
96. Nath, R., et al., *Single-crystal P-31 NMR studies of the frustrated square-lattice compound Pb-2(VO)(PO4)(2).* Physical Review B, 2009. **80**(21).
97. Kitagawa, K., et al., *Antiferromagnetism of SrFe2As2 Studied by Single-Crystal As-75-NMR.* Journal of the Physical Society of Japan, 2009. **78**(6).
98. Chapman, K.W., et al., *Optimizing high-pressure pair distribution function measurements in diamond anvil cells.* Journal of Applied Crystallography, 2010. **43**: p. 297-307.
99. White, C.E., et al., *Combining density functional theory (DFT) and pair distribution function (PDF) analysis to solve the structure of metastable materials: the case of metakaolin.* Physical Chemistry Chemical Physics, 2010. **12**(13): p. 3239-3245.
100. Bin Im, W., et al., *Probing local structure in the yellow phosphor LaSr2AlO5 : Ce3+, by the maximum entropy method and pair distribution function analysis.* Journal of Materials Chemistry, 2009. **19**(46): p. 8761-8766.
101. Lukoyanov, A.V., et al., *The semiconductor-to-ferromagnetic-metal transition in FeSb2.* European Physical Journal B, 2006. **53**(2): p. 205-207.
102. Terasaki, I., Y. Sasago, and K. Uchinokura, *Large thermoelectric power in NaCo2O4 single crystals.* Physical Review B, 1997. **56**(20): p. 12685-12687.
103. Masset, A.C., et al., *Misfit-layered cobaltite with an anisotropic giant magnetoresistance: Ca3Co4O9.* Physical Review B, 2000. **62**(1): p. 166-175.

104. Lambert, S., H. Leligny, and D. Grebille, *Three forms of the misfit layered cobaltite Ca2CoO3 CoO2 (1.62) - A 4D structural investigation.* Journal of Solid State Chemistry, 2001. **160**(2): p. 322-331.
105. Funahashi, R. and S. Urata, *Fabrication and application of an oxide thermoelectric system.* International Journal of Applied Ceramic Technology, 2007. **4**(4): p. 297-307.
106. Urata, S., et al., *Power generation of a p-type Ca3Co4O9/n-type CaMnO3 module.* International Journal of Applied Ceramic Technology, 2007. **4**(6): p. 535-540.
107. Noudem, J.G., et al., *Thermoelectric ceramics for generators.* Journal of the European Ceramic Society, 2008. **28**(1): p. 41-48.
108. Sugiyama, J., C.T. Xia, and T. Tani, *Anisotropic magnetic properties of Ca3Co4O9: Evidence for a spin-density-wave transition at 27 K.* Physical Review B, 2003. **67**: p. 104410.
109. Singh, A.K. and G. Ramani, *MEASUREMENT OF THERMOELECTRIC-POWER OF SOLIDS UP TO 10 GPA.* Review of Scientific Instruments, 1978. **49**(9): p. 1324-1326.
110. Littleton, R.T., et al., *High-Temperature Transport Probe for Thermopower and Resistivity Measurements* Mat. Res. Soc. Symp. Proc., 1998. **545**: p. 137.
111. Limelette, P., et al., *Scaling behavior in thermoelectric misfit cobalt oxides.* Physical Review Letters, 2006. **97**: p. 046601.
112. Limelette, P., et al., *Magnetoresistance scaling in the layered cobaltate Ca3Co4O9.* Physical Review B, 2008. **77**: p. 245123.
113. Cheng, J.G., et al., *First-order phase transition characteristic of the high temperature metal-semiconductor transition in Ca2CoO3 (0.62) CoO2.* Applied Physics a-Materials Science & Processing, 2009. **94**(4): p. 911-916.
114. Muguerra, H. and D. Grebille, *Original disorder-order transition related to electronic and magnetic properties in the thermoelectric misfit phase Ca2CoO3 CoO2 (1.62).* Acta Crystallographica Section B-Structural Science, 2008. **64**: p. 676-683.